

Navigating Text-To-Image Customization: From LyCORIS Fine-Tuning to Model Evaluation

Shin-Ying Yeh^{1*} Yu-Guan Hsieh^{2†} Zhidong Gao^{3*}
Bernard B W Yang⁴ Giyeong Oh⁵ Yanmin Gong³

¹National Tsing Hua University, Taiwan

²Université Grenoble Alpes, France

³University of Texas at San Antonio, USA

⁴University of Toronto, Canada

⁵Yonsei University, South Korea

<https://github.com/KohakuBlueleaf/LyCORIS>

Abstract

Text-to-image generative models have garnered immense attention for their ability to produce high-fidelity images from text prompts. Among these, Stable Diffusion distinguishes itself as a leading open-source model in this fast-growing field. However, the intricacies of fine-tuning these models pose multiple challenges from new methodology integration to systematic evaluation. Addressing these issues, this paper introduces LyCORIS (Lora by Yond Conventional methods, Other Rank adaptation Implementations for Stable diffusion), an open-source library that offers a wide selection of fine-tuning methodologies for Stable Diffusion. Furthermore, we present a thorough framework for the systematic assessment of varied fine-tuning techniques. This framework employs a diverse suite of metrics and delves into multiple facets of fine-tuning, including hyperparameter adjustments and the evaluation with different prompt types across various concept categories. Through this comprehensive approach, our work provides essential insights into the nuanced effects of fine-tuning parameters, bridging the gap between state-of-the-art research and practical application.

1 Introduction

The recent advancements in deep generative models along with the availability of vast data on the internet have ushered in a new era of text-to-image synthesis (Balaji et al., 2022; Ramesh et al., 2022; Saharia et al., 2022). These models allow users to transform text prompts into high-quality, visually appealing images, revolutionizing the way we conceive of and interact with digital media (Ko et al., 2023; Zhang et al., 2023). Moreover, the models' wide accessibility and user-friendly interfaces extend their influence beyond the research community to laypeople who aspire to create their own artworks. Among these, Stable Diffusion (Rombach et al., 2022) emerges as one of the pioneering open-source models offering such capabilities. Its open-source nature has served as a catalyst for a multitude of advances, attracting both researchers and casual users alike. Extensions such as cross-attention control (Liu et al., 2022) and ControlNet (Zhang et al., 2023) have further enriched the landscape, broadening the model's appeal and utility.

*Equal contribution.

†Corresponding author: <cyberhsieh212@gmail.com>

While these models offer an extensive repertoire of image generation, they often fall short in capturing highly personalized or novel concepts, leading to a burgeoning interest in model customization techniques. Initiatives like DreamBooth (Ruiz et al., 2023) and Textual Inversion (Gal et al., 2023) have spearheaded efforts in this domain, allowing users to imbue pretrained models like Stable Diffusion with new concepts through a small set of representative images (see Appendix A for detailed related work). Coupled with user-friendly trainers designed to customize Stable Diffusion, the ecosystem now boasts a plethora of specialized models and dedicated platforms that host them—often witnessing the upload of thousands of new models to a single website in just one week.

In spite of this burgeoning landscape, our understanding of the intricacies involved in fine-tuning these models remains limited. The complexity of the task—from variations in datasets, image types, and captioning strategies, to the abundance of available methods each with their own sets of hyperparameters—renders it a challenging terrain to navigate. While new methods proposed by researchers offer much potential, they are not always seamlessly integrated into the existing ecosystem, which can hinder comprehensive testing and wider adoption. Moreover, current evaluation paradigms lack a systematic approach that covers the full depth and breadth of what fine-tuning entails. To address these gaps and bridge the divide between research innovations and casual usage, we present our contributions as follows.

1. We develop LyCORIS, an open source library dedicated to fine-tuning of Stable Diffusion. This library encapsulates a spectrum of methodologies ranging from matrix factorization techniques like LoRA, LoHa, and LoKr, to emerging strategies such as DyLoRA, GLoRA, GLoKr, and (IA)³ that are newer and lesser-explored in the context of text-to-image models.
2. To enable rigorous comparisons between methods, we propose a comprehensive evaluation framework that incorporates a wide range of metrics, capturing key aspects such as concept fidelity, text-image alignment, image diversity, and preservation of the base model’s style.
3. Through extensive experiments, we compare the performances of different fine-tuning algorithms implemented in LyCORIS and assess the impacts of various hyperparameters, offering insights into how these factors influence the results. Concurrently, we underscore the complexities inherent in model evaluation, advocating for the development and adoption of more comprehensive and systematic evaluation processes.

2 Preliminary

In this section, we briefly review the two core components of our study: Stable Diffusion and LoRA for model customization.

2.1 Stable Diffusion

Diffusion models (Ho et al., 2020; Sohl-Dickstein et al., 2015) are a family of probabilistic generative models that are trained to capture a data distribution through a sequence of denoising operations. Given an initial noise map $\mathbf{x}_T \sim \mathcal{N}(0, \mathbf{I})$, the models iteratively refine it by reversing the diffusion process until it is synthesized into a desired image \mathbf{x}_0 . These models can be conditioned on elements such as text prompts, class labels, or low-resolution images, allowing conditioned generation.

Specifically, our work is based on Stable Diffusion, a text-to-image latent diffusion model (Rombach et al., 2022) pretrained on the LAION 5-billion image dataset (Schuhmann et al., 2022). Latent diffusion models reduce the cost of diffusion models by shifting the denoising operation into the latent space of a pre-trained variational autoencoder, composed of an encoder \mathcal{E} and a decoder \mathcal{D} . During training, the noise is added to the encoder’s latent output $\mathbf{z} = \mathcal{E}(\mathbf{x}_0)$ for each time step $t \in \{0, \dots, T\}$, resulting in a noisy latent \mathbf{z}_t . Then, the model is trained to predict the noise applied to \mathbf{z}_t , given text conditioning $\mathbf{c} = \mathcal{T}(l)$ obtained from an image description l (also known as the image’s caption) using a text encoder \mathcal{T} . Formally, with θ denoting the parameter of the denoising U-Net and $\epsilon_\theta(\cdot)$ representing the predicted noise from this model, we aim to minimize

$$\mathcal{L}(\theta) = \mathbb{E}_{\mathbf{x}_0, \mathbf{c}, \epsilon, t} [\|\epsilon - \epsilon_\theta(\mathbf{z}_t, t, \mathbf{c})\|_2^2], \quad (1)$$

where \mathbf{x}_0, \mathbf{c} are drawn from the dataset, $\epsilon \sim \mathcal{N}(0, \mathbf{I})$, and t is uniformly drawn from $\{1, \dots, T\}$.

2.2 Model Customization With LoRA

To enable more personalized experiences, model customization has been proposed as a means to adapt foundational models to specific domains or concepts. In the case of Stable Diffusion, this frequently involves fine-tuning a pretrained model by minimizing the original loss function (1) on a new dataset, containing as few as a single image for each target concept. In this process, we introduce a *concept descriptor* $[V]$ for each target concept, comprising a neutral *trigger word* $[V_{\text{trigger}}]$ and an optional *class word* $[V_{\text{class}}]$ to denote the category to which the concept belongs. This concept descriptor is intended for use in both the image captions and text prompts. While it is possible to include a prior-preservation loss by utilizing a set of regularization images (Kumari et al., 2023; Ruiz et al., 2023), we have chosen not to employ this strategy in the current study (see Appendix D.1 for a detailed discussion).

Low-Rank Adaptation (LoRA). When integrated into the model customization process, Low-Rank Adaptation (LoRA) could substantially reduce the number of parameters that need to be updated. It was originally developed for large language models (Hu et al., 2021), and later adapted for Stable Diffusion by Simo Ryu (2022). LoRA operates by constraining fine-tuning to a low-rank subspace of the original parameter space. More specifically, the *weight update* $\Delta W \in \mathbb{R}^{p \times q}$ is pre-factorized into two low-rank matrixes $B \in \mathbb{R}^{p \times r}$, $A \in \mathbb{R}^{r \times q}$, where p, q are the dimensions of the original model parameter, r is the dimension of the low-rank matrix, and $r \ll \min(p, q)$. During fine-tuning, the foundational model parameter W_0 remains frozen, and only the low-rank matrices are updated. Formally, the forward pass of $\mathbf{h}' = W_0 \mathbf{h} + \mathbf{b}$ is modified to:

$$\mathbf{h}' = W_0 \mathbf{h} + \mathbf{b} + \gamma \Delta W \mathbf{h} = W_0 \mathbf{h} + \mathbf{b} + \gamma B A \mathbf{h}, \quad (2)$$

where γ is a *merge ratio* that balances the retention of pretrained model information and its adaptation to the target concepts.¹ Following Hu et al. (2021), we further define $\alpha = \gamma r$ so that $\gamma = \alpha/r$.

3 The LyCORIS Library

Building upon the initiative of LoRA, this section introduces LyCORIS, our open-source library that provides an array of different methods for fine-tuning Stable Diffusion.

3.1 Design and Objectives

LyCORIS stands for *Lora beyond Conventional methods, Other Rank adaptation Implementations for Stable diffusion*. Broadly speaking, the library’s main objective is to serve as a test bed for users to experiment with a variety of fine-tuning strategies for Stable Diffusion models. Seamlessly integrating into the existing ecosystem, LyCORIS is compatible with easy-to-use command-line tools and graphic interfaces, allowing users to leverage the algorithms implemented in the library effortlessly. Additionally, native support exists in popular user interfaces designed for image generation, facilitating the use of models fine-tuned through LyCORIS methods. For most of the algorithms implemented in LyCORIS, stored parameters naturally allow for the reconstruction of the weight update ΔW . This design brings inherent flexibility: it enables the weight updates to be scaled and applied to a base model W'_0 different from those originally used for training, expressed as $W' = W'_0 + \lambda \Delta W$. Furthermore, a weight update can be combined with those from other fine-tuned models, further compressed, or integrated with advanced tools like ControlNet. This opens up a diverse range of possibilities for the application of these fine-tuned models.

3.2 Implemented Algorithms

We now discuss the core of the library—the algorithms implemented in LyCORIS. For conciseness, we will primarily focus on three main algorithms: LoRA (LoCon), LoHa, and LoKr. The merge ratio $\gamma = \alpha/r$ introduced in (2) is implemented for all these methods.

¹Setting γ is mathematically equivalent to scaling the initialization of B and A by $\sqrt{\gamma}$ and scaling the learning rate by $\sqrt{\gamma}$ or γ , depending on the used optimizer. See Appendix B.1 for a generalization of this result.

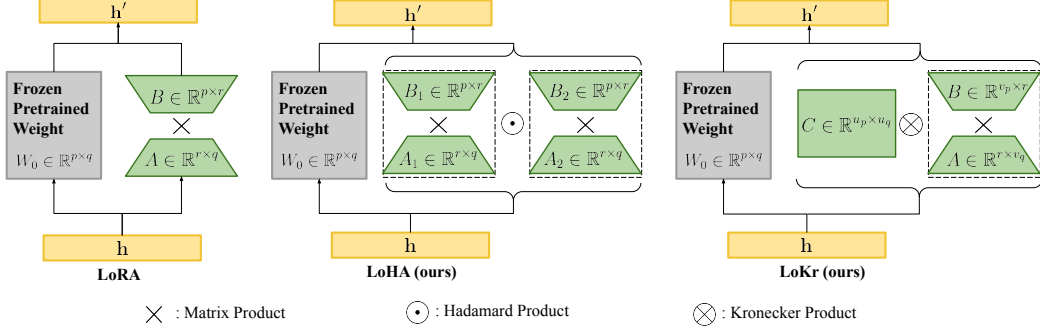


Figure 1: This figure shows the structure of the proposed Loha and Lokr modules implemented in LyCORIS.

LoRA (LoCon). In the work of [Hu et al. \(2021\)](#), the focus was primarily centered on applying the low-rank adapter to the attention layer within the large language model. In contrast, the convolutional layers play a key role in diffusion models. Therefore, we extend the method to the convolutional layers of diffusion models. The intuition behind this is with more layers getting involved during fine-tuning, the performance (generated image quality and fidelity) should be better.

In particular, consider a convolutional layer with a weight update denoted as $\Delta W \in \mathbb{R}^{c_{\text{out}} \times c_{\text{in}} \times k \times k}$, where k represents kernel size, c_{in} and c_{out} indicate the number of input channels and output channels. To facilitate the application of our method, this weight update can be unrolled into a 2-D matrix represented as $\Delta W \in \mathbb{R}^{c_{\text{out}} \times c_{\text{in}} k^2}$. Factorizing this 2-D matrix gives us two matrices of reduced rank: $B \in \mathbb{R}^{c_{\text{out}} \times r}$, $A \in \mathbb{R}^{r \times c_{\text{in}} k^2}$. The matrix A can be reshaped back to a 4-D tensor: $A \in \mathbb{R}^{r \times c_{\text{in}} \times k \times k}$. Such a transformation implies that the given convolutional layer can be effectively approximated by two consecutive convolutional layers with kernel sizes k and 1. Notably, the low-rank dimension r is the number of output and input channels of the first and second layers. This decomposition method is well-established and has been extensively adopted in previous research (see e.g., [Wang et al., 2021](#)). Beyond this basic approach, we also implement the Tucker decomposition ([Tucker, 1966](#)) for the convolutional layers, as explained in [Appendix B.2](#).

LoHa. Inspired by the basic idea underlying LoRA, we explore the potential enhancements in fine-tuning methods. In particular, it is well recognized that methods based on matrix factorization suffer from the *low-rank constraint*. Within the LoRA framework, weight updates are confined within the low-rank space, inevitably impacting the performance of the fine-tuned model. To achieve better fine-tuning performance, we conjecture that a relatively large rank might be necessary, particularly when working with larger fine-tuning datasets or when the data distribution of downstream tasks greatly deviates from the pretraining data. However, this cloud leads to increased memory usage and more storage demands.

FedPara ([Hyeon-Woo et al., 2022](#)) is a technique originally developed for federated learning that aims to mitigate the low-rank constraint when applying low-rank decomposition methods to federated learning. One of the advantages of FedPara is that the maximum rank of the resulting matrix is larger than those derived from conventional low-rank decomposition (such as LoRA). More precisely, for $\Delta W = (B_1 A_1) \odot (B_2 A_2)$, where \odot denotes the Hadamard product (element-wise product), $B_1, B_2 \in \mathbb{R}^{p \times r}$, $A_1, A_2 \in \mathbb{R}^{r \times q}$, and $r \leq \min(p, q)$, the rank of ΔW can be as large as r^2 . To make a fair comparison, we assume the low-rank dimension in equation (2) is $2r$, such that they have the same number of trainable parameters. Then, the reconstructed matrix $\Delta W = BA$ has a maximum rank of $2r$. Clearly, $2r < r^2$, if $r > 2$. This implies decomposing the weight update with the Hadamard product could improve the fine-tuning capability given the same number of trainable parameters. We term this method as LoHa (**L**ow-rank adaptation with **H**adamard product). The forward pass of $\mathbf{h}' = W_0 \mathbf{h} + \mathbf{b}$ is then modified to:

$$\mathbf{h}' = W_0 \mathbf{h} + \mathbf{b} + \gamma \Delta W \mathbf{h} = W_0 \mathbf{h} + \mathbf{b} + \gamma [(B_1 A_1) \odot (B_2 A_2)] \mathbf{h}. \quad (3)$$

LoKr. In the same spirit of maximizing matrix rank while minimizing parameter count, our library offers LoKr (**L**ow-rank adaptation with **K**ronecker product) as another viable option. This method is an extension of the KronA technique, initially proposed by [Edalati et al. \(2022\)](#) for fine-tuning of language models, and employs Kronecker products for matrix decomposition. Importantly, we have adapted this technique to work with convolutional layers, similar to what we achieved with LoCon. A unique advantage of using Kronecker products lies in the multiplicative nature of their ranks, allowing us to move beyond the limitations of low-rank assumptions.

Going further, to provide finer granularity for model fine-tuning, we additionally incorporate an optional low-rank decomposition (which users can choose to apply or not) that focuses exclusively on the right block resulting from the Kronecker decomposition.² In summary, writing \otimes for the Kronecker product, the forward pass $\mathbf{h}' = W_0 \mathbf{h} + \mathbf{b}$ is modified to:

$$\mathbf{h}' = W_0 \mathbf{h} + \mathbf{b} + \gamma \Delta W \mathbf{h} = W_0 \mathbf{h} + \mathbf{b} + \gamma [C \otimes (BA)] \mathbf{h}, \quad (4)$$

The size of these matrices are determined by two user-specified hyperparameters: the factor f and the dimension r . With these, we have $C \in \mathbb{R}^{u_p \times u_q}$, $B \in \mathbb{R}^{v_p \times r}$, and $A \in \mathbb{R}^{r \times v_q}$, where

$$u_p = \max(u \leq \min(f, \sqrt{p}) \mid p \bmod u = 0), \quad v_p = \frac{p}{u_p}. \quad (5)$$

The two scalars u_q and v_q are defined in the same way. Interestingly, LoKr has the widest range of potential parameter counts among the three methods and can yield the smallest file sizes when appropriately configured. Additionally, it can be interpreted an adapter that is composed of a number of linear layers, as detailed in [Appendix B.3](#).

Others. In addition to LoRA, LoHa, and LoKr described earlier, our library features other algorithms like DyLoRA ([Valipour et al., 2022](#)), GLoRA ([Chavan et al., 2023](#)), and (IA)³ ([Liu et al., 2022](#)). Moreover, following the basic idea of GLoRA, we have created GLoKr, a fusion of GLoRA concepts with linear layer adaptations of LoKr. However, discussing these supplementary algorithms in detail is beyond the scope of this paper.

4 Evaluating Fine-Tuned Text-To-Image Models

With the wide range of algorithmic choices and hyperparameter settings made possible by LyCORIS, one naturally wonders: Is there an optimal algorithm or set of hyperparameters for fine-tuning Stable Diffusion? To tackle this question in a comprehensive manner, it is essential to first establish a clear framework for model evaluation.

With this in mind, in this section, we turn our focus to two independent but intertwined components that are crucial for a systematic evaluation of fine-tuned text-to-image models: *i*) the types of prompts used for image generation and *ii*) the evaluation of the generated images. While these two components are commonly considered as a single entity in existing literature, explicitly distinguishing between them allows for a more nuanced evaluation of model performance (see [Appendix A](#) for a comprehensive overview of related works on text-to-image model evaluation). Below, we explore each of these components in detail.

4.1 Classification of Prompts for Image Generation

To fully understand the model’s behavior, it is important to distinguish between different types of prompts that guide image generation. We categorize these into three main types as follows:

- **Training Prompts:** These are the prompts originally used for training the model. The images generated from these prompts are expected to closely align with the training dataset, providing insight into how well the model has captured the target concepts.

²As shown in [Eq. \(5\)](#), in our implementation, the right block is always the larger of the two.

- **Generalization Prompts:** These prompts seek to generate images that generalize learned concepts to broader contexts, going beyond the specific types of images encountered in the training set. This includes, for example, combining the innate knowledge of the base model with the learned concepts, combining concepts trained within the same model, and combining concepts trained across different models which are later merged together. Such prompts are particularly useful to evaluate the disentanglement of the learned representations.
- **Concept-Agnostic Prompts:** These are prompts that deliberately avoid using trigger words from the training set and are often employed to assess concept leak, see e.g., Kumari et al. (2023). When training also involves class words, this category can be further refined to distinguish between prompts that do and do not use these class words.

4.2 Evaluation Criteria

After detailing the different types of prompts that guide the image generation process, the next important step is to identify the aspects that we would like to look at when evaluating the generated images, as we outline below.

- **Fidelity** measures the extent to which generated images adhere to the target concept.
- **Controllability** evaluates the model’s ability to generate images that align well with text prompts.
- **Diversity** assesses the variety of images that are produced from a single or a set of prompts.
- **Base Model Preservation** measures how much fine-tuning affects the base model’s inherent capabilities, particularly in ways that may be undesirable. For example, if the target concept is an object, retaining the background and style as generated by the base model might be desired.
- **Image Quality** concerns the visual appeal of the generated images, focusing primarily on aspects like naturalness, absence of artifacts, and lack of weird deformations. Aesthetics, though related, are considered to be more dependent on the dataset than on the training method, and are therefore not relevant for our purpose.

Taken together, the prompt classification of Section 4.1 and the evaluation criteria listed above offer a nuanced and comprehensive framework for assessing fine-tuned text-to-image models. Notably, these tools also enable us to evaluate other facets of model performance, such as the ability to learn multiple distinct concepts without mutual interference and the capability for parallel training of multiple models that can later be successfully merged.

5 Experiments

In this section, we perform extensive experiments to compare different LyCORIS algorithms and to assess the impact of the hyperparameters. Our experiments employ the non-EMA version of Stable Diffusion 1.5³ as the base model. All the experimental details not included in the main text along with presentations of additional experiments can be found in the appendix.

5.1 Dataset

Contrary to prior studies that primarily focus on single-concept fine-tuning with very few images, we consider a dataset that spans across a wide variety of concepts with an imbalance in the number of images for each. This corresponds to a moderate scale of fine-tuning, which is quite common in practice. Our dataset is hierarchically structured, featuring 1,706 images across five categories: anime characters, movie characters, scenes, stuffed toys, and styles. These categories further break down into various classes and sub-classes. Importantly, classes under “scenes” and “stuffed toys” contain only 4 to 12 images, whereas other categories have 45 to 200 images per class.

The influence of training captions on the fine-tuned model is also widely acknowledged in the community. It is particularly observed that training with uninformative captions such as “A photo

³<https://huggingface.co/runwayml/stable-diffusion-v1-5>

of “[V]”, which are commonly employed in the literature, can lead to subpar results. In light of this, we use a publicly available tagger⁴ to tag the training images. We then remove tags that are inherently tied to each target concept. The resulting tags are combined with the concept descriptor to create more informative captions as “[V], {tag₁}, …, {tag_k}”. To justify this choice, comparative analyses for models trained using different captions are presented in Appendix H.3.

5.2 Algorithm Configuration and Evaluation

Our experiments focus on methods that are implemented in the LyCORIS library, and notably LoRA, LoHa, LoKr, and native fine-tuning (note that DreamBooth Ruiz et al., 2023 can be simply regarded as native fine-tuning with regularization images). For each of these four algorithms, we define a set of default hyperparameters and then individually vary one of the following hyperparameters: learning rate, trained layers, dimension and alpha for LoRA and LoHa, and factor for LoKr. This leads to 26 distinct configurations. For each configuration, three models are trained using different random seeds, and three checkpoints are saved along each fine-tuning, giving in this way 234 checkpoints in the end. While other parameter-efficient fine-tuning methods exist in the literature, most of the proposed modifications are complementary to our approach. We thus do not include them for simplicity.

Data Balancing. To address dataset imbalance, we repeat each image a number of times within each epoch to ensure images from different classes are equally exposed during training.

Evaluation Procedure. To evaluate the trained models, we consider the following four types of prompts *i*) <train> training captions, *ii*) <trigger> concept descriptor alone, *iii*) <alter> generalization prompts with content alteration, and *iv*) <style> generalization prompts with style alteration. Using only the concept descriptor tests if the model can accurately reproduce the concept without using the exact training captions. As for generalization prompts, only a single target concept is involved. This thus evaluates the model’s ability to combine innate and fine-tuned knowledge. For each considered prompt type, we generate 100 images for each class or sub-class, resulting in a total of 14,900 images per checkpoint. Note that we do not include concept-agnostic prompts in our experiments.

Evaluation Metrics. Our evaluation metrics are designed to capture the criteria delineated in Section 4.2 and are computed on a per (sub)-class basis. We briefly describe below the metrics that are used for each criterion.

- **Fidelity:** We assess the similarity between the generated and dataset images using *average cosine similarity* and *squared centroid distance* between their DINOv2 embeddings (Oquab et al., 2023).
- **Controllability:** The alignment between generated images and corresponding prompts is measured via *average cosine similarity* in the CLIP feature space (Radford et al., 2021).
- **Diversity:** Diversity of images generated with a single prompt is measured by the *Vendi score* (Friedman & Dieng, 2023), calculated using the DINOv2 embeddings.
- **Base Model Preservation:** This generally needs to be evaluated on a case-by-case basis, depending on which aspect of the base model we would like to retain. Specifically, we examine potential style leakage by measuring the standard *style loss* (Johnson et al., 2016) between base and fine-tuned model outputs for <style> prompts.
- **Image Quality:** Although numerous methods have been developed for image quality assessment, most of them target natural images. As far as we are aware, currently, there still lacks a systematic approach for assessing the quality of AI-generated images. We attempted experiments with three leading pretrained quality assessment models, as detailed in Appendix H.2, but found them unsuitable for our context. We thus do not include any quality metrics in our primary experiments.

Further justification for our metric choices is provided in Appendices E and H.1, where we compute correlation coefficients for a wider range of metrics and conduct experiments across three classification datasets to assess the sensitivity of different image features to change in a certain image attribute.

⁴<https://huggingface.co/SmilingWolf/wd-v1-4-convnxt-tagger-v2>

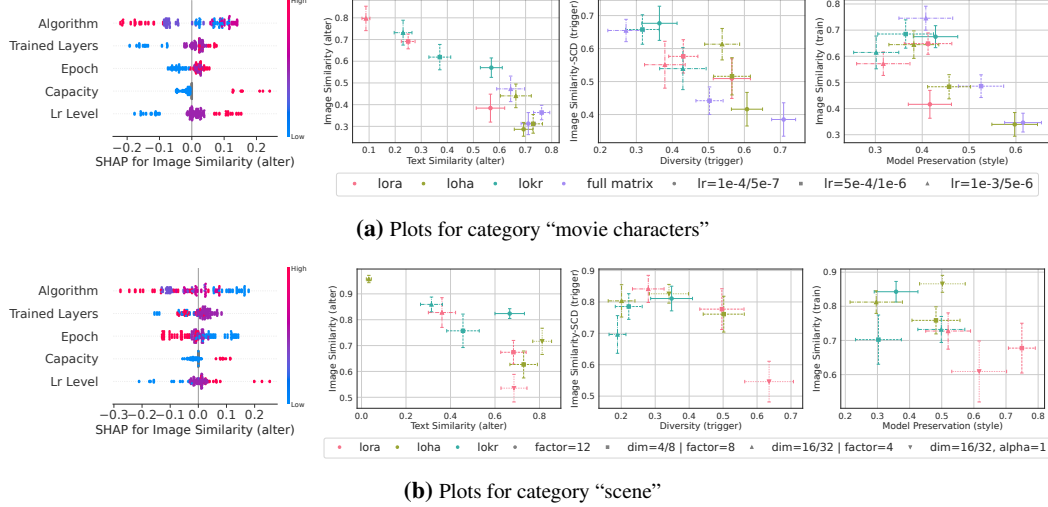


Figure 2: SHAP beeswarm charts and scatter plots for analyzing the impact of change in different algorithm components. In the beeswarm plots, LoRA is in blue, LoHa is in purple, LoKr is in purple red, and native fine-tuning is in red. Model capacity is adjusted by either increasing dimension (for LoRA or LoHa) or decreasing factor (for LoKr). In the scatter plots, SCD indicates that we use squared centroid distance to measure image similarity. This removes the implicit penalization towards more diverse image sets in the computation of average cosine similarity (see Appendix D.4 for details). We believe it is thus more suitable when we are interested in the trade-off between fidelity and diversity. The error bars in the scatter plots represent standard errors of the metric values across random seeds and classes.

5.3 Experimental Results

To carry out the analysis, we first transform each computed metric value into a normalized score, ranging from 0 to 1, based on its relative ranking among all the examined checkpoints (234 in total). A score closer to 1 signifies superior performance. Subsequently, these scores are averaged across sub-classes and classes to generate a set of metrics for each category and individual checkpoint. Alongside the scatter plots, which directly indicate the values of these metrics, we also employ SHAP (SHapley Additive exPlanations) analysis (Lundberg & Lee, 2017) in conjunction with CatBoost regressor (Prokhorenkova et al., 2018) to get a clear visualization of the impact of different algorithm components on the considered metrics, as shown in Figure 2. In essence, a SHAP value quantifies the impact of a given feature on the model’s output. For a more exhaustive presentation of the results, readers are referred to Appendix F.

5.3.1 Challenges in Algorithm Evaluation

Before delving into our analysis, it is crucial to acknowledge the complexities inherent in evaluating the performance of fine-tuning algorithms. Specifically, we identify several key challenges, including *i*) sensitivity to hyperparameters, *ii*) performance discrepancy across concepts, *iii*) influence of dataset, *iv*) conflicting criteria, and *v*) unreliability of evaluation metrics, among others. These challenges are discussed in detail in Appendix C. To mitigate some of these issues, our evaluation encompasses a large number of configurations and includes separate analyses for each category. Additionally, we complement our quantitative metrics with visual inspections conducted throughout our experiments (see Appendix G for an extensive set of qualitative results). Finally, we exercise caution in making any definitive claims, emphasizing that there is no one-size-fits-all solution, and acknowledging that exceptions do exist to our guiding principles.

5.3.2 Analysis of Results and Insights for Fine-Tuning with LyCORIS

In this part, we delve into a detailed examination of our experimental results, aiming to glean actionable insights for fine-tuning with LyCORIS. These insights should not be considered as rigid guidelines, but rather as empirical observations designed to serve as foundational reference points.

Target Concept	LoRA dim 8 alpha 4 (50 epochs)	Target Concept	Native fine-tuning (30 epochs)	
	 Attention-only Attention+MLP		 $\text{Lr } 10^{-6}$ $\text{Lr } 5 \cdot 10^{-6}$	
	 LoHa dim 4 alpha 2	 LoHa dim 16 alpha 8	 LoHa dim 16 alpha 1	 LoKr factor 8
			10 epochs	

Figure 3: Qualitative comparison of checkpoints trained with different configurations. Samples of the top row are generated using only concept descriptors while samples of the bottom row are generated with the two prompts “[V_{castle}] scene stands against a backdrop of snow-capped mountains” and “[V_{castle}] scene surrounded by a lush, vibrant forest”. The number of training epochs is chosen according to the concept category.

Number of Training Epochs. To analyze the evolution of models over training, we generate images from checkpoints obtained after 10, 30, and 50 epochs of training. Due to the small number of images available for “scenes” and “stuffed toys” categories and the use of data balancing, the 30 and 50 epoch checkpoints are almost universally overtrained for these concepts, explaining why increasing training epochs decreases image similarity as shown in the SHAP plot of Figure 2b.⁵ Otherwise, generally speaking, increasing the number of epochs improves concept fidelity but compromises text-image alignment, diversity, and base model preservation. Exceptions to this trend exist. Specifically, we observe the *overfit-then-generalize* phenomenon, as often illustrated through the double descent curve (Nakkiran et al., 2021), in certain situations. We explore this further in Appendix G.4.2.

Learning Rate. We consider three levels of learning rate, $5 \cdot 10^{-7}$, 10^{-6} , and $5 \cdot 10^{-6}$ for native fine-tuning, and 10^{-4} , $5 \cdot 10^{-4}$, and 10^{-3} for the other three algorithms. Within a reasonable range, increasing the learning rate seems to have the same effect as increasing the number of training epochs. A qualitative example is provided in Figure 3. It is worth noting, however, that an excessively low learning rate cannot be remedied by simply extending the training duration (see Appendix G.3.2).

Algorithm. A central question driving the development of LyCORIS is to assess how different methods of decomposing the model update influence the final model’s performance. From Figure 2, we observe that among the three decomposition methods, LoKr appears to outperform LoRA, which in turn outperforms LoHa, in terms of image similarity, whereas for other metrics, this ranking is typically reversed. Importantly, these observations are made under conditions where all methods have approximately the same number of parameters, and one should keep in mind that LoKr has the unique advantage of being adaptable across a wider range of potential parameter counts. Figure 2a also reveals that native fine-tuning at a learning rate of $5 \cdot 10^{-6}$ achieves high image similarity for training prompts and high text similarity for generalization prompts. However, this strong performance in text similarity for generalization prompts leads to a lower image similarity score for these prompts due to the metrics’ design. This underlines the necessity of evaluating different types of prompts independently. Lastly, we find that, native fine-tuning, when properly tuned, can achieve high text and image similarity and strong base model style preservation but often compromises diversity.

⁵We also experimented without data balancing and observed undertraining even after 50 epochs.

Trained Layers. To investigate the effects of fine-tuning different layers, we examine three distinct presets: *i*) attn-only: where we only fine-tune attention layers; *ii*) attn-mlp: where we fine-tune both attention and feedforward layers; and *iii*) full network: where we fine-tune all the layers, including the convolutional ones. As can be seen from the SHAP plots in [Figure 2](#), when all the other parameters are fixed, restricting fine-tuning to only the attention layers leads to a substantial decrease in image similarity while improving other metrics. This could be unfavorable in certain cases; for instance, the top-left example in [Figure 3](#) shows that neglecting to fine-tune the feedforward layers prevents the model from correctly learning the character’s uniform. The impact of fine-tuning the convolutional layers is less discernible, possibly because the metrics we use are not sensitive enough to capture subtle differences. Overall, our observations align with those made by [Han et al. \(2023\)](#). Moreover, it is worth noting that with the “attn-only” preset, we also fine-tune the self-attention layers in addition to the cross-attention layers, but this may still be insufficient, as demonstrated above.

Dimension, Alpha, and Factor. We finally inspect a number of parameters that are specific to our algorithms—dimension r , alpha α , and factor f . By default, we set the dimension and alpha of LoRA to 8 and 4, and of LoHa to 4 and 2. As for LoKr, we set the factor to 8 and do not perform further decomposition of the second block. These configurations result in roughly the same parameter counts across the three methods. To increase model capacity, we either increase the dimension or decrease the factor. This is what we refer to as “capacity” in the SHAP plots. We note that when the ratio between dimension and alpha is fixed, increasing model capacity has roughly the same effect as increasing learning rate or training epochs, though we expect the model’s performance could now vary more greatly when varying other hyperparameters. We especially observe in [Figure 2b](#) that the effects could be reversed when alpha is set to 1 (these checkpoints are not included in our SHAP analysis). Some qualitative comparisons are further provided in the bottom row of [Figure 3](#).

6 Concluding Remarks

In conclusion, this paper serves three main purposes. First, we introduce LyCORIS, an open-source library implementing a diverse range of methods for efficient fine-tuning of Stable Diffusion. Secondly, we advocate for a broader, more comprehensive evaluation framework that better captures the nuances of different fine-tuning methods. Lastly, our extensive experiments serve to shed light on the impact of the choice of the algorithm and their configuration on model performance, revealing their relative strengths and limitations. Interestingly, we find although both LoHa and LoKr increase the maximum matrix ranks compared to LoRA, their impact on model fine-tuning diverges, suggesting that rank may not be the best indicator to predict a method’s performance in our context.

Despite our extensive efforts, the scope of our study remains limited. For example, we have not explored the task of generating images with multiple learned concepts, as this aspect is highly sensitive to input prompts and more challenging to evaluate. However, recent works such as [Huang et al. \(2023\)](#) aim to address these issues, and we believe that incorporating these emerging evaluation frameworks will further enrich the comparison of fine-tuning methods in future studies.

Acknowledgement

We extend our heartfelt appreciation to the community for their invaluable support, which has been instrumental in bringing LyCORIS to fruition. Our particular gratitude goes to those who have directly contributed to the library and those who have further integrated it into the existing ecosystem, helping to improve and expand its functionality and reach.

References

- [1] Yuval Alaluf, Elad Richardson, Gal Metzer, and Daniel Cohen-Or. A neural space-time representation for text-to-image personalization. *arXiv preprint arXiv:2305.15391*, 2023.
- [2] Anonymous, The Danbooru Community, and Gwern Branwen. Danbooru2021: A large-scale crowdsourced and tagged anime illustration dataset, 01 2022. URL <https://www.gwern.net/Danbooru2021>. Accessed: 2022-01-28.
- [3] Eslam Mohamed Bakr, Pengzhan Sun, Xiaoqian Shen, Faizan Farooq Khan, Li Erran Li, and Mohamed Elhoseiny. HRS-Bench: Holistic, reliable and scalable benchmark for text-to-image models. *arXiv preprint arXiv:2304.05390*, 2023.
- [4] Yogesh Balaji, Seungjun Nah, Xun Huang, Arash Vahdat, Jiaming Song, Karsten Kreis, Miika Aittala, Timo Aila, Samuli Laine, Bryan Catanzaro, et al. eDiff-I: Text-to-image diffusion models with an ensemble of expert denoisers. *arXiv preprint arXiv:2211.01324*, 2022.
- [5] David Bau, Hendrik Strobelt, William Peebles, Jonas Wulff, Bolei Zhou, Jun-Yan Zhu, and Antonio Torralba. Semantic photo manipulation with a generative image prior. *ACM Transactions on Graphics (TOG)*, 38(4):1–11, 2019.
- [6] Mikołaj Bińkowski, Danica J Sutherland, Michael Arbel, and Arthur Gretton. Demystifying mmd gans. In *International Conference on Learning Representations*, 2018.
- [7] Stephen Casper, Xander Davies, Claudia Shi, Thomas Krendl Gilbert, Jérémie Scheurer, Javier Rando, Rachel Freedman, Tomasz Korbak, David Lindner, Pedro Freire, et al. Open problems and fundamental limitations of reinforcement learning from human feedback. *arXiv preprint arXiv:2307.15217*, 2023.
- [8] Arnav Chavan, Zhuang Liu, Deepak Gupta, Eric Xing, and Zhiqiang Shen. One-for-all: Generalized lora for parameter-efficient fine-tuning, 2023.
- [9] Yixiong Chen, Li Liu, and Chris Ding. X-IQE: explainable image quality evaluation for text-to-image generation with visual large language models. *arXiv preprint arXiv:2305.10843*, 2023.
- [10] Jaemin Cho, Abhay Zala, and Mohit Bansal. DALL-EVAL: Probing the reasoning skills and social biases of text-to-image generative models. *arXiv preprint arXiv:2202.04053*, 2022.
- [11] Tim Dettmers, Mike Lewis, Sam Shleifer, and Luke Zettlemoyer. 8-bit optimizers via block-wise quantization. *International Conference on Learning Representations*, 2022.
- [12] Tan M Dinh, Rang Nguyen, and Binh-Son Hua. TISE: Bag of metrics for text-to-image synthesis evaluation. In *European Conference on Computer Vision*, pp. 594–609. Springer, 2022.
- [13] Ziyi Dong, Pengxu Wei, and Liang Lin. DreamArtist: Towards controllable one-shot text-to-image generation via contrastive prompt-tuning. *arXiv preprint arXiv:2211.11337*, 2022.
- [14] DC Dowson and BV Landau. The fréchet distance between multivariate normal distributions. *Journal of multivariate analysis*, 12(3):450–455, 1982.
- [15] Ali Edalati, Marzieh Tahaei, Ivan Kobyzev, Vahid Partovi Nia, James J. Clark, and Mehdi Rezagholizadeh. KronA: Parameter efficient tuning with kronecker adapter, 2022.
- [16] Dan Friedman and Adji Bousoo Dieng. The Vendi score: A diversity evaluation metric for machine learning. *Transactions on Machine Learning Research*, 2023. ISSN 2835-8856.
- [17] Samir Yitzhak Gadre, Gabriel Ilharco, Alex Fang, Jonathan Hayase, Georgios Smyrnis, Thao Nguyen, Ryan Marten, Mitchell Wortsman, Dhruba Ghosh, Jieyu Zhang, et al. DataComp: In search of the next generation of multimodal datasets. *arXiv preprint arXiv:2304.14108*, 2023.

- [18] Rinon Gal, Yuval Alaluf, Yuval Atzmon, Or Patashnik, Amit Haim Bermano, Gal Chechik, and Daniel Cohen-or. An image is worth one word: Personalizing text-to-image generation using textual inversion. In *The Eleventh International Conference on Learning Representations*, 2023.
- [19] Rinon Gal, Moab Arar, Yuval Atzmon, Amit H Bermano, Gal Chechik, and Daniel Cohen-Or. Encoder-based domain tuning for fast personalization of text-to-image models. *ACM Transactions on Graphics (TOG)*, 42(4):1–13, 2023.
- [20] gigant. Old book illustrations, 2007. URL <https://www.oldbookillustrations.com>. Accessed: 2023-07-16.
- [21] Yuchao Gu, Xintao Wang, Jay Zhangjie Wu, Yujun Shi, Yunpeng Chen, Zihan Fan, Wuyou Xiao, Rui Zhao, Shuning Chang, Weijia Wu, et al. Mix-of-show: Decentralized low-rank adaptation for multi-concept customization of diffusion models. *arXiv preprint arXiv:2305.18292*, 2023.
- [22] Sylvain Gugger, Lysandre Debut, Thomas Wolf, Philipp Schmid, Sourab Mangrulkar Zachary Mueller, Marc Sun, and Benjamin Bossan. Accelerate: Training and inference at scale made simple, efficient and adaptable., 2022. URL <https://github.com/huggingface/accelerate>. Accessed: 2023-06-22.
- [23] Haidra-Org. Ai-horde-ratings, 2023. URL <https://huggingface.co/datasets/Haidra-Org/AI-Horde-Ratings>. Accessed: 2023-08-20.
- [24] Inhwa Han, Serin Yang, Taesung Kwon, and Jong Chul Ye. Highly personalized text embedding for image manipulation by stable diffusion. *arXiv preprint arXiv:2303.08767*, 2023.
- [25] Ligong Han, Yinxiao Li, Han Zhang, Peyman Milanfar, Dimitris Metaxas, and Feng Yang. SVDiff: Compact parameter space for diffusion fine-tuning. *arXiv preprint arXiv:2303.11305*, 2023.
- [26] Kaiming He, Xinlei Chen, Saining Xie, Yanghao Li, Piotr Dollár, and Ross Girshick. Masked autoencoders are scalable vision learners. In *Proceedings of the IEEE/CVF conference on computer vision and pattern recognition*, pp. 16000–16009, 2022.
- [27] Jack Hessel, Ari Holtzman, Maxwell Forbes, Ronan Le Bras, and Yejin Choi. Clipscore: A reference-free evaluation metric for image captioning. In *Proceedings of the 2021 Conference on Empirical Methods in Natural Language Processing*, pp. 7514–7528, 2021.
- [28] Martin Heusel, Hubert Ramsauer, Thomas Unterthiner, Bernhard Nessler, and Sepp Hochreiter. Gans trained by a two time-scale update rule converge to a local nash equilibrium. In *Advances in neural information processing systems*, volume 30, 2017.
- [29] Jonathan Ho, Ajay Jain, and Pieter Abbeel. Denoising diffusion probabilistic models. In *Advances in neural information processing systems*, volume 33, pp. 6840–6851, 2020.
- [30] V. Hosu, H. Lin, T. Sziranyi, and D. Saupe. Koniq-10k: An ecologically valid database for deep learning of blind image quality assessment. *IEEE Transactions on Image Processing*, 29: 4041–4056, 2020.
- [31] Edward J. Hu, Yelong Shen, Phillip Wallis, Zeyuan Allen-Zhu, Yuanzhi Li, Shean Wang, Lu Wang, and Weizhu Chen. LoRA: Low-rank adaptation of large language models, 2021.
- [32] Yushi Hu, Benlin Liu, Jungo Kasai, Yizhong Wang, Mari Ostendorf, Ranjay Krishna, and Noah A Smith. TIFA: Accurate and interpretable text-to-image faithfulness evaluation with question answering. *arXiv preprint arXiv:2303.11897*, 2023.

- [33] Kaiyi Huang, Kaiyue Sun, Enze Xie, Zhenguo Li, and Xihui Liu. T2I-CompBench: A comprehensive benchmark for open-world compositional text-to-image generation. *arXiv preprint arXiv:2307.06350*, 2023.
- [34] Nam Hyeon-Woo, Moon Ye-Bin, and Tae-Hyun Oh. FedPara: Low-rank hadamard product for communication-efficient federated learning. In *International Conference on Learning Representations*, 2022.
- [35] Gabriel Ilharco, Mitchell Wortsman, Ross Wightman, Cade Gordon, Nicholas Carlini, Rohan Taori, Achal Dave, Vaishaal Shankar, Hongseok Namkoong, John Miller, Hannaneh Hajishirzi, Ali Farhadi, and Ludwig Schmidt. OpenCLIP, July 2021. URL <https://doi.org/10.5281/zenodo.5143773>.
- [36] Justin Johnson, Alexandre Alahi, and Li Fei-Fei. Perceptual losses for real-time style transfer and super-resolution. In *Computer Vision–ECCV 2016: 14th European Conference, Amsterdam, The Netherlands, October 11–14, 2016, Proceedings, Part II 14*, pp. 694–711. Springer, 2016.
- [37] Tero Karras, Samuli Laine, and Timo Aila. A style-based generator architecture for generative adversarial networks. In *Proceedings of the IEEE/CVF conference on computer vision and pattern recognition*, pp. 4401–4410, 2019.
- [38] Bahjat Kawar, Shiran Zada, Oran Lang, Omer Tov, Huiwen Chang, Tali Dekel, Inbar Mosseri, and Michal Irani. Imagic: Text-based real image editing with diffusion models. In *Conference on Computer Vision and Pattern Recognition 2023*, 2023.
- [39] Yuval Kirstain, Adam Polyak, Uriel Singer, Shahbuland Matiana, Joe Penna, and Omer Levy. Pick-a-pic: An open dataset of user preferences for text-to-image generation. *arXiv preprint arXiv:2305.01569*, 2023.
- [40] Hyung-Kwon Ko, Gwanmo Park, Hyeon Jeon, Jaemin Jo, Juho Kim, and Jinwook Seo. Large-scale text-to-image generation models for visual artists’ creative works. In *Proceedings of the 28th International Conference on Intelligent User Interfaces*, pp. 919–933, 2023.
- [41] Nupur Kumari, Bingliang Zhang, Richard Zhang, Eli Shechtman, and Jun-Yan Zhu. Multi-concept customization of text-to-image diffusion. In *Proceedings of the IEEE/CVF conference on computer vision and pattern recognition*, pp. 1931–1941, 2023.
- [42] Chenliang Li, Haiyang Xu, Junfeng Tian, Wei Wang, Ming Yan, Bin Bi, Jiabo Ye, Hehong Chen, Guohai Xu, Zheng Cao, et al. mPLUG: Effective and efficient vision-language learning by cross-modal skip-connections. *arXiv preprint arXiv:2205.12005*, 2022.
- [43] Haokun Liu, Derek Tam, Mohammed Muqeeth, Jay Mohta, Tenghao Huang, Mohit Bansal, and Colin A Raffel. Few-shot parameter-efficient fine-tuning is better and cheaper than in-context learning. In *Advances in Neural Information Processing Systems*, volume 35, pp. 1950–1965, 2022.
- [44] Nan Liu, Shuang Li, Yilun Du, Antonio Torralba, and Joshua B Tenenbaum. Compositional visual generation with composable diffusion models. In *European Conference on Computer Vision*, pp. 423–439. Springer, 2022.
- [45] Zhiheng Liu, Ruili Feng, Kai Zhu, Yifei Zhang, Kecheng Zheng, Yu Liu, Deli Zhao, Jingren Zhou, and Yang Cao. Cones: Concept neurons in diffusion models for customized generation. In *International conference on machine learning*. PMLR, 2023.
- [46] Ilya Loshchilov and Frank Hutter. Decoupled weight decay regularization. In *International Conference on Learning Representations*, 2019.

- [47] Scott M Lundberg and Su-In Lee. A unified approach to interpreting model predictions. In *Advances in Neural Information Processing Systems*, volume 30. Curran Associates, Inc., 2017.
- [48] Jian Ma, Junhao Liang, Chen Chen, and Haonan Lu. Subject-diffusion: Open domain personalized text-to-image generation without test-time fine-tuning. *arXiv preprint arXiv:2307.11410*, 2023.
- [49] Henry Moss, Andrew Moore, David Leslie, and Paul Rayson. FIESTA: Fast IdEntification of state-of-the-art models using adaptive bandit algorithms. In *Proceedings of the 57th Annual Meeting of the Association for Computational Linguistics*, pp. 2920–2930, Florence, Italy, July 2019. Association for Computational Linguistics.
- [50] Preetum Nakkiran, Gal Kaplun, Yamini Bansal, Tristan Yang, Boaz Barak, and Ilya Sutskever. Deep double descent: Where bigger models and more data hurt. *Journal of Statistical Mechanics: Theory and Experiment*, 2021(12):124003, 2021.
- [51] Maxime Oquab, Timothée Darcret, Théo Moutakanni, Huy Vo, Marc Szafraniec, Vasil Khalidov, Pierre Fernandez, Daniel Haziza, Francisco Massa, Alaaeldin El-Nouby, et al. Dinov2: Learning robust visual features without supervision. *arXiv preprint arXiv:2304.07193*, 2023.
- [52] Mayu Otani, Riku Togashi, Yu Sawai, Ryosuke Ishigami, Yuta Nakashima, Esa Rahtu, Janne Heikkilä, and Shin’ichi Satoh. Toward verifiable and reproducible human evaluation for text-to-image generation. In *Proceedings of the IEEE/CVF Conference on Computer Vision and Pattern Recognition*, pp. 14277–14286, 2023.
- [53] Kishore Papineni, Salim Roukos, Todd Ward, and Wei-Jing Zhu. Bleu: a method for automatic evaluation of machine translation. In *Proceedings of the 40th annual meeting of the Association for Computational Linguistics*, pp. 311–318, 2002.
- [54] Adam Paszke, Sam Gross, Francisco Massa, Adam Lerer, James Bradbury, Gregory Chanan, Trevor Killeen, Zeming Lin, Natalia Gimelshein, Luca Antiga, et al. Pytorch: An imperative style, high-performance deep learning library. In *Advances in neural information processing systems*, volume 32, 2019.
- [55] Vitali Petriuk, Alexander E Siemann, Saisamrit Surbehera, Zad Chin, Keith Tyser, Gregory Hunter, Arvind Raghavan, Yann Hicke, Bryan A Plummer, Ori Kerret, et al. Human evaluation of text-to-image models on a multi-task benchmark. *arXiv preprint arXiv:2211.12112*, 2022.
- [56] Alethea Power, Yuri Burda, Harri Edwards, Igor Babuschkin, and Vedant Misra. Grokking: Generalization beyond overfitting on small algorithmic datasets. *arXiv preprint arXiv:2201.02177*, 2022.
- [57] Liudmila Prokhorenkova, Gleb Gusev, Aleksandr Vorobev, Anna Veronika Dorogush, and Andrey Gulin. Catboost: unbiased boosting with categorical features. In *Advances in neural information processing systems*, volume 31, 2018.
- [58] Alec Radford, Jong Wook Kim, Chris Hallacy, Aditya Ramesh, Gabriel Goh, Sandhini Agarwal, Girish Sastry, Amanda Askell, Pamela Mishkin, Jack Clark, et al. Learning transferable visual models from natural language supervision. In *International conference on machine learning*, pp. 8748–8763. PMLR, 2021.
- [59] Aditya Ramesh, Prafulla Dhariwal, Alex Nichol, Casey Chu, and Mark Chen. Hierarchical text-conditional image generation with clip latents. *arXiv preprint arXiv:2204.06125*, 1(2):3, 2022.
- [60] Edwin Arkel Rios, Wen-Huang Cheng, and Bo-Cheng Lai. DAF: Re: a challenging, crowd-sourced, large-scale, long-tailed dataset for anime character recognition. *arXiv preprint arXiv:2101.08674*, 2021.

- [61] Esther Robb, Wen-Sheng Chu, Abhishek Kumar, and Jia-Bin Huang. Few-shot adaptation of generative adversarial networks. *arXiv preprint arXiv:2010.11943*, 2020.
- [62] Daniel Roich, Ron Mokady, Amit H Bermano, and Daniel Cohen-Or. Pivotal tuning for latent-based editing of real images. *ACM Transactions on graphics (TOG)*, 42(1):1–13, 2022.
- [63] Robin Rombach, Andreas Blattmann, Dominik Lorenz, Patrick Esser, and Björn Ommer. High-resolution image synthesis with latent diffusion models. In *Proceedings of the IEEE/CVF conference on computer vision and pattern recognition*, pp. 10684–10695, 2022.
- [64] Nataniel Ruiz, Yuanzhen Li, Varun Jampani, Yael Pritch, Michael Rubinstein, and Kfir Aberman. Dreambooth: Fine tuning text-to-image diffusion models for subject-driven generation. In *Proceedings of the IEEE/CVF conference on computer vision and pattern recognition*, pp. 22500–22510, 2023.
- [65] Nataniel Ruiz, Yuanzhen Li, Varun Jampani, Wei Wei, Tingbo Hou, Yael Pritch, Neal Wadhwa, Michael Rubinstein, and Kfir Aberman. Hyperdreambooth: Hypernetworks for fast personalization of text-to-image models. *arXiv preprint arXiv:2307.06949*, 2023.
- [66] Olga Russakovsky, Jia Deng, Hao Su, Jonathan Krause, Sanjeev Satheesh, Sean Ma, Zhiheng Huang, Andrej Karpathy, Aditya Khosla, Michael Bernstein, Alexander C. Berg, and Li Fei-Fei. ImageNet Large Scale Visual Recognition Challenge. *International Journal of Computer Vision*, 115(3):211–252, 2015. doi: 10.1007/s11263-015-0816-y.
- [67] Chitwan Saharia, William Chan, Saurabh Saxena, Lala Li, Jay Whang, Emily L Denton, Kamyar Ghasemipour, Raphael Gontijo Lopes, Burcu Karagol Ayan, Tim Salimans, et al. Photorealistic text-to-image diffusion models with deep language understanding. In *Advances in Neural Information Processing Systems*, volume 35, pp. 36479–36494, 2022.
- [68] Mehdi SM Sajjadi, Olivier Bachem, Mario Lucic, Olivier Bousquet, and Sylvain Gelly. Assessing generative models via precision and recall. *Advances in neural information processing systems*, 31, 2018.
- [69] Christoph Schuhmann, Romain Beaumont, Richard Vencu, Cade Gordon, Ross Wightman, Mehdi Cherti, Theo Coombes, Aarush Katta, Clayton Mullis, Mitchell Wortsman, et al. Laion-5b: An open large-scale dataset for training next generation image-text models. In *Advances in Neural Information Processing Systems*, volume 35, pp. 25278–25294, 2022.
- [70] Jing Shi, Wei Xiong, Zhe Lin, and Hyun Joon Jung. Instantbooth: Personalized text-to-image generation without test-time finetuning. *arXiv preprint arXiv:2304.03411*, 2023.
- [71] D Amnon Silverstein and Joyce E Farrell. The relationship between image fidelity and image quality. In *Proceedings of 3rd IEEE international conference on image processing*, volume 1, pp. 881–884. IEEE, 1996.
- [72] Simo Ryu. Low-rank adaptation for fast text-to-image diffusion fine-tuning. <https://github.com/cloneofsimo/lora/>, 2022. Accessed: 2023-08-14.
- [73] K Simonyan and A Zisserman. Very deep convolutional networks for large-scale image recognition. In *International Conference on Learning Representations*. Computational and Biological Learning Society, 2015.
- [74] James Seale Smith, Yen-Chang Hsu, Lingyu Zhang, Ting Hua, Zsolt Kira, Yilin Shen, and Hongxia Jin. Continual diffusion: Continual customization of text-to-image diffusion with c-lora. *arXiv preprint arXiv:2304.06027*, 2023.
- [75] Jascha Sohl-Dickstein, Eric Weiss, Niru Maheswaranathan, and Surya Ganguli. Deep unsupervised learning using nonequilibrium thermodynamics. In *International conference on machine learning*, pp. 2256–2265. PMLR, 2015.

- [76] Jiaming Song, Chenlin Meng, and Stefano Ermon. Denoising diffusion implicit models. In *International Conference on Learning Representations*, 2021.
- [77] George Stein, Jesse C Cresswell, Rasa Hosseinzadeh, Yi Sui, Brendan Leigh Ross, Valentin Villecroze, Zhaoyan Liu, Anthony L Caterini, J Eric T Taylor, and Gabriel Loaiza-Ganem. Exposing flaws of generative model evaluation metrics and their unfair treatment of diffusion models. *arXiv preprint arXiv:2306.04675*, 2023.
- [78] Wei Ren Tan, Chee Seng Chan, Hernan Aguirre, and Kiyoshi Tanaka. Improved ArtGAN for conditional synthesis of natural image and artwork. *IEEE Transactions on Image Processing*, 28(1):394–409, 2019.
- [79] Yoad Tewel, Rinon Gal, Gal Chechik, and Yuval Atzmon. Key-locked rank one editing for text-to-image personalization. In *ACM SIGGRAPH 2023 Conference Proceedings*, pp. 1–11, 2023.
- [80] Tristan Thrush, Ryan Jiang, Max Bartolo, Amanpreet Singh, Adina Williams, Douwe Kiela, and Candace Ross. Winoground: Probing vision and language models for visio-linguistic compositionality. In *Proceedings of the IEEE/CVF Conference on Computer Vision and Pattern Recognition*, pp. 5238–5248, 2022.
- [81] Ledyard R Tucker. Some mathematical notes on three-mode factor analysis. *Psychometrika*, 31(3):279–311, 1966.
- [82] Ryan Turner, David Eriksson, Michael McCourt, Juha Kiili, Eero Laaksonen, Zhen Xu, and Isabelle Guyon. Bayesian optimization is superior to random search for machine learning hyperparameter tuning: Analysis of the black-box optimization challenge 2020. In Hugo Jair Escalante and Katja Hofmann (eds.), *Proceedings of the NeurIPS 2020 Competition and Demonstration Track*, volume 133 of *Proceedings of Machine Learning Research*, pp. 3–26. PMLR, 06–12 Dec 2021.
- [83] Mojtaba Valipour, Mehdi Rezagholizadeh, Ivan Kobyzev, and Ali Ghodsi. DyLoRA: Parameter efficient tuning of pre-trained models using dynamic search-free low rank adaptation, 2022.
- [84] Ramakrishna Vedantam, C Lawrence Zitnick, and Devi Parikh. Cider: Consensus-based image description evaluation. In *Proceedings of the IEEE conference on computer vision and pattern recognition*, pp. 4566–4575, 2015.
- [85] Patrick von Platen, Suraj Patil, Anton Lozhkov, Pedro Cuenca, Nathan Lambert, Kashif Rasul, Mishig Davaadorj, and Thomas Wolf. Diffusers: State-of-the-art diffusion models. <https://github.com/huggingface/diffusers>, 2022. Accessed: 2023-06-22.
- [86] Andrey Voynov, Qinghao Chu, Daniel Cohen-Or, and Kfir Aberman. $p+$: Extended textual conditioning in text-to-image generation. *arXiv preprint arXiv:2303.09522*, 2023.
- [87] Hongyi Wang, Saurabh Agarwal, and Dimitris Papailiopoulos. Pufferfish: Communication-efficient models at no extra cost. *Proceedings of Machine Learning and Systems*, 3:365–386, 2021.
- [88] Yaxing Wang, Chenshen Wu, Luis Herranz, Joost Van de Weijer, Abel Gonzalez-Garcia, and Bogdan Raducanu. Transferring gans: generating images from limited data. In *Proceedings of the European Conference on Computer Vision (ECCV)*, pp. 218–234, 2018.
- [89] Zijie J. Wang, Evan Montoya, David Munechika, Haoyang Yang, Benjamin Hoover, and Duen Horng Chau. DiffusionDB: A large-scale prompt gallery dataset for text-to-image generative models. *arXiv:2210.14896*, 2022.
- [90] Yuxiang Wei, Yabo Zhang, Zhilong Ji, Jinfeng Bai, Lei Zhang, and Wangmeng Zuo. Elite: Encoding visual concepts into textual embeddings for customized text-to-image generation. *arXiv preprint arXiv:2302.13848*, 2023.

- [91] Ross Wightman. Pytorch image models. <https://github.com/huggingface/pytorch-image-models>, 2019. Accessed: 2023-08-14.
- [92] Thomas Wolf, Lysandre Debut, Victor Sanh, Julien Chaumond, Clement Delangue, Anthony Moi, Pierrick Cistac, Tim Rault, Rémi Louf, Morgan Funtowicz, et al. Transformers: State-of-the-art natural language processing. In *Proceedings of the 2020 conference on empirical methods in natural language processing: system demonstrations*, pp. 38–45, 2020.
- [93] Sanghyun Woo, Shoubhik Debnath, Ronghang Hu, Xinlei Chen, Zhuang Liu, In So Kweon, and Saining Xie. Convnext v2: Co-designing and scaling convnets with masked autoencoders. In *Proceedings of the IEEE/CVF conference on computer vision and pattern recognition*, pp. 16133–16142, 2023.
- [94] Xiaoshi Wu, Yiming Hao, Keqiang Sun, Yixiong Chen, Feng Zhu, Rui Zhao, and Hongsheng Li. Human preference score v2: A solid benchmark for evaluating human preferences of text-to-image synthesis. *arXiv preprint arXiv:2306.09341*, 2023.
- [95] Jiazheng Xu, Xiao Liu, Yuchen Wu, Yuxuan Tong, Qinkai Li, Ming Ding, Jie Tang, and Yuxiao Dong. Imagereward: Learning and evaluating human preferences for text-to-image generation. *arXiv preprint arXiv:2304.05977*, 2023.
- [96] Tao Xu, Pengchuan Zhang, Qiuyuan Huang, Han Zhang, Zhe Gan, Xiaolei Huang, and Xiaodong He. AttnGAN: Fine-grained text to image generation with attentional generative adversarial networks. In *Proceedings of the IEEE conference on computer vision and pattern recognition*, pp. 1316–1324, 2018.
- [97] Sidi Yang, Tianhe Wu, Shuaiwei Shi, Shanshan Lao, Yuan Gong, Mingdeng Cao, Jiahao Wang, and Yujiu Yang. ManiqA: Multi-dimension attention network for no-reference image quality assessment. In *Proceedings of the IEEE/CVF Conference on Computer Vision and Pattern Recognition*, pp. 1191–1200, 2022.
- [98] Joe Young. Star Wars dataset, 2019. URL <https://www.kaggle.com/datasets/jsphyg/star-wars>. Accessed: 2023-07-16.
- [99] Mert Yuksekgonul, Federico Bianchi, Pratyusha Kalluri, Dan Jurafsky, and James Zou. When and why vision-language models behave like bags-of-words, and what to do about it? In *International Conference on Learning Representations*, 2023.
- [100] Chenshuang Zhang, Chaoning Zhang, Mengchun Zhang, and In So Kweon. Text-to-image diffusion model in generative ai: A survey. *arXiv preprint arXiv:2303.07909*, 2023.
- [101] Lvmin Zhang, Anyi Rao, and Maneesh Agrawala. Adding conditional control to text-to-image diffusion models. In *IEEE International Conference on Computer Vision (ICCV)*, 2023.
- [102] Weixia Zhang, Guangtao Zhai, Ying Wei, Xiaokang Yang, and Kede Ma. Blind image quality assessment via vision-language correspondence: A multitask learning perspective. In *IEEE Conference on Computer Vision and Pattern Recognition*, pp. 14071–14081, 2023.
- [103] Deyao Zhu, Jun Chen, Xiaoqian Shen, Xiang Li, and Mohamed Elhoseiny. Minigpt-4: Enhancing vision-language understanding with advanced large language models. *arXiv preprint arXiv:2304.10592*, 2023.

Appendix

Table of Contents

A Related Works	19
B Further Discussion on Implemented Algorithms	21
B.1 Effect of Merge Ratio	22
B.2 Tucker Decomposition of Convolutional Layers	23
B.3 LoKr as Consecutive Linear Layers	24
C Challenges in Algorithm Evaluation	25
D Experimental Details	26
D.1 Dataset	26
D.2 Algorithm Configuration and Hardware	29
D.3 Evaluation Prompts	29
D.4 Evaluation Metrics	30
D.5 Encoders	33
D.6 Metric Value Processing	33
E Correlation Analysis	34
E.1 Influence of Encoders, Resizing Methods, and Prompt Types	34
E.2 Relation between Different Metrics	35
F Supporting Plots	36
F.1 Plots for Category “Movie Characters”	37
F.2 Plots for Category “Scenes”	39
F.3 Plots for Category “Stuffed Toys”	41
F.4 Plots for Category “Anime Characters”	43
F.5 Plots for Category “Styles”	45
G Further Qualitative Results	47
G.1 Discrepancy of Results Across Classes	47
G.2 Unreliability of Metrics	47
G.3 Illustrating the Impact of Different Algorithm Components	47
G.4 Violations of the General Principles	56
G.5 Example Generations for Category “Styles”	64
H Additional Experiments	69
H.1 Investigating the Relevance of Image Features	69
H.2 Image Quality Assessment with Pretrained Models	71
H.3 Impact of Captioning Strategies on Model Performance	73
I Author Contributions	77

A Related Works

In this section, we review related works for two interconnected themes that are vital to our study: text-to-image model customization and text-to-image model evaluation.

Model Customization. There has been a long-standing effort in adapting pretrained deep generative models to learn new concepts with limited data (Bau et al., 2019; Robb et al., 2020; Roich et al., 2022; Wang et al., 2018), but the surge of Stable Diffusion and similar large-scale text-to-image generation models have accelerated this progress. Specifically, DreamBooth (Ruiz et al., 2023) proposes fine-tuning the U-Net with a prior-preservation loss, which serves as the regularizer in combating overfitting and improving the generation performance. Another pioneering work in this direction is Textual Inversion (TI) (Gal et al., 2023), which instead optimizes the input text embedding vector with the subject images and uses that optimized text embedding for generation.

Expanding on the initial concept of pivotal tuning (Roich et al., 2022) for StyleGAN (Karras et al., 2019), other works have explored concurrent fine-tuning of both text embeddings and network architectures for diffusion models (Gu et al., 2023; Kawar et al., 2023; Kumari et al., 2023; Smith et al., 2023; Tewel et al., 2023). For instance, Imagic by Kawar et al. (2023) targets single-image editing by initially optimizing the text embedding for a given input before further network fine-tuning. On the other hand, Custom Diffusion (Kumari et al., 2023) and Perfusion (Tewel et al., 2023) both focus on fine-tuning only the K-V cross-attention layers to reduce overfitting but adopt different strategies. Custom Diffusion considers native fine-tuning of these layers and offers a way to merge fine-tuned models without additional training, while Perfusion employs a more complex gated mechanism and “locks” the K pathway using class-specific words, thereby enhancing the model’s capacity to generate learned concepts across diverse contexts.

Efforts have also been made to address more specific challenges. For example, C-LoRA (Smith et al., 2023) addresses the issue of catastrophic forgetting through a self-regularization mechanism while fine-tuning the K-V cross-attention layers with LoRAs. In parallel, ED-LoRA (Gu et al., 2023) employs LoRA dropout to counterbalance the otherwise dominant influence of LoRA in the learning process, ensuring that the embeddings remain a significant component of concept learning.

Alongside these focused endeavors, there has been complementary progress in expanding and improving upon Textual Inversion. Notably, Voynov et al. (2023) introduced Extended Textual Inversion (XTI), a layer-wise embedding method that was also used in ED-LoRA. Another noteworthy innovation is DreamArtist (Dong et al., 2022), which leverages positive and negative embeddings for efficient one-shot model customization. Further improvements to the TI framework include the works by Alaluf et al. (2023); Han et al. (2023).

While TI-based methods often struggle to generate concepts outside of the pretrained models’ domain (Gu et al., 2023; Smith et al., 2023), they do offer an advantage in terms of parameter efficiency. Specifically, the number of stored parameters required by these methods is orders of magnitude smaller than those necessitated by most network fine-tuning methods. This gap is partially bridged by SVDiff (Han et al., 2023) and Cones (Liu et al., 2023). The former optimizes singular values of the weight matrices of the network, which leads to a compact and efficient parameter space that reduces the risk of overfitting and language-drifting. The latter proposes to focus on concept neurons, a small set of parameters of the K-V attention layers, which are posited to be sufficient to encode the target concept in an ideal scenario. Remarkably, several methods implemented in our LyCORIS library, such as LoKr and (IA)³ can also result in weight updates with parameter counts that are comparable to these methods.

A partial summary of the related works in text-to-image diffusion model customization is provided in [Table 1](#). This table shows that even though these methods may focus on optimizing different components involved in the image generation process, they often introduce new techniques that can be integrated in a complementary fashion. For example, elements like the positive and negative guiding introduced in DreamArtist can be effectively coupled with algorithms implemented in our LyCORIS library. Furthermore, other techniques, such as the layer-wise embeddings in XTI and

Method	K-V	Linear	Conv	TE	Emb	PP Loss	Further Innovations
DreamBooth [64]	✓	✓	✓			✓	
Textual Inversion [18]					✓		
DreamArtist [13]					✓		Positive and Negative Embeddings
XTI [86]					✓		Layer-Wise Embeddings
Custom Diffusion [41]	✓				✓	✓	Model Fusion Technique
C-LoRA [74]	✓				✓	✓	Self-Regularization for Continual Learning
Perfusion [79]	✓				✓		Key-Locking, Gated Rank-1 Update
Cones [45]	✓					✓	Concept Neurons
SVDiff [25]	✓	✓	✓			✓	Fine-Tune Singular Values, Cut-Mix-Unmix
ED-LoRA [21]	✓	-		✓	✓		XTI + LoRA Dropout, Gradient Fusion
LyCORIS (ours)	✓	✓	✓	✓			LoHa, LoKr, etc.

Table 1: A brief recapitulation for the functioning of different existing diffusion model fine-tuning strategies. K-V, Linear, Conv, TE, Emb, and PP Loss respectively stand for K-V cross-attention layers, linear layers in attention and feed-forward blocks in U-Net, convolutional layers, text encoder, embedding, and prior-preservation loss. We put a checkmark when the corresponding block is optimized or when the corresponding mechanism is employed. ED-LoRA fine-tunes linear layers within attention blocks, and this is why we put - instead of a checkmark. For LyCORIS, we focus on the setup of this paper, but in reality, we have the liberty to decide which part to fine-tune and whether to use prior-preservation loss or not. Note for the “further innovations” column, we only include the main contributions from each work and further details concerning the implementation of each method are omitted (for example, Textual Inversion also considers an additional regularization term and progressive extensions, while Perfusion weights the diffusion reconstruction loss by a soft segmentation mask).

key-locking from Perfusion, can also be incorporated concurrently. Collectively, these innovations thus form a robust toolkit conducive to the fine-tuning of text-to-image diffusion models.

Finally, there exists a distinct line of research that aims to facilitate test-time adaptation without the need for further fine-tuning (see e.g., Gal et al., 2023; Ma et al., 2023; Ruiz et al., 2023; Shi et al., 2023; Wei et al., 2023). In these cases, we need to train separate networks or additional modules, using larger and more diverse datasets that encompass data from a single domain or multiple domains. As a result, the adaptability of these models is generally confined to the domains encountered during training. While such methods are useful for specialized, ad-hoc applications where users might want to generate variations of a target concept with a limited set of input images, they don’t offer the broad applicability inherent to direct fine-tuning strategies.

Model Evaluation. The evaluation of generative models has been a central concern since the inception of these models. Early efforts focused on measuring the distance between the data distribution and the distribution learned by the models, utilizing metrics like FID (Heusel et al., 2017), KID (Bińkowski et al., 2018), and Precision-Recall (Sajjadi et al., 2018) which have been widely adopted in the community. Meanwhile, the limitations of these metrics are increasingly being recognized, as detailed by Stein et al. (2023), who critically examined the flaws of various metrics used for evaluating generative models. In our context, these metrics are primarily useful for evaluating the concept fidelity of the generated images on the condition that we have a sufficiently large training set.

Another dimension comes into the scene when considering text-to-image models. In such scenarios, assessing the text-image alignment of generated images becomes crucial. Commonly used metrics for this purpose include CLIPScore (Hessel et al., 2021), R-precision (Xu et al., 2018), and BLEU (Papineni et al., 2002) or CIDEr (Vedantam et al., 2015) for evaluating the similarity between the captions generated for the synthesized images and the original text prompts. To enhance interpretability and enable finer-grained evaluation, recent works like TIFA (Hu et al., 2023) and X-IQE (Chen et al., 2023) have also explored the use of pretrained large vision-language models such as mPLUG (Li et al., 2022) and MiniGPT-4 (Zhu et al., 2023). Together with image fidelity/quality, these represent the two main aspects on which text-to-image models are typically evaluated (Dinh et al., 2022; Saharia et al., 2022). Notably, nearly all the text-to-image model customization studies we have discussed have limited their quantitative evaluations to these two sets of metrics.

Yet, the need for going beyond these two aspects has also been acknowledged. Specifically, other criteria such as visual reasoning, social bias, and creativity have been considered in DALL-EVAL (Cho et al., 2022) and HRS-Bench (Bakr et al., 2023). While some of these can be regarded as the design of more dedicated metrics to measure text-image alignment in particular situations, others necessitate a completely different attack angle.

Importantly, all the previous works focus exclusively on the evaluation of general text-to-image models, while we zoom in on the evaluation of fine-tuned models. Although we can borrow metrics and criteria from these works, certain nuances exist. For example, as discussed in Section 4, we may want to ensure that new concepts do not adversely affect the innate knowledge of the original model, and image fidelity, image quality, and aesthetics should be evaluated independently (Silverstein & Farrell, 1996). Moreover, we separate how the model is prompted (or how it is used more generally) from how the generated images are evaluated, which together define the so-called “skills” in the aforementioned papers. On top of this, we identify a few key aspects that could be the most affected by model fine-tuning. That said, the metrics that we currently employ remain relatively rudimentary, and integrating more advanced metrics from the literature would undoubtedly be beneficial.

Complementary to automatic evaluation, human evaluation is generally considered to yield the most accurate assessments of model performance. Recent initiatives in this area include the works of Otani et al. (2023); Petsiuk et al. (2022). In particular, Otani et al. (2023) introduced a well-defined protocol for human evaluation to ensure verifiable and reproducible results. Nonetheless, most studies employing human evaluations compare a limited set of models using relatively few generated samples and evaluation criteria. Given the scale of our work, which involves hundreds of trained checkpoints and millions of generated images, conducting a comprehensive human evaluation would incur prohibitive costs, both in terms of time and resources. Therefore, we have opted to omit human evaluations from this study. In the meantime, we believe that methods from the fields of multi-armed bandits and Bayesian optimization may offer promising avenues for tackling the scalability challenges of human evaluation (Moss et al., 2019; Turner et al., 2021).

As another avenue for exploration, several datasets have been introduced to capture human preferences for AI-generated images (Kirstain et al., 2023; Wu et al., 2023; Xu et al., 2023). These datasets pave the way for training human preference models, which could further be used for evaluation and for fine-tuning text-to-image models for closer alignment with human preferences (Xu et al., 2023). However, one should note that human preference represents just one facet in a multi-dimensional evaluation landscape and is often more tied to the dataset than the training algorithm itself. Moreover, as Casper et al. (2023) aptly points out, “A single reward function cannot represent a diverse society of humans”. Over-reliance on such a reward function could inadvertently marginalize or overlook the preferences and needs of under-represented groups, thus reinforcing existing biases and inequalities.

B Further Discussion on Implemented Algorithms

This appendix discusses finer details of the algorithms implemented in our study. We especially focus on the effect of the merge ratio on training dynamics, Tucker decomposition of convolutional layers, and the interpretation of LoKr as a number of consecutive linear layers.

B.1 Effect of Merge Ratio

In this section, we demonstrate an equivalence between scaling the merge ratio and scaling the initialization parameters and the learning rates. For simplicity, we will write $\mathbf{h}' = W_0 \mathbf{h} + \mathbf{b}$ to represent the transformation performed by all types of layers in the neural network, whatever we deal with convolutional or linear layers. Our result holds in a general setup in which each layer, identified by the index ℓ , can use its own distinct decomposition function T_ℓ and merge ratio γ_ℓ .

Formally, we assume that the forward pass of layer ℓ is modified to

$$\mathbf{h}'_\ell = W_{\ell,0} \mathbf{h}_\ell + \mathbf{b}_\ell + \gamma_\ell \Delta W_\ell \mathbf{h}_\ell = W_{\ell,0} \mathbf{h}_\ell + \mathbf{b}_\ell + \gamma_\ell T_\ell(A_{\ell,1}, \dots, A_{\ell,m_\ell}) \mathbf{h}_\ell, \quad (6)$$

where $A_{\ell,1}, \dots, A_{\ell,m_\ell}$ are a set of tensors that together define the weight update ΔW_ℓ . In LyCORIS, the decomposition function T_ℓ is mainly composed of low rank decomposition, Hadarmard decomposition, and Kronecker decomposition. However, other decomposition functions such as Tucker decomposition (Tucker, 1966) can also be used (see [Appendix B.2](#)). The effect of the merge ratios $\gamma = (\gamma_\ell)_\ell$ is stated in the following theorem.

Theorem 1. *Assume that we train a neural network with forward pass modified as in (6) and that every T_ℓ is homogeneous, i.e., for all $a \in \mathbb{R}$ and all possible input $A_{\ell,1}, \dots, A_{\ell,m_\ell}$, we have*

$$T_\ell(aA_{\ell,1}, \dots, aA_{\ell,m_\ell}) = a^{m_\ell} T_\ell(A_{\ell,1}, \dots, A_{\ell,m_\ell}). \quad (7)$$

Then, replacing γ_ℓ by 1 in (6), scaling the initialization parameters and learning rate of each layer ℓ respectively by $(\gamma_\ell)^{\frac{1}{m_\ell}}$ and $(\gamma_\ell)^{\frac{c}{m_\ell}}$ is mathematically equivalent to training with the original initialization parameters, learning rates, and merge ratios. Here, $c = 2$ if we train with stochastic gradient descent (SGD), and $c = 1$ if we train with Adam, RMSProp, or AdaGrad with the ε parameter set to 0.

Proof. Let \mathcal{L} be the loss function for a specific step when the network is parameterized with $(\Delta W_\ell)_\ell$. Note that this loss function is different from the one defined in [Section 2.1](#), and in particular, it depends on the data sampled at each step, and also the sampled noise and sampled diffusion step in the case of diffusion model. Similarly, for any $\gamma = (\gamma_\ell)_\ell$, we define $\tilde{\mathcal{L}}^\gamma$ as the loss function of the same step (i.e., resulting from the same sampled data, noise, diffusion step etc.) but with respect to the tensors $\mathbf{A} = (A_{\ell,i})_{\ell,i}$ when the forward pass is modified following (6). By defining

$$\mathbf{T}^\gamma: \mathbf{A} \rightarrow (\Delta W_\ell)_\ell = (\gamma_\ell T_\ell(A_{\ell,1}, \dots, A_{\ell,m_\ell}))_\ell, \quad (8)$$

as the function that maps the decomposed tensors to weight updates, we have clearly $\tilde{\mathcal{L}}^\gamma = \mathcal{L} \circ \mathbf{T}^\gamma$. To simplify the notation, we further write $\tilde{\mathcal{L}} = \tilde{\mathcal{L}}^1$ and $\mathbf{T} = \mathbf{T}^1$. We claim that

$$\nabla_{\mathbf{A}_\ell} \tilde{\mathcal{L}}^\gamma(\mathbf{A}) = (\gamma_\ell)^{\frac{1}{m_\ell}} \nabla_{\mathbf{A}_\ell} \tilde{\mathcal{L}}(\gamma^{\frac{1}{m}} \cdot \mathbf{A}). \quad (9)$$

In the above, $\mathbf{A}_\ell = (A_{\ell,i})_i$ collects the decomposed tensors of layer ℓ , $\nabla_{\mathbf{A}_\ell}$ represents the gradient with respect to these tensors, and $\gamma^{\frac{1}{m}} \cdot \mathbf{A} = ((\gamma_\ell)^{\frac{1}{m_\ell}} \mathbf{A}_\ell)_\ell$ is obtained from scaling all the tensors by a layer-dependent scalar $(\gamma_\ell)^{\frac{1}{m_\ell}}$. For ease of mathematical treatment, it is convenient to consider both the inputs and outputs of functions \mathcal{L} , $\tilde{\mathcal{L}}^\gamma$, and \mathbf{T}^γ as one-dimensional vectors, which are formed by flattening the tensors and then concatenating them. Lastly, by slight abuse of notation, we use \mathbf{A}_ℓ for both the variable and the value at which we evaluate the gradient.

To prove (9), we first apply chain rule to get

$$\begin{aligned} \nabla \tilde{\mathcal{L}}^\gamma(\mathbf{A})^\top &= \nabla \mathcal{L}(\mathbf{T}^\gamma(\mathbf{A}))^\top \text{Jac}_{\mathbf{T}^\gamma}(\mathbf{A}), \\ \nabla \tilde{\mathcal{L}}(\gamma^{\frac{1}{m}} \cdot \mathbf{A})^\top &= \nabla \mathcal{L}(\mathbf{T}(\gamma^{\frac{1}{m}} \cdot \mathbf{A}))^\top \text{Jac}_{\mathbf{T}}(\gamma^{\frac{1}{m}} \cdot \mathbf{A}), \end{aligned} \quad (10)$$

where Jac_T represents the Jacobian matrix of operator T . Note that by the definition of \mathbf{T}^γ , input variable $A_{\ell,i}$ only affects output variable ΔW_ℓ , and thus $\text{Jac}_{\mathbf{T}^\gamma}(\mathbf{A})$ is blockwise diagonal. This indicates that (10) can be written in a layer-wise way as following.

$$\begin{aligned} \nabla_{\mathbf{A}_\ell} \tilde{\mathcal{L}}^\gamma(\mathbf{A})^\top &= \nabla_{\Delta W_\ell} \mathcal{L}(\mathbf{T}^\gamma(\mathbf{A}))^\top \text{Jac}_{\gamma_\ell T_\ell}(\mathbf{A}_\ell), \\ \nabla_{\mathbf{A}_\ell} \tilde{\mathcal{L}}(\gamma^{\frac{1}{m}} \cdot \mathbf{A})^\top &= \nabla_{\Delta W_\ell} \mathcal{L}(\mathbf{T}(\gamma^{\frac{1}{m}} \cdot \mathbf{A}))^\top \text{Jac}_{T_\ell}((\gamma_\ell)^{\frac{1}{m_\ell}} \mathbf{A}_\ell). \end{aligned} \quad (11)$$

Since each T_ℓ is homogeneous, it holds that

$$\gamma_\ell T_\ell(\mathbf{A}_\ell) = T_\ell((\gamma_\ell)^{\frac{1}{m_\ell}} \mathbf{A}_\ell). \quad (12)$$

Differentiating both sides with respect to \mathbf{A}_ℓ gives immediately

$$\text{Jac}_{\gamma_\ell T_\ell}(\mathbf{A}_\ell) = (\gamma_\ell)^{\frac{1}{m_\ell}} \text{Jac}_{T_\ell}((\gamma_\ell)^{\frac{1}{m_\ell}} \mathbf{A}_\ell). \quad (13)$$

On the other hand, it also follows from (12) that

$$\mathbf{T}^\gamma(\mathbf{A}) = \mathbf{T}(\gamma^{\frac{1}{m}} \cdot \mathbf{A}). \quad (14)$$

Plugging (13) and (14) into (11) gives immediately (9).

To complete the proof, we just need to note that an important difference between AdaGrad-type methods and vanilla SGD is in whether the learning rates are scaled by some scalar computed based on gradient magnitude or not. This is not the case for SGD, and we can simply write

$$(\gamma_\ell)^{\frac{1}{m_\ell}} (\mathbf{A}_\ell - \eta_\ell \nabla_{\mathbf{A}_\ell} \tilde{\mathcal{L}}^\gamma(\mathbf{A})) = (\gamma_\ell)^{\frac{1}{m_\ell}} \mathbf{A}_\ell - \eta_\ell (\gamma_\ell)^{\frac{2}{m_\ell}} \nabla_{\mathbf{A}_\ell} \tilde{\mathcal{L}}(\gamma^{\frac{1}{m}} \cdot \mathbf{A}), \quad (15)$$

where η_ℓ is the learning rate of layer ℓ . This shows that if for each layer ℓ , we scale the initialized parameters by $(\gamma_\ell)^{\frac{1}{m_\ell}}$ and learning rate by $(\gamma_\ell)^{\frac{2}{m_\ell}}$, while setting the merge ratio to 1, then after each stochastic gradient step we still have $\mathbf{A}^2 = \gamma^{\frac{1}{m}} \cdot \mathbf{A}^1$. Here, \mathbf{A}^1 and \mathbf{A}^2 are respectively the tensors obtained from the updates with merge ratio γ and merge ratio 1 but with scaled initialization and learning rates. Together with (14) we then see that the two approaches lead to the same weight update $(\Delta W_\ell)_\ell$ at the end.

As for Adam, RMSProp, and AdaGrad, when ε is set to 0, the scaling of the learning rate causes the two versions to have the same scaled update vector. In other words, instead of having a relation like (9), the update is performed with the same vector \mathbf{d} . One has clearly

$$(\gamma_\ell)^{\frac{1}{m_\ell}} (\mathbf{A}_\ell - \eta_\ell \mathbf{d}) = (\gamma_\ell)^{\frac{1}{m_\ell}} \mathbf{A}_\ell - \eta_\ell (\gamma_\ell)^{\frac{1}{m_\ell}} \mathbf{d}. \quad (16)$$

This shows that one should rather scale the learning rate by $(\gamma_\ell)^{\frac{1}{m_\ell}}$ in this case to maintain the relation $\mathbf{A}^2 = \gamma^{\frac{1}{m}} \cdot \mathbf{A}^1$, concluding the proof. \square

While [Theorem 1](#) provides an intuitive way to understand how the merge ratio γ , or the related α affects training, it is crucial to keep in mind that these quantities were specifically introduced by [Hu et al. \(2021\)](#) to address numerical precision issues. In fact, if we were to simply scale the initialization parameters and learning rates instead of using the merge ratios, the stored parameters in the decomposed tensors would be much smaller. This could lead to numerical instability or reduced precision during the optimization process, potentially affecting the model's training and final performance adversely.

B.2 Tucker Decomposition of Convolutional Layers

In this section, we elaborate on how Tucker decomposition ([Tucker, 1966](#)) is applied to the convolutional layers in order to achieve higher computational and memory efficiency.

To begin, let us denote by \times_n the n -mode product which computes the matrix product on dimension n of a tensor while casting over the remaining dimensions. Formally, for $G = (g_{i_1 \dots i_d}) \in \mathbb{R}^{I_1 \times \dots \times I_d}$ a tensor of order d and $A = (a_{i_n j_n}) \in \mathbb{R}^{I_n \times J_n}$ a matrix of size $I_n \times J_n$, their n -mode product $G \times_n A \in \mathbb{R}^{I_1 \times \dots \times I_{n-1} \times J_n \times I_{n+1} \times \dots \times I_d}$ has its elements given by

$$(G \times_n A)_{i_1 \dots i_{n-1} j_n i_{n+1} \dots i_d} = \sum_{i_n=1}^{I_n} g_{i_1 \dots i_{n-1} i_n i_{n+1} \dots i_d} a_{i_n j_n}. \quad (17)$$

With this in mind, Tucker decomposition is simply the decomposition of a tensor into a set of matrices and a small core tensor using n -mode product.

In the context of fine-tuning convolutional layers, we can apply Tucker decomposition to decompose the weight update $\Delta W \in \mathbb{R}^{c_{\text{out}} \times c_{\text{in}} \times k \times k}$ into one core tensor $G \in \mathbb{R}^{r \times r \times k \times k}$ and two matrices

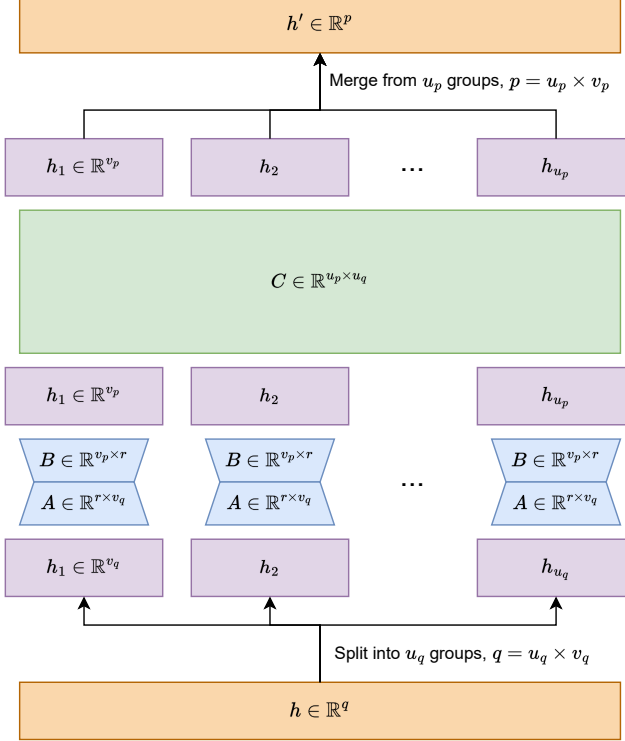


Figure 4: This figure shows how to represent LoKr as two or three linear layers (depending on whether we perform the additional low-rank decomposition or not).

$B \in \mathbb{R}^{r \times c_{\text{out}}}$, $A \in \mathbb{R}^{r \times c_{\text{in}}}$, leading to

$$\mathbf{h}' = W_0 * \mathbf{h} + \mathbf{b} + \gamma(G \times_1 B \times_2 A) * \mathbf{h}. \quad (18)$$

Compared to the approach elaborated in [Section 3.2](#), the number of parameters changes from $r(c_{\text{in}}k^2 + c_{\text{out}})$ to $r(rk^2 + c_{\text{in}} + c_{\text{out}})$. The latter is substantially smaller when $r \ll c_{\text{in}}(1 - 1/k^2)$.

Importantly, the tensor G can also be interpreted as a convolutional kernel with in-channels and out-channels both set to r . To recast this decomposition as three convolutional layers (two of them have $k = 1$), we first reshape B^\top and A respectively into $\tilde{B} \in \mathbb{R}^{c_{\text{out}} \times r \times 1 \times 1}$ and $\tilde{A} \in \mathbb{R}^{r \times c_{\text{in}} \times 1 \times 1}$. The forward pass then becomes

$$\mathbf{h}' = W_0 * \mathbf{h} + \mathbf{b} + \tilde{B} * (G * (\tilde{A} * \mathbf{h})). \quad (19)$$

Tucker decomposition was also adopted in FedPara ([Hyeon-Woo et al., 2022](#)) for decomposing convolutional layers' kernels. We borrow their methods and implement it for LoHa. In this case, the forward pass is modified to

$$\mathbf{h}' = W_0 * \mathbf{h} + \mathbf{b} + \gamma(G_1 \times_1 B_1 \times_2 A_1) \odot (G_2 \times_1 B_2 \times_2 A_2) * \mathbf{h}, \quad (20)$$

where $G_1, G_2 \in \mathbb{R}^{r \times r \times k \times k}$, $B_1, B_2 \in \mathbb{R}^{r \times c_{\text{out}}}$, and $A_1, A_2 \in \mathbb{R}^{r \times c_{\text{in}}}$. The decomposition for convolutional layers in LoKr follows the same methodology.

B.3 LoKr as Consecutive Linear Layers

For a more intuitive understanding of LoKr, we introduce here a unique representation for $\Delta \mathbf{h} = (C \otimes BA)\mathbf{h}$ that effectively models it as a sequence three linear layers. The core mechanism for this representation is the use of the mixed Kronecker matrix-vector product property. Consider the linear transformation $\Delta \mathbf{h} = \Delta W \mathbf{h}$, where $\mathbf{h} \in \mathbb{R}^q$, $\Delta \mathbf{h} \in \mathbb{R}^p$ and $\Delta W \in \mathbb{R}^{p \times q}$. The weight update ΔW is further decomposed as $\Delta W = C \otimes BA$ with $C \in \mathbb{R}^{u_p \times u_q}$, $B \in \mathbb{R}^{v_p \times r}$, and $A \in \mathbb{R}^{r \times v_q}$.

Algorithm 1 PyTorch-style pseudocode for LoKr as linear layers

```
1: def lokr_linear(h, a, b, c):
2:     vq = a.size(1)
3:     uq = c.size(1)
4:     h_in_group = rearrange(
5:         h,
6:         "b ... (uq vq) -> b ... uq vq",
7:         uq=uq, vq=vq
8:     )
9:     ha = F.linear(h_in_group, a)
10:    hb = F.linear(ha, b)
11:    h_cross_group = hb.transpose(-1, -2)
12:    hc = F.linear(h_cross_group, c)
13:    h = rearrange(hc, "b ... vp up -> b ... (up vp)")
14:    return h
```

Utilizing the mixed Kronecker matrix-vector product property, we can express this as

$$\begin{aligned}\Delta \mathbf{h} &= \Delta W \mathbf{h} \\ &= (C \otimes BA) \mathbf{h} \\ &= \text{vec}(C \text{unvec}(\mathbf{h})(BA)^\top) \\ &= \text{vec}(C((BA \text{unvec}^\top(\mathbf{h}))^\top)^\top).\end{aligned}\tag{21}$$

Here, vec represents the row-major vectorization operator that stacks the rows of a matrix into a vector, and unvec reshapes the vector \mathbf{h} from $\mathbf{h} \in \mathbb{R}^q$ to $\text{unvec}(\mathbf{h}) \in \mathbb{R}^{u_q \times v_q}$ by filling rows of $\text{unvec}(\mathbf{h})$ with consecutive elements from \mathbf{h} . The unvec^\top notation indicates an additional transpose operation following $\text{unvec}(\mathbf{h})$. As illustrated in [Figure 4](#), this representation enables us to interpret LoKr as a composition of three consecutive linear layers. In [Algorithm 1](#), we further provide a PyTorch-style pseudo-code that implements the decomposition of [\(21\)](#).

C Challenges in Algorithm Evaluation

In this appendix, we highlight a number of difficulties in evaluating the performance of fine-tuning algorithms. These complexities caution against simplistic comparisons and underscore the importance of a more comprehensive evaluation framework, as what we proposed in [Section 4](#).

Sensitivity to Hyperparameters. As we can see from [Figure 2](#), the algorithms' performance are sensitive to various hyperparameters, such as learning rate, dimension, and factor. Without a single objective metric, pinpointing the optimal hyperparameters for a specific method becomes elusive. As a result, comparing two methods based on a single set of hyperparameters oversimplifies the evaluation process.

Performance Discrepancy Across Concepts. The models' performances can differ substantially across different concepts, whether these are trained in isolation or in tandem. This variance is especially pronounced when comparing concepts that are fundamentally different or with differing numbers of training images. Nonetheless, even when these factors are mitigated, discrepancies in performance across concepts can still arise, as illustrated in [Appendix G.1](#).

Influence of Dataset. In a similar vein, the composition of the dataset, including the images and accompanying captions, exerts a significant influence on the performance of the fine-tuning model (see [Appendix H.3](#) for an illustration on the importance of having good captions). Additionally, the nuances of each dataset may necessitate tailored approaches or specific configurations to achieve optimal results. For instance, a larger training set or a dataset featuring concepts that diverge substantially from the model's pretrained knowledge may benefit from employing a model with

greater capacity. Thus, it is essential to adapt fine-tuning strategies to the particularities of the dataset at hand.

Conflicting Criteria. There is an intrinsic trade-off between the various criteria under consideration. We have particularly seen in [Section 5.3](#) that models with higher concept fidelity often have lower controllability, diversity, and base model preservation. Determining the optimal balance among these criteria requires a nuanced, case-by-case analysis rather than a simple aggregation of metrics.

Unreliability of Evaluation Metrics. Despite the significant advancements in computer vision and deep learning in recent years, the metrics we employ are still far from perfect. Often, these metrics do not fully align with human judgement and may overlook nuanced details that define a concept, as shown by [Thrush et al. \(2022\)](#); [Yuksekgonul et al. \(2023\)](#) and we further elaborate in [Appendix G.2](#). Additionally, a single numerical value can be insufficiently informative; for instance, a low image similarity score could arise from either underfitting or overfitting.

Practical Considerations. In practice, a trained model often undergoes further adjustments. As explained in [Section 3.1](#), we can adjust the scaling factor of the fine-tuned weight differences ΔW , combine multiple trained networks, and apply the fine-tuned parameters to a different base model. This is not to mention the influence of prompts and the potential for prompt engineering. All these variables add layers of complexity to the evaluations.

In light of the aforementioned complexities, it becomes evident that assessing the effectiveness of fine-tuning algorithms is a multifaceted challenge. While existing research often leans on a limited scope of evaluation metrics, hyperparameters, and concept categories, such an approach risks not capturing the full breadth and depth of these algorithms’ capabilities and inadvertently results in evaluations that unfairly penalize certain methods. Therefore, we call upon the research community to build upon our initial efforts by investing in the development of more extensive evaluation frameworks and ecosystems for fine-tuned text-to-image models. These should aim to delve deeper into the subtleties of various fine-tuning strategies, thereby promoting more robust and meaningful comparisons.

D Experimental Details

This part of the appendix offers detailed information about the experiments we conducted, ranging from dataset specifics, algorithm settings, to details on the evaluation of the models.

D.1 Dataset

In this section, we provide more details on the composition of our dataset, the sources of the data, and the captioning strategy.

Dataset Structure. Our dataset follows a hierarchical structure, as detailed in [Tables 2](#) and [3](#). We also include the count of images for each category, class, and subclass, as well as the number of repeats for images in each class (used for dataset balancing) in these tables.

Data Sources. The images in our dataset originate from various sources to encompass a broad range of styles and subjects.

- Images for anime characters are sourced from the DAF:re dataset ([Rios et al., 2021](#)).
- Movie character images are extracted from a public dataset available on Kaggle ([Young, 2019](#)).
- Scene and stuffed toy images are part of the CustomConcept101 dataset ([Kumari et al., 2023](#)).
- Style-related images are compiled from multiple sources, including the “new” WikiArt dataset ([Tan et al., 2019](#)), the Old Book Illustrations dataset ([gigant, 2007](#)), and Studio Ghibli’s official website⁶. For the images obtained from Studio Ghibli’s website, it is important to note that Studio Ghibli specifies they should be used “with common sense” and are not intended for commercial use.⁷

⁶<https://www.ghibli.jp/works/> (Accessed: 2023-07-16)

⁷Studio Ghibli’s original note in Japanese: ※画像は常識の範囲でご自由にお使いください。

Category	Class	Sub-class	# of Images	Repeat
Anime Characters (571 images)	Yuuki Makoto	N/A	90	2
	Kotomine Kirei		51	4
	Tushima Yoshiko		128	2
	Ika Musume	Default outfit	118	
		Alternative outfit	20	1
		Others	34	
	Abukuma (KanColle)	Dark color uniform	54	
		Light color uniform	48	2
		Others	28	
Movie Characters (276 images)	K-2SO	N/A	63	3
	Admiral Piett	Figurine	13	
		Realistic	34	4
		Others	2	
	Bodhi Rook	Figurine	11	
		Illustration	12	
		Realistic	34	3
		Others	2	
	Saw Gerrera	Afro, illustration	4	
		Afro, realistic	23	
		Bald, 3d	10	4
		Bald, realistic	7	
		Others	1	
Styles (776 images)	Rose Tico	Illustration	10	
		Realistic	45	3
		Others	5	
		Ghibli	200	1
		Ghibli 2	100	2
		Old Book	100	2
		Ukiyo E	87	2
	Impressionism	N/A	101	2
	Felix Vallotton		100	2
	Vladimir Borovikovsky		88	2

Table 2: Summary of dataset composition—anime characters, movie characters, and styles.

Category	Class	Subclass	# of Images	Repeat
Stuffed Toys (53 images)	Tortoise	N/A	12	17
	Pink		10	20
	Panda		10	20
	Bunny		7	29
	Lobster		7	29
	Teddy Bear		7	29
Scenes (30 images)	Waterfall	N/A	9	22
	Garden		7	29
	Canal		5	40
	Castle		5	40
	Sculpture		4	50

Table 3: Summary of dataset composition—stuffed toys and scenes.

Captioning. For captioning of our dataset, we employ a tagger with a ConvNeXt V2 architecture (Woo et al., 2023), hosted on Hugging Face.⁸ This tagger is trained on the Danbooru dataset (Anonymous et al., 2022). We set the threshold to 0.35 for our use. After the initial tagging phase, we manually adjust the tags for all the images within the categories “scenes” and “stuffed toys”. As for images of other categories, we filter out tags that are naturally bound to the target concept, such as tags that represent hair color or gender. We also remove tags that are related to the corresponding outfit for character outfit sub-classes.

Regarding class words and trigger words, we use unique tokens for each class and outfit sub-class, leading to a total of 32 different tokens. The class word is set to one of the following: anime girl, anime boy, robot, man, woman, scene, stuffed toy, or style. Sub-class keywords are used as is for movie characters and otherwise formed by concatenating the relevant token with the word “outfit” for the two anime characters in question. We do not use sub-class keywords for the sub-class “others”. The final prompt consists of a string where the concept descriptor, sub-class keyword, and tags are separated by commas. For illustration, an example is provided below:

```
"[Vabukuma] anime girl, [Vdark uniform] outfit, looking at viewer,  
smile, simple background, full body, boots, black background"
```

A Note on Prior-Preservation Loss. The prior-preservation loss is frequently used in the literature to enhance the model’s performance for generalization and concept-agnostic prompts, see e.g., Han et al. (2023); Kumari et al. (2023); Ruiz et al. (2023). Specifically, this approach has proven effective in mitigating unwanted concept drift and enriching the diversity of the generated images. Despite these merits, we have opted not to incorporate the prior-preservation loss in our experiments for two important reasons.

First, implementing this loss function necessitates the creation of a separate regularization dataset. This can be a labor-intensive process, particularly in our case where the training set encompasses a broad range of concept categories. While one could always build a regularization set using the pretrained model, there remains the challenge of designing the prompts for generation and ensuring the diversity and quality of the generated samples. Furthermore, some users would prefer the fine-tuned model to produce samples distinct from those produced by the pretrained model.

Secondly, it is our hope that by focusing on this more challenging setup, we can better identify the impacts of various algorithmic configurations and settings. In fact, with the prior-preservation loss

⁸<https://huggingface.co/SmilingWolf/wd-v1-4-convnext-tagger-v2> (Accessed: April 22, 2023)

the model learns from both the training set and the regularization set, making the analysis of the methods even more complicated.

D.2 Algorithm Configuration and Hardware

This section details the configurations employed for training and image generation, as well as the hardware specifications utilized in our experiments.

Shared Hyperparameters. The following hyperparameters are used throughout our experiments.

- **Optimizer:** We use 8-bit AdamW (Dettmers et al., 2022; Loshchilov & Hutter, 2019) with weight decay 0.1, $\beta_1 = 0.9$, $\beta_2 = 0.99$, and a constant scheduler with 5 epochs of warm-up. Gradient clipping is also applied, with a maximum gradient norm set to 1.
- **Data:** We load the data using aspect ratio bucketing with resolution set to 512. This ensures that each image is resized to maintain its original aspect ratio as much as possible, while the new height and width must be multiples of 64, and the new area must not exceed 512×512 . Batch size is set at 8, and a caption-dropping rate of 5% is applied, meaning that empty captions are used in the loss calculation with a 5% probability.
- **Image generation:** We use 25 steps of DDIM sampler (Song et al., 2021) with a CFG scale of 7. All the generated images are of size 512×512 . No negative prompt is used.

Configuration-Dependent Hyperparameters. By default, we train all the linear layers of the text encoder and U-Net, with a learning rate of 10^{-6} for native fine-tuning, and a learning rate of $5 \cdot 10^{-4}$ for LoRA, LoHa and LoKr. The default dimension and alpha for LoRA and LoHa are respectively (8, 4) and (4, 2). The default factor for LoKr is 8. Note that as explained in Section 3.2, it is also possible to specify dimension for LoKr in LyCORIS, and this leads to a low rank decomposition of the second block obtained from the Kronecker product decomposition. To avoid this behavior, we need to set the dimension to a sufficiently large number. The hyperparameters for the remaining experiments where we individually vary 1 to 2 hyperparameters are as specified in Section 5.3.2. The same set of hyperparameters is applied to all the trained layers of the network. The resulting file sizes for each network configuration are provided in Table 4.

Hardware and Library. We conduct all experiments on a Ubuntu Server equipped with four A6000 GPUs. For the training script, we re-use the public sourced code from *kohaya-ss/sd-scripts*⁹, version 0.6.5. After fine-tuning, we generate the images through the API provided by *stable-diffusion-webui*¹⁰. Note that support for LyCORIS has been integrated as the default feature of *stable-diffusion-webui* during paper writing. The versions of *stable-diffusion-webui* and LyCORIS are respectively 1.6.0 and 1.9.0.dev9. We adopt the Python 3.10 interpreter with Pytorch 2.0 (Paszke et al., 2019). Moreover, we employ transformers 4.26 (Wolf et al., 2020), diffusers 0.10.2 (von Platen et al., 2022), and accelerate 0.15 (Gugger et al., 2022) for our experiment.

D.3 Evaluation Prompts

We provide below the complete list of the generalization prompts used in the generation of our evaluation images. These prompts are formulated using natural language syntax, in contrast to the tag-based structure used for training captions.

<Alter> Generalization Prompts with Content Alteration. The prompts of this type are organized into 8 templates as shown in Table 5. Each template contains 10 prompts, and multiple (sub-)classes use the same template. Many of these prompts are directly taken from the CustomConcept101 dataset.

<Style> Generalization Prompts with Style Alteration. For generalization prompts with style alteration, we use a set of 5 prompts that are shared across all the classes, as listed below.

- {} in the style of pencil drawing

⁹<https://github.com/kohaya-ss/sd-scripts>

¹⁰<https://github.com/AUTOMATIC1111/stable-diffusion-webui>

Algorithm	Trained Layers	Dimension	Factor	File Size
LoRA	Attention	8	N/A	4.4 M
	Linear	8		9.2 M
	Full	8		20 M
	Linear	32		37 M
LoHa	Attention	4	N/A	4.4 M
	Linear	4		9.3 M
	Full	4		20 M
	Linear	16		37 M
LoKr	Linear	N/A	12	6.4 M
	Attention		8	3.8 M
	Linear	8	8	11 M
	Full	N/A	8	29 M
	Linear		4	43 M
Native Fine-Tuning	Attention	N/A	N/A	233 M
	Linear			672 M
	Full			1.8 G

Table 4: Resulting file size from different algorithm configuration (saved in fp16 format). Note that among the hyperparameters that we consider, only trained layers, dimension, and factor have an impact on the file size.

- {} in the style of watercolor painting
- {} in the style of Vincent Van Gogh
- {} in the style of Claude Monet
- {} in the style of pixel art

Note that we do not generate images using <style> prompts for classes that fall under the “styles” category and we do not generate images for sub-classes “others” that fall under the “movie characters” category. This results in a total of 14,900 generated images per checkpoint, as mentioned in [Section 5.2](#).

D.4 Evaluation Metrics

The metrics we examine are built upon two fundamental elements: a lower-dimensional representation space and simple, analytically defined functions operating within that space. We use an encoder to project images into this representation space, which is intended to capture perceptual relevance that is broadly applicable to a wide array of images. Following this transformation, we compute the analytically defined functions within this embedding space. In this way, the functions and the encoders can be discussed separately, and in this section, our primary focus is on these functions, assuming that the features for both images and text are readily given.

Image Similarity. Given two sets of images with their corresponding features $\mathcal{Z}^1 = \{z_i^1\}_{i=1}^n$ and $\mathcal{Z}^2 = \{z_i^2\}_{i=1}^m$, the average cosine similarity between the two sets is computed as

$$S_C(\mathcal{Z}^1, \mathcal{Z}^2) = \frac{1}{nm} \sum_{i=1}^n \sum_{j=1}^m \frac{\langle z_i^1, z_j^2 \rangle}{\|z_i^1\| \|z_j^2\|} = \frac{1}{nm} \sum_{i=1}^n \sum_{j=1}^m \langle \hat{z}_i^1, \hat{z}_j^2 \rangle, \quad (22)$$

where for a vector z we define $\hat{z} = z/\|z\|$ as its normalized vector. We also define

$$\bar{z}^1 = \frac{1}{n} \sum_{i=1}^n \hat{z}_i^1 \quad \text{and} \quad \bar{z}^2 = \frac{1}{m} \sum_{i=1}^m \hat{z}_i^2.$$

For Anime and Movie Characters	For Stuffed Toys
{ } selfie standing under the pink blossoms of a cherry tree { } in a chef's outfit, cooking in a kitchen { } paddling a canoe on a tranquil lake { } playing with their pet dog { } in an astronaut suit, floating in a spaceship { } dressed in a firefighter's outfit, a raging forest fire in the background { } wearing Victorian-era clothing, reading a book in a classic British library { } dressed as a knight, riding a horse in a medieval castle { } kneeling under trees with aurora in the background { } wearing red dress jumping in the sky in a rainy day	{ } in grand canyon { } swimming in a pool { } sitting at the beach with a view of the sea { } in times square { } in front of a medieval castle { } wearing sunglasses { } working on the laptop { } on a boat in the sea { } wearing headphones { } lying in the middle of the road
For Styles	For Waterfall
{ } of a city skyline during sunset { } of a bustling marketplace in the 1800s { } of a lone tree standing in a vast desert { } of children flying kites on a breezy day { } of a roaring lion in the heart of the jungle { } of a mountain climber scaling a snowy peak { } of a dancer lost in the rhythm of music { } of a quaint countryside cottage surrounded by wildflowers { } of a serene monk meditating atop a hill { } of a vintage car speeding along a coastal road	{ } at dusk with the first rays of sunlight creeping in { } at night full of stars A frozen { } in the winter season and snow all around { } in a neon-lit cyberpunk cityscape A golden retriever in front of the { } A cat sitting in front of the { } { } with a vibrant rainbow arching across its mist { } in a fantasy world, with dragons flying around A painter painting the scene of the { } on canvas { } of molten lava flowing down
For Canal	For Garden
{ } surrounded by towering skyscrapers { } against a backdrop of snow-capped mountains { } under a star-filled night sky { } in the autumn season with colorful foliage { } with a hot air balloon drifting all over the sky { } with a cobblestone bridge arching over the water { } with a rustic wooden boat gently floating in the water { } with a swan gliding gracefully in the water { } with the water turned into liquid gold, reflecting the setting sun { } with the water replaced by a smooth pathway of glowing emeralds	{ } with an active volcano in the background { } with night sky { } with cloudy sky { } with stone pillars and intricate carvings on it A British shorthair cat sitting in front of { } A koala eating leaves in { } A red cardinal flying in { } A rustic wooden swing in { } A laughing Buddha statue in { } { } with yellow marigold flowers
For Castle	For Sculpture
{ } stands against a backdrop of snow-capped mountains { } surrounded by a lush, vibrant forest { } in the autumn season with colorful foliage { } on a rocky cliff, with crashing waves below { } surrounded by a field of grazing sheep { } overlooks a serene lake { } overlooks a serene lake, where a family of geese swims { } guarded by mythical elves A peacock in front of the { } { }, made of crystal, shimmers in the sunlight	{ } at a beach with a view of the seashore { } in the middle of a highway road { } in Times Square { } on the surface of the moon A puppy in front of { } with a close-up view A cat sitting in front of { } in the snow A squirrel in front of { } { } in snowy ice { } made of metal { } digital painting 3D render in geometric style

Table 5: Evaluation prompts of type <alter> for image generation. { }'s are to be filled with concept descriptors.

These are the centroids of the normalized vectors. The centroid distance that we consider in our experiments is given by

$$\text{dist}_{\text{cent}}(\hat{\mathcal{Z}}^1, \hat{\mathcal{Z}}^2) = \|\bar{z}^1 - \bar{z}^2\|.$$

In the above, we write $\hat{\mathcal{Z}}^1$ and $\hat{\mathcal{Z}}^2$ for the sets of normalized vectors. It is worth noticing that with $\text{Var}(\mathcal{Z})$ denoting the variance of set \mathcal{Z} , it holds that

$$1 - S_C(\mathcal{Z}^1, \mathcal{Z}^2) = \frac{1}{2} \left(\|\bar{z}^1 - \bar{z}^2\|^2 + \text{Var}(\hat{\mathcal{Z}}^1) + \text{Var}(\hat{\mathcal{Z}}^2) \right). \quad (23)$$

The above formula reveals that average cosine similarity inherently rewards image sets with lower diversity, as mentioned in [Section 5.3.2](#). This insight compels us to consider squared centroid distance as a complementary measure. Specifically, we utilize squared centroid distance when contrasting results against the Vendi scores of the images to remove the aforementioned bias.

Text-Image Alignment. Let $\mathcal{Z}^{\text{image}} = \{z_i^{\text{image}}\}_{i=1}^n$ be the features of a set of images and $\mathcal{Z}^{\text{text}} = \{z_i^{\text{text}}\}_{i=1}^n$ be the features of their corresponding prompts. To evaluate text-image alignment, we compute the cosine similarity between an image and its corresponding prompt and average the results.

This gives

$$S'_C(\mathcal{Z}^{\text{image}}, \mathcal{Z}^{\text{text}}) = \frac{1}{n} \sum_{i=1}^n \frac{\langle z_i^{\text{image}}, z_i^{\text{text}} \rangle}{\|z_i^{\text{image}}\| \|z_i^{\text{text}}\|}.$$

Moreover, in our experiments, we process the prompts as following before feature encoding:

- For anime and movie characters, we remove trigger words and retain class words.
- For scenes and stuffed toys, we replace trigger words with the corresponding class names, as given in [Table 3](#).
- For styles and outfit sub-classes, we remove both trigger words and class words. Any extra commas or prepositions that remain are also removed.

Diversity. We employ the Vendi score, as proposed by [Friedman & Dieng \(2023\)](#), to assess the diversity within a set of images. Given the images’ features $\mathcal{Z} = \{z_i\}_{i=1}^n$, the definition of the Vendi score relies on the eigenvalues $\lambda_1, \dots, \lambda_n$ of a matrix K/n , where K is a kernel matrix constructed using a positive semi-definite kernel function k . More precisely, the entries of K are calculated as $K_{ij} = k(z_i, z_j)$. In this work, we specifically employ a linear kernel between normalized vectors to compute the entries of the kernel matrix, i.e.,

$$k(z, z') = \frac{\langle z, z' \rangle}{\|z\| \|z'\|}.$$

With these in mind and using the convention $0 \log 0 = 0$, the Vendi score of the feature set is given by

$$\text{VS}(\mathcal{Z}) = e^{-\sum_{i=1}^n \lambda_i \log \lambda_i}.$$

The Vendi score can be interpreted as the “effective number of modes” within the feature set. In particular, it is more sensitive to changes in the number of modes compared to the intra-dissimilarity. See also [Stein et al. \(2023\)](#) and our experiments in [Appendix H.1](#) for further support for the use of the Vendi score.

Style Loss. Unlike the metrics described above, the style loss introduced by [Johnson et al. \(2016\)](#), is intrinsically associated with a specific encoder: the VGG network ([Simonyan & Zisserman, 2015](#)). For its computation, we use feature maps from several convolutional layers to extract information. In particular, we select the layers `conv1_1`, `conv2_1`, `conv3_1`, `conv4_1`, and `conv5_1` from a pretrained VGG-19 network in our experiments.¹¹ Each of these layers provides an output with a shape of $c_i \times h_i \times w_i$, where i identifies the particular layer (ranging from 1 to 5 in our setup), and c_i , h_i , w_i represent respectively the number of channels, the height, and the width of the feature maps. These outputs are further reshaped to matrices $\psi_i(x)$ of shape $c_i \times h_i w_i$, where x represents the image in input. Following the reshaping, we calculate the corresponding normalized Gram matrices

$$G_i(x) = \frac{1}{c_i h_i w_i} \psi(x) \psi(x)^\top.$$

Finally, to obtain the style loss, we compute the squared Frobenius norm of the differences between the Gram matrices of the two images. This is done for each selected layer, and the results are summed, leading to

$$\mathcal{L}_{\text{style}}(x, x') = \sum_{i=1}^5 \|G_i(x) - G_i(x')\|^2.$$

Importantly, as the VGG network can take images of any resolution in input (as long as the short edge has at least 224 pixels) and the size of the gram matrices does not depend on the size of the input images, we can compute the style loss between two images of different resolutions. In our evaluation of base model preservation, we compute the style losses between pairs of images generated from identical prompts and seeds but differing in whether the model is fine-tuned or not. We then average these individual style losses to arrive at a single metric for each (sub-)class.

¹¹<https://pytorch.org/vision/main/models/generated/torchvision.models.vgg19.html>
(Accessed: 2023-08-16)

D.5 Encoders

For the computation of image similarity and Vendi score, we consider three different encoders: DINOv2 (Oquab et al., 2023), CLIP (Radford et al., 2021), and ConvNeXt V2 (Woo et al., 2023). This choice is motivated by Stein et al. (2023), where the authors compared a number of encoders and concluded that DINOv2, CLIP ViT-L/14, and MAE (He et al., 2022) are much better at extracting high-level representations that align with human perception. In particular, they showed that the Fréchet distance (Dowson & Landau, 1982; Heusel et al., 2017) measured in the representation space of these networks are more correlated with human error rate in distinguishing real from fake images, compared to other networks they examined. Although ConvNeXt V2 was not considered by Stein et al. (2023), we include it in the correlation analysis of Appendix E for it being itself an improvement over MAE. We use models of size “L” throughout our work.

As for the main experiments, we opt for DINOv2 as our encoder for evaluating image similarity and Vendi scores following the recommendation of Stein et al. (2023). To accommodate DINOv2’s input resolution, all the images are padded (in cases where the image is non-square) and resized to dimensions of 224×224 .¹² On the other hand, among the aforementioned encoders, CLIP is the only one that can be used to evaluate text-image alignment. More details on the used pretrained networks are provided below.

- DINOv2: We use the original pretrained DINOv2 ViT-L/14 model available via PyTorch Hub.¹³
- CLIP: Following Stein et al. (2023), we use the OpenCLIP ViT-L/14 implementation (Ilharco et al., 2021) trained on DataComp-1B (Gadre et al., 2023), which is reported to be the best CLIP ViT-L/14 model in the OpenClip library. We use the image features that are obtained after the final projection layer.
- ConvNeXt V2: We load the pretrained convnextv2_large.fcmae_ft_in22k_in1k_384 checkpoint using the timm toolkit (Wightman, 2019). The pre_logits features are used.

D.6 Metric Value Processing

In this section, we discuss in detail how the resulting metric values are processed and analyzed.

Normalization and Aggregation. To account for the varying ranges of metric values across different classes and sub-classes, we employ a rank-based normalization technique. Specifically, for each metric value (e.g., average cosine similarity between dataset and generated images, Vendi score) computed for a given class or subclass and a specific type of prompt, we rank it against other metric values computed with the same metric, for the same class or sub-class and prompt type, but for different checkpoints. This allows us to assign a normalized score to each metric value, with the highest-ranking score set to 1 and the lowest set to 0. These normalized scores are equally distributed between 0 and 1. This rank-based normalization is motivated by our focus on relative performance and enables more equitable comparisons across varying classes.

Building upon the above, we then first average the normalized scores across sub-classes of the same class and then average across different classes within the same category. For the scatter plots, we also average these scores across random seeds, and the error bars indicate the standard error of these scores across both random seeds and classes.

SHAP Analysis. The SHAP analysis is performed on the average normalized scores for each category. As shown in Figure 2, we consider 5 dependent variables: algorithm, trained layers, epoch, capacity, and learning rate level. Among these, algorithm and trained layers are treated as categorical features, while the remaining ones are treated as numerical features. The learning rate level is set to either 1, 2, or 3, corresponding to the smallest, intermediate, and largest learning rates considered for each algorithm. As for the capacity variable, we assign a value of 1 for default hyperparameters and 2 for configurations with altered dimensions and factors in LoRA, LoHa, and

¹²The impact of the resizing method is also investigated in Appendices E and H.1

¹³<https://github.com/facebookresearch/dinov2> (Accessed: 2023-08-14)

LoKr. However, LoRA and LoHa configurations with higher dimensions and an alpha of 1, along with LoKr configurations with a factor of 12, are excluded from the SHAP analysis. It is also important to note that the capacity variable is not meaningful for native fine-tuning. To accommodate this, we designate a capacity value of 3 for all native fine-tuning configurations, and subsequently adjust the SHAP value for the algorithm variable by adding up the SHAP value from the capacity variable for these configurations.

Due to the presence of categorical feature, we used CatBoostRegressor for the analysis.¹⁴ We set iterations to 300 and the learning rate to 0.1 while leaving the remaining hyperparameters untouched.

E Correlation Analysis

In our study, we are faced with a plethora of metrics that could be considered for evaluating the models. Moreover, the precise definitions and computation of these metrics can vary depending on factors like the encoder used or the resizing methods applied. Given this complexity, we are interested in the following two main questions: how do these variables affect the results, and what relationships exist between different metrics? To answer these, we go beyond the metrics studied in [Section 5.3](#) and present a comprehensive correlation analysis in this appendix.

Resizing Methods. Given a target resolution s , we consider four different methods for resizing a rectangular image.

- **Scale:** The image is resized such that the smaller edge matches the target resolution while preserving the original aspect ratio.
- **Letterbox:** This method adds black-colored padding around the original image to fit it within the target resolution, preserving the aspect ratio of the original image.
- **Center Crop:** After scaling the image, the central part fitting within the target resolution is retained, and the outer portions are cropped away.
- **Stretch:** The original image is stretched or compressed to fit the target resolution, potentially causing distortion as the aspect ratio is not preserved.

It is important to note that while the last three methods produce images with dimensions of $s \times s$, the “scale” method maintains the original aspect ratio. Therefore, “scale” is only applicable when the encoder can accept rectangular images. For this reason, in our experiments, we use the “scale” method exclusively for ConvNeXt V2 and Vgg19 (the latter is used in the computation of style loss). The “stretch” method is applied for DINOv2 and CLIP. Both “letterbox” and “center crop” (abbreviated as “crop” in the figures) are tested across DINOv2, CLIP, and ConvNeXt V2.

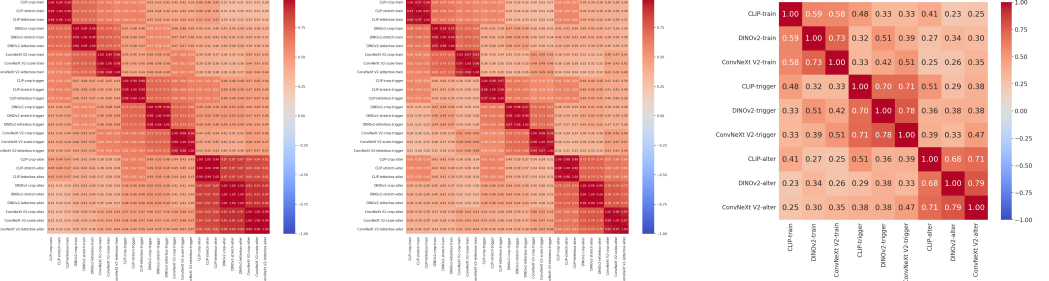
Implementation Details. We compute the Pearson correlation coefficients of the normalized scores. We do not perform aggregation across classes or sub-classes before the computation.

E.1 Influence of Encoders, Resizing Methods, and Prompt Types

We first investigate the influence of the choice of encoder and resizing method. To this end, we compute two types of image similarity (based on either average cosine similarity or squared centroid distance as discussed in [Appendix D.4](#)) and the Vendi score using different encoders and resizing methods. Note however that as our generated images are all squares, the difference in resizing methods only matters when dataset images are also included in the computation in the metrics (which is not the case for Vendi score). Moreover, for the computation of Vendi score on images generated from the prompts of type <alter>, we first compute the Vendi score for each unique prompt before averaging them to form a single score for each class or sub-class.

The results of the correlation analysis are presented in [Figure 5](#). Generally speaking, we can see that that the choice of resizing method has little influence on the outcomes, with correlation coefficients

¹⁴https://catboost.ai/en/docs/concepts/python-reference_catboostregressor (Accessed: 2023-08-25)



(a) Correlation matrix heatmap for image similarity. **(b)** Correlation matrix heatmap for image similarity based on squared centroid distance. **(c)** Correlation matrix heatmap for Vendi score.

Figure 5: Pearson correlation for metrics computed using different encoders and resizing methods, evaluated on images generated from different types of prompts (best viewed when zoomed in).

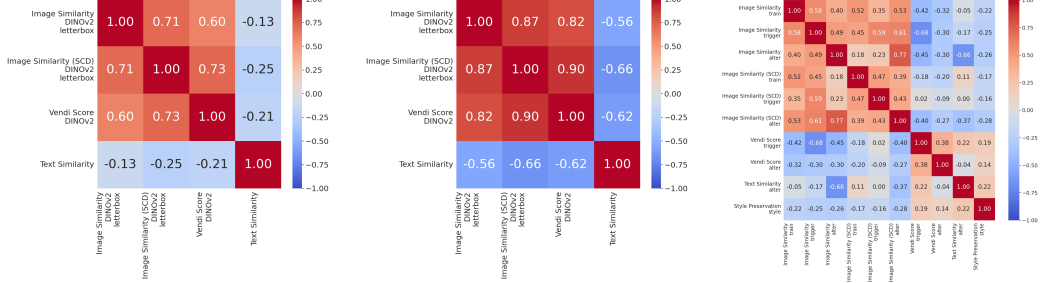
ranging between 0.95 and 1. While the choice of encoder has a greater influence, the resulting metrics still exhibit strong positive correlations (typically between 0.65 and 0.9). In particular, we observe a higher correlation between image similarity metrics calculated with different encoders when images are generated using generalization prompts, as opposed to using training prompts or prompts containing only the concept descriptor. We believe that this occurs because the image similarity score in the former cases is primarily influenced by how closely the generated images adhere to either the prompts or the dataset images. This overarching trend can be readily discerned regardless of the encoder used. Conversely, for training prompts and simple captions containing only the concept descriptor, a more nuanced analysis is required to gauge image similarity, making the choice of encoder more critical.

Finally, we observe a lower positive correlation (often below 0.5) between metrics evaluated on images generated from different prompt types. This suggests that model rankings could vary considerably depending on the types of prompts under consideration, highlighting again the importance of evaluating images generated by each type of prompt individually. Interestingly, utilizing the CLIP encoder tends to yield the highest correlations across images generated using different prompt types.

E.2 Relation between Different Metrics

We next examine how the various types of metrics under consideration relate to each other. The results are shown in [Figure 6](#). Since our primary focus here is on the metrics used in [Section 5.3](#), we employ DINOv2 as the encoder for the computation of image similarity and Vendi score, and we use letterbox resizing to resize dataset images to the target resolution when computing image similarity.

As we can see from Figures 6a and 6b, text and image similarity metrics exhibit a strong negative correlation when generalization prompts are used to generate images. However, this correlation weakens considerably when training prompts are utilized. This suggests again that the trade-off between producing images that look similar to those in the training set and producing images that follow the prompts is much easier to be evaluated by the considered metrics. Finally, we make two observations in Figure 6c. First, the correlation between Vendi score, text similarity, and base model style preservation (as measured by the style loss) is relatively weak, even though they are all negatively correlated with image similarity. This underscores the fact that these metrics serve as distinct indicators of model performance and should be independently evaluated. Secondly, we observe that the correlation between Vendi score and image similarity weakens when the latter is assessed using squared centroid distance. This observation is consistent with our prior discussion in Appendix D.4 and validates our decision to contrast diversity against image similarity as measured by squared centroid distance in Figure 2.



(a) Correlation matrix heatmap for image and text similarity metrics on <train> prompts.
(b) Correlation matrix heatmap for image and text similarity metrics on <alter> prompts.
(c) Correlation matrix heatmap for the main metrics studied in this work.

Figure 6: Pearson correlation for the main metrics studied in this work (best viewed when zoomed in). SCD stands for squared centroid distance.

F Supporting Plots

To substantiate the claims made in [Section 5.3](#), we include in this section a comprehensive set of plots for the key metrics under review. This set comprises both the beeswarm plots showcasing the SHAP values and the scatter plots contrasting various metrics. Among these, we have made the decision to omit the scatter plots for the epoch 30 checkpoints, as we believe that the plots for epochs 10 and 50 are sufficient to demonstrate the sensitivity of the results to the number of training epochs. As in [Section 5.3](#), these plots are organized according to concept categories.

It is important to acknowledge that some discrepancies do arise when comparing these plots to the principles laid out in [Section 5.3](#). Upon closer examination, we categorize these discrepancies into two groups. First, there are genuine deviations, which indicate that the models behave in ways not entirely captured by our initial guidelines. Second, there are metric-induced deviations, which arise from the limitations or biases in the metrics themselves. As we explore the plots by category in the remainder of this section, we will briefly touch upon some of these discrepancies. Further elaboration on the genuine deviations, supported by qualitative examples, are presented in [Appendix G.4](#).

F.1 Plots for Category “Movie Characters”

The plots for the “movie characters” category are shown in Figures 7 to 9. These results largely align with our general guidelines. Specifically, we observe that for generalization prompts with content alteration, LoKr exhibits high image similarity and low text similarity at lower epochs, while LoRA achieves similar result at higher training epochs.



Figure 7: SHAP beeswarm charts for the category “Movie Characters” showing the impact of diverse algorithm factors on the evaluation metrics. LoRA is in blue, LoHa is in purple, LoKr is in purple red, and native fine-tuning is in red.

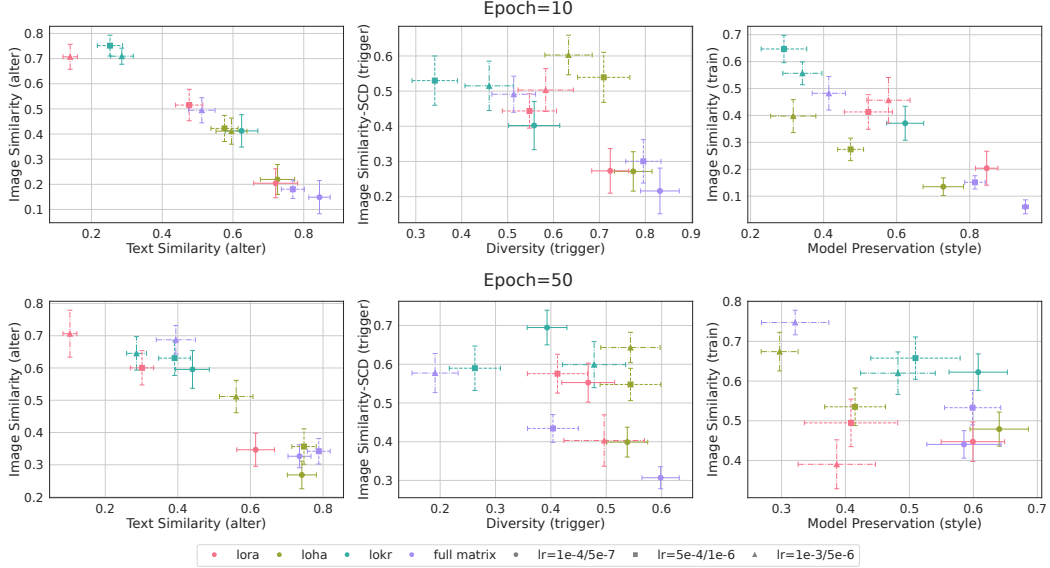


Figure 8: Scatter plots comparing different evaluation metrics for the category “Movie Characters”, with variations across algorithms and learning rates. As in Section 5.3, in the middle column we use squared centroid distance (SCD) to measure image similarity.

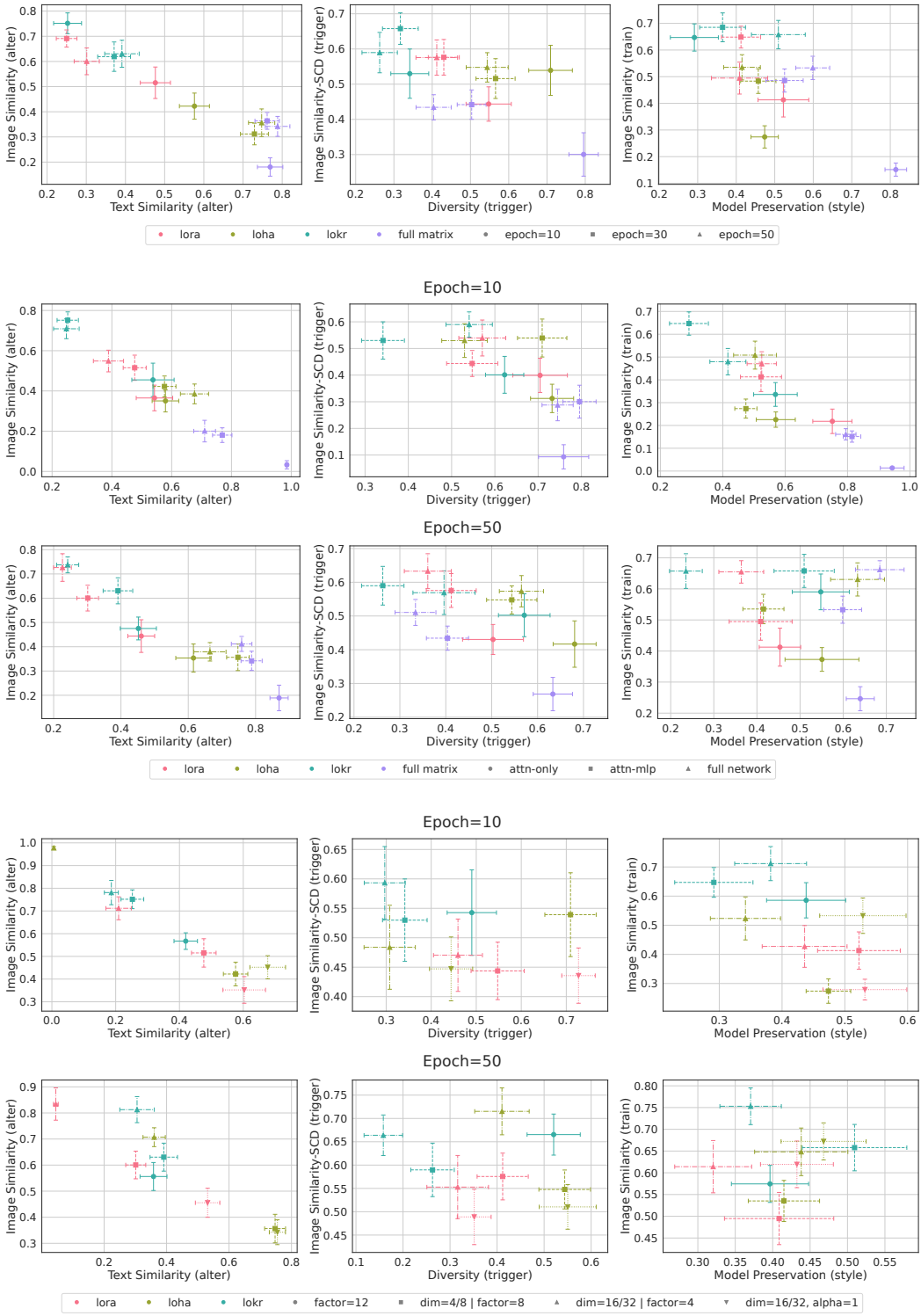


Figure 9: Scatter plots comparing different evaluation metrics for the category "Movie Characters", with variations across algorithms and either i) top: number of training epochs, ii) middle: trained layers, or iii) bottom: dimensions, factors, and alphas.

F.2 Plots for Category “Scenes”

The plots for the “scenes” category are shown in Figures 10 to 12. As both the checkpoints after 30 and 50 epochs are severely overtrained for this category, we only consider the epoch 10 checkpoints when performing SHAP analysis. Again, the results mostly agree with the claims made in Section 5.3, though the difference between LoRA and LoHa are less pronounced here. We do however note that LoRA now has the best base model style preservation among all the algorithms. The qualitative comparison in Appendix G.4.1 further validates this observation.

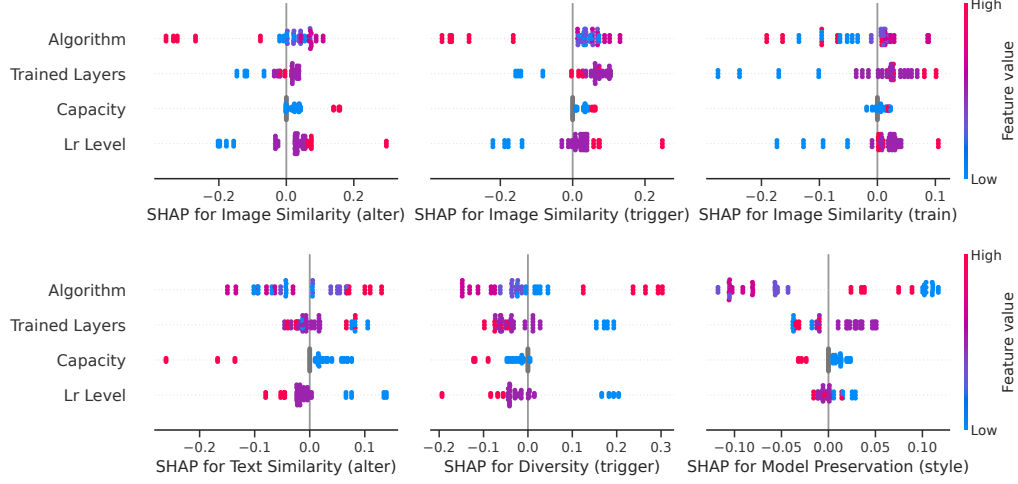


Figure 10: SHAP beeswarm charts for the category “Scenes” showing the impact of diverse algorithm factors on the evaluation metrics. LoRA is in blue, LoHa is in purple, LoKr is in purple red, and native fine-tuning is in red.

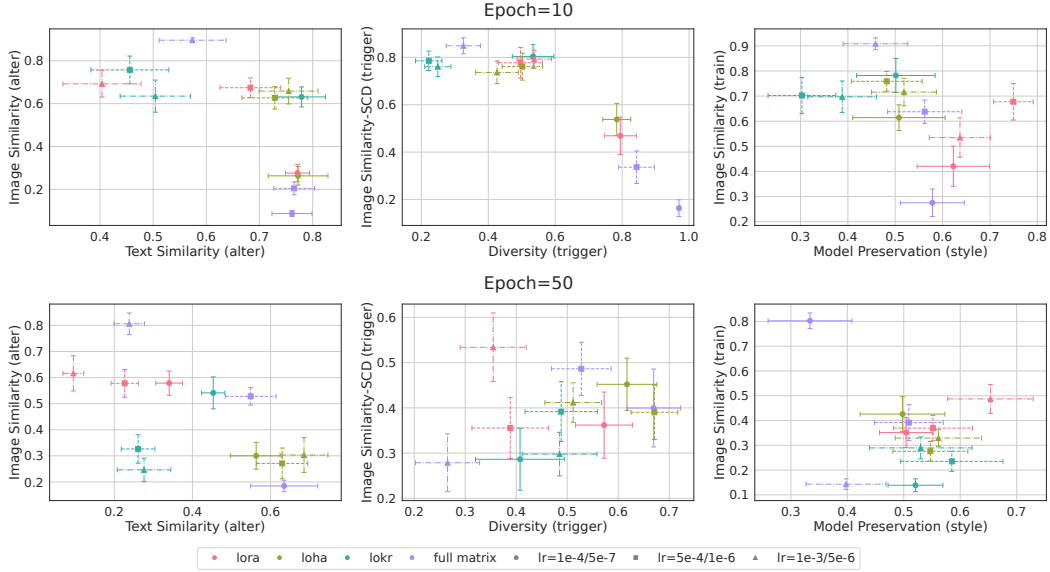


Figure 11: Scatter plots comparing different evaluation metrics for the category “Scenes”, with variations across algorithms and learning rates. As in Section 5.3, in the middle column we use squared centroid distance (SCD) to measure image similarity.

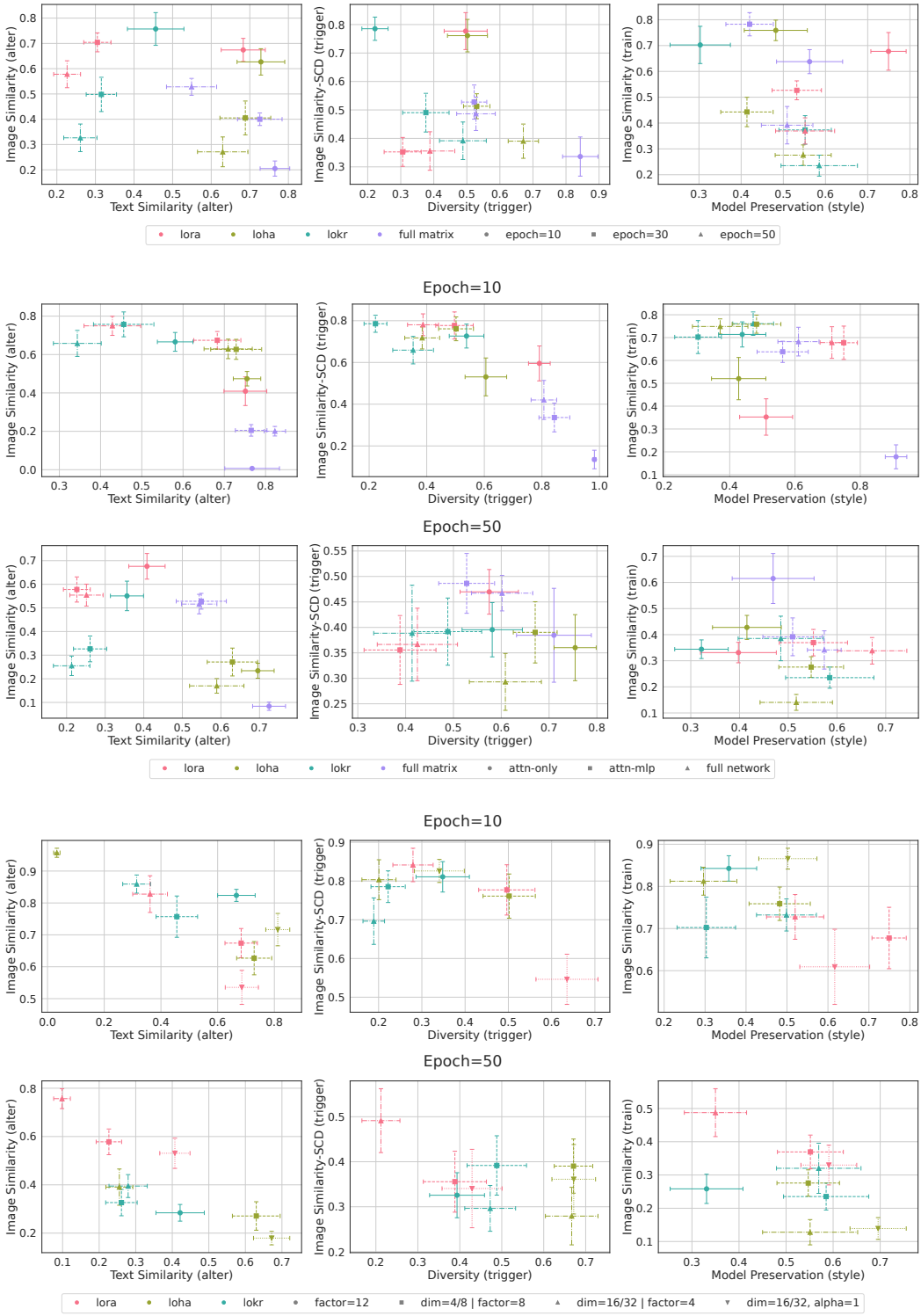


Figure 12: Scatter plots comparing different evaluation metrics for the category “Scenes”, with variations across algorithms and either *i*) top: number of training epochs, *ii*) middle: trained layers, or *iii*) bottom: dimensions, factors, and alphas.

F.3 Plots for Category “Stuffed Toys”

The plots for the “stuffed toys” category are shown in Figures 13 to 15. Following the reasoning of Appendix F.2, the SHAP analysis is only conducted with epoch 10 checkpoints. For the most part, these plots corroborate the statements of Section 5.3, and much like for the “scenes” category, LoRA and LoHa perform similarly here. Although the evaluation metrics indicate that training LoRA leads to greater diversity at the expense of base model style preservation, this trend is not visually discernible in the generated images. Another interesting observation is the significant improvement in base model style preservation for LoKr when the factor is decreased, which corresponds to an increase in model capacity. We further investigate this phenomenon in Appendix G.4.3.

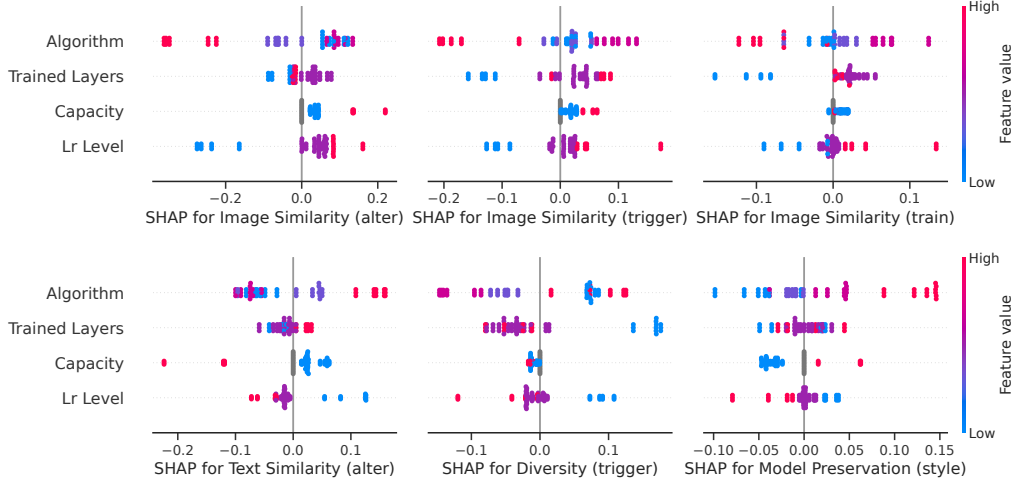


Figure 13: SHAP beeswarm charts for the category “Stuffed Toys” showing the impact of diverse algorithm factors on the evaluation metrics. LoRA is in blue, LoHa is in purple, LoKr is in purple red, and native fine-tuning is in red.

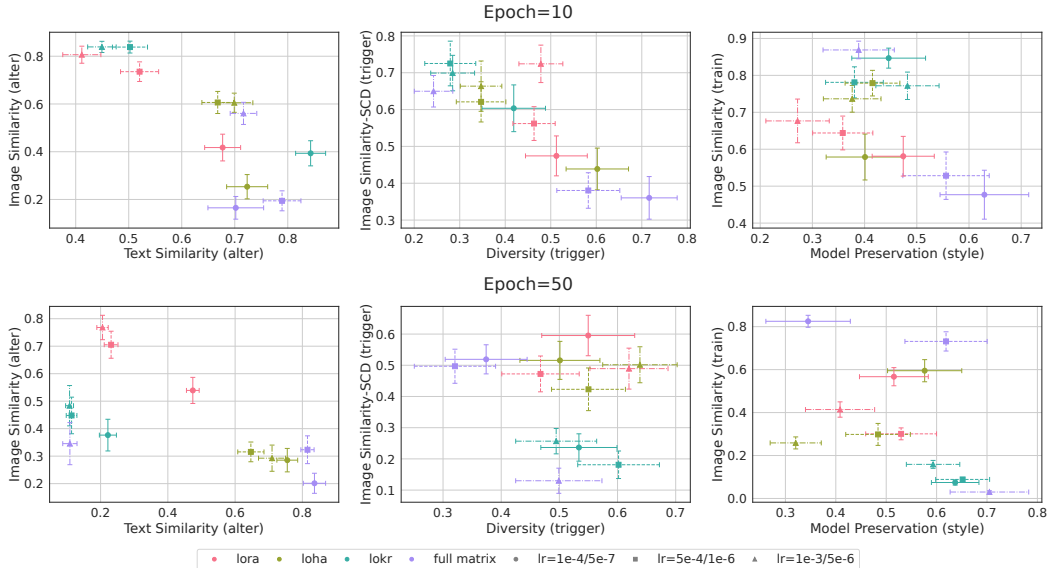


Figure 14: Scatter plots comparing different evaluation metrics for the category “Stuffed Toys”, with variations across algorithms and learning rates. As in Section 5.3, in the middle column we use squared centroid distance (SCD) to measure image similarity.

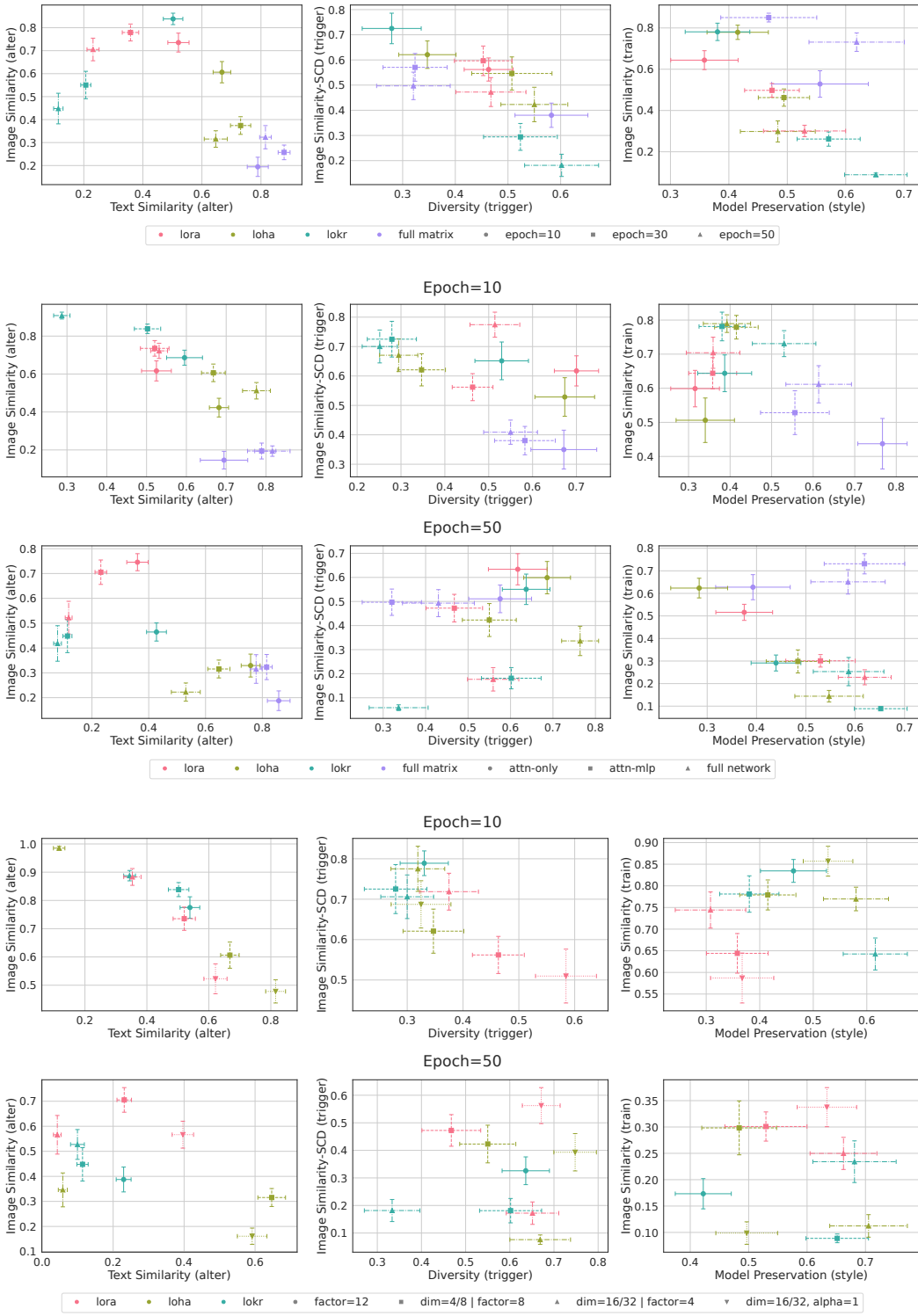


Figure 15: Scatter plots comparing different evaluation metrics for the category "Stuffed Toys", with variations across algorithms and either i) top: number of training epochs, ii) middle: trained layers, or iii) bottom: dimensions, factors, and alphas.

F.4 Plots for Category “Anime Characters”

The plots for the “anime characters” category are shown in Figures 16 to 18. As we will discuss in Appendix G.2, the metrics that we consider are less suitable for this category. There are thus a number of inconsistencies with our general guidelines that can be attributed to the limitations of these metrics, especially for the image similarity of images generated from training prompts. In spite of this, it could still be surprising to see that text-image alignment for generalization prompts gets improved over training. Our qualitative results in Appendix G.4.2 suggest that this can indeed happen.

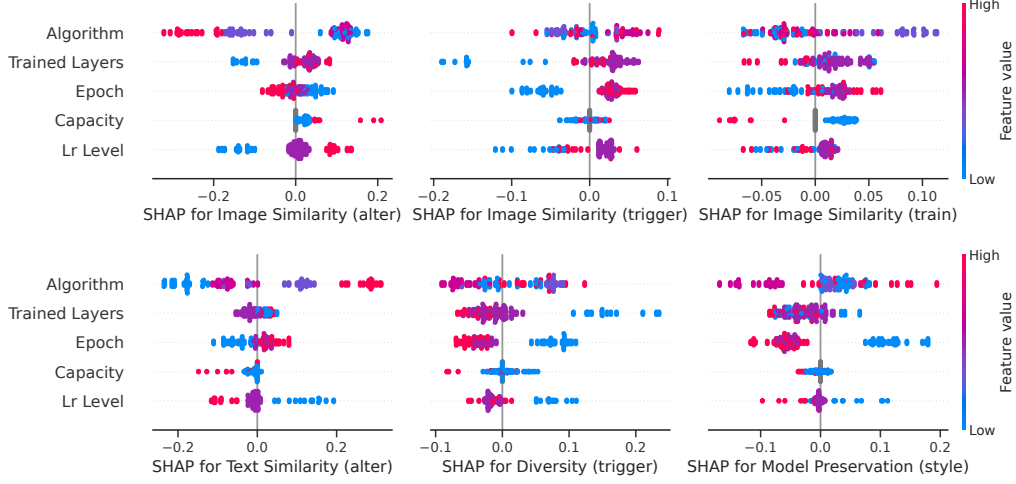


Figure 16: SHAP beeswarm charts for the category “Anime Characters” showing the impact of diverse algorithm factors on the evaluation metrics. LoRA is in blue, LoHa is in purple, LoKr is in purple red, and native fine-tuning is in red.

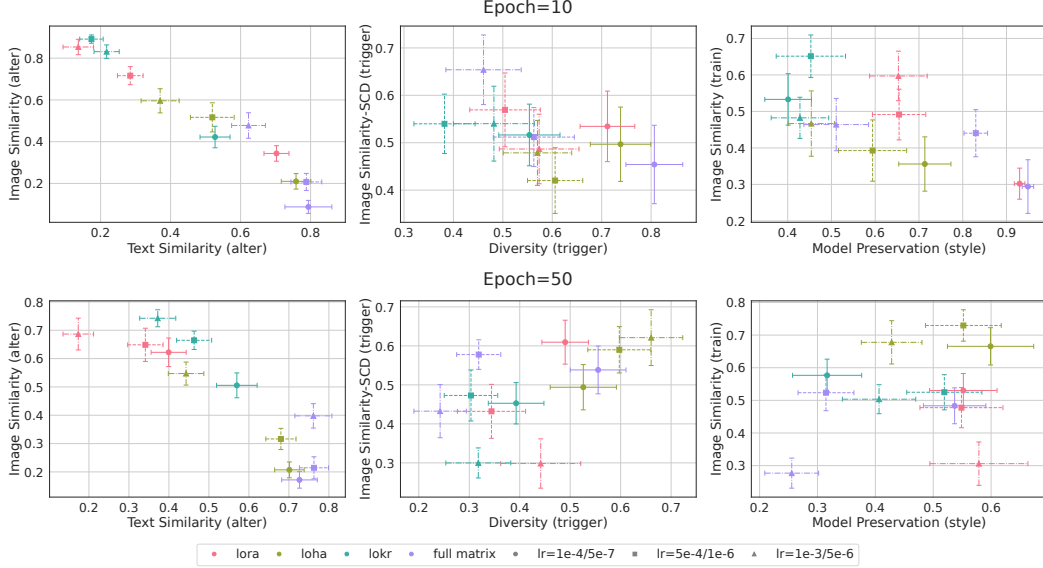


Figure 17: Scatter plots comparing different evaluation metrics for the category “Anime Characters”, with variations across algorithms and learning rates. As in Section 5.3, in the middle column we use squared centroid distance (SCD) to measure image similarity.

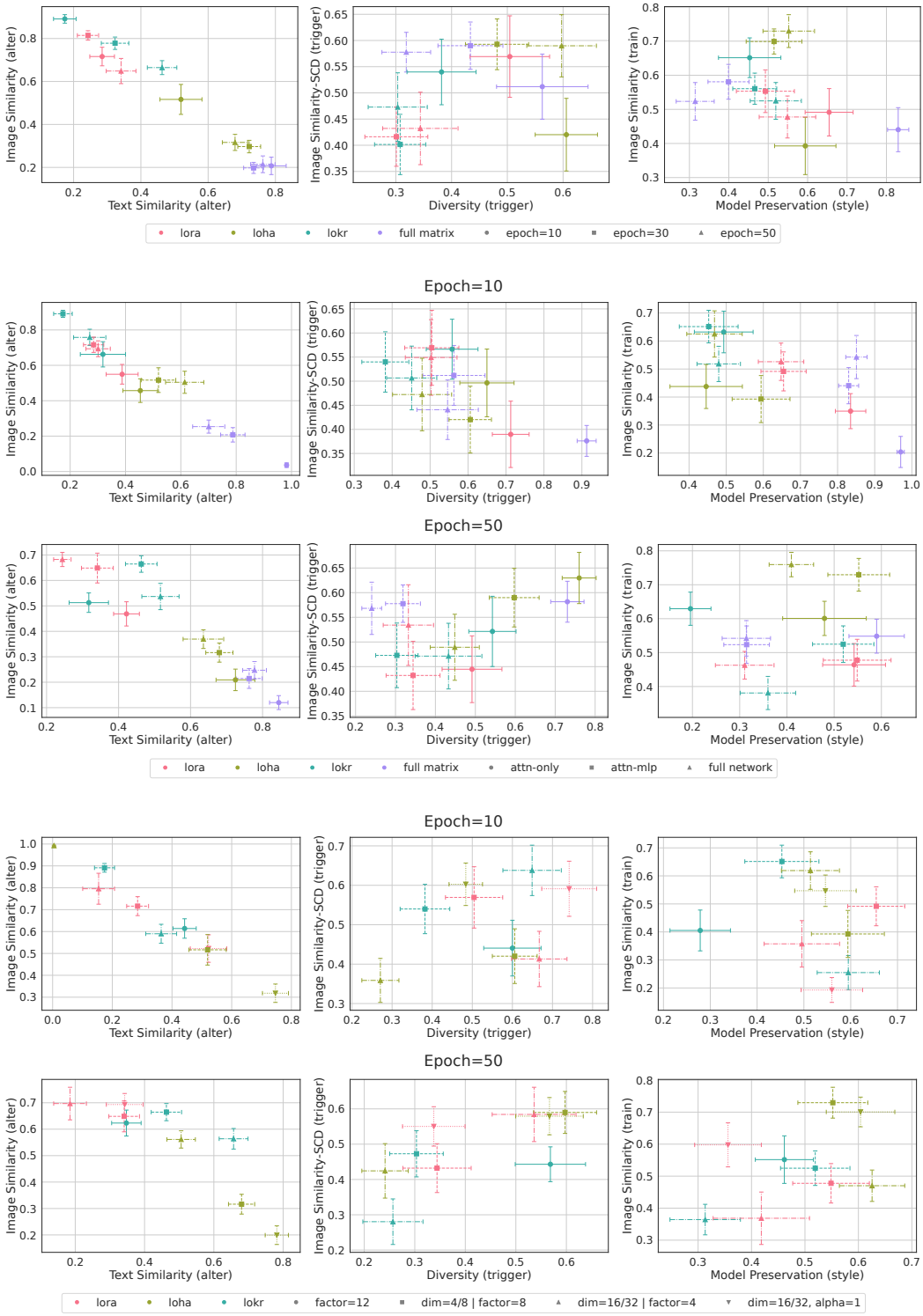


Figure 18: Scatter plots comparing different evaluation metrics for the category "Anime Characters", with variations across algorithms and either i) top: number of training epochs, ii) middle: trained layers, or iii) bottom: dimensions, factors, and alphas.

F.5 Plots for Category “Styles”

The plots for the “styles” category are shown in Figures 19 to 21. These plots differ from the plots for the other categories in the two following ways: First, we also use average style loss to evaluate concept fidelity. For consistency, in the plots, we still use “Image Similarity” to refer to the average cosine similarity measured in the DINOv2 feature space, and we use “Style Similarity” to refer to the similarity measured by the average style loss between dataset and generated images. Second, we do not measure base model style preservation here.

As we can see in the plots, the tendency suggested by the two different ways to measure fidelity do not always agree, and violations of the claims made in Section 5.3 are common. In fact, despite the seemingly advantage of using style loss to measure style similarity as we will demonstrate in Appendix H.1, we recognize this metric may still fall short of capturing all the nuanced elements that should be considered when comparing styles reproduced by different models. Furthermore, the very notion of what we refer to as “style” is inherently ambiguous and may require more specific and finely detailed methods of study. Consequently, it becomes challenging for us to render a definitive judgment on this topic. For illustration, some generated images for this category are shown in Appendix G.5.

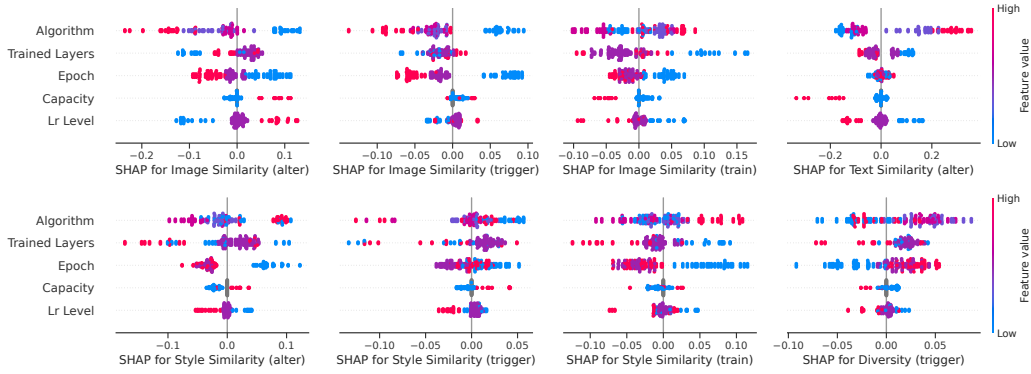


Figure 19: SHAP beeswarm charts for the category “Styles” showing the impact of diverse algorithm factors on the evaluation metrics. LoRA is in blue, LoHa is in purple, LoKr is in purple red, and native fine-tuning is in red.

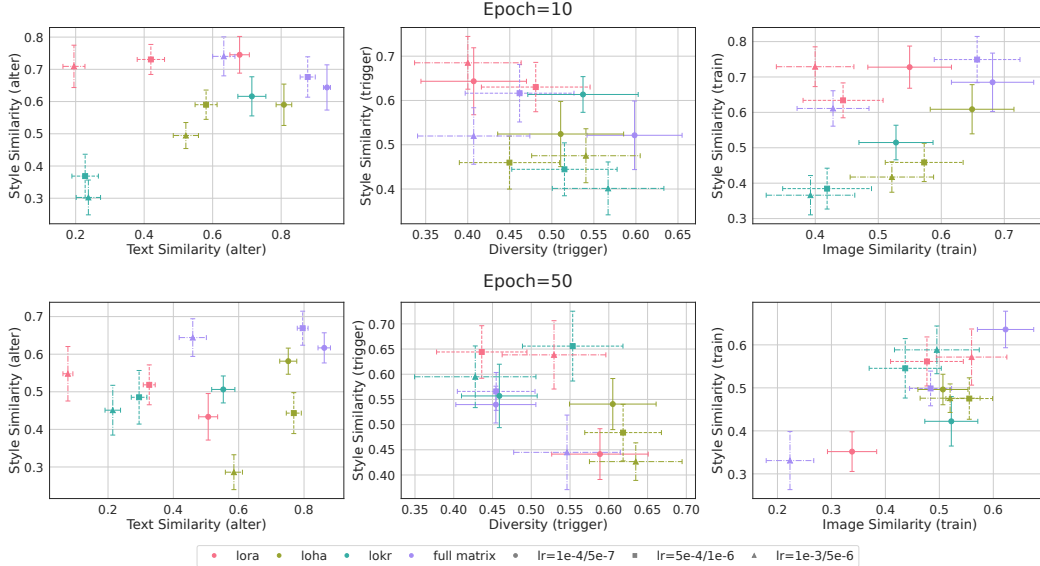


Figure 20: Scatter plots comparing different evaluation metrics for the category “Styles”, with variations across algorithms and learning rates.

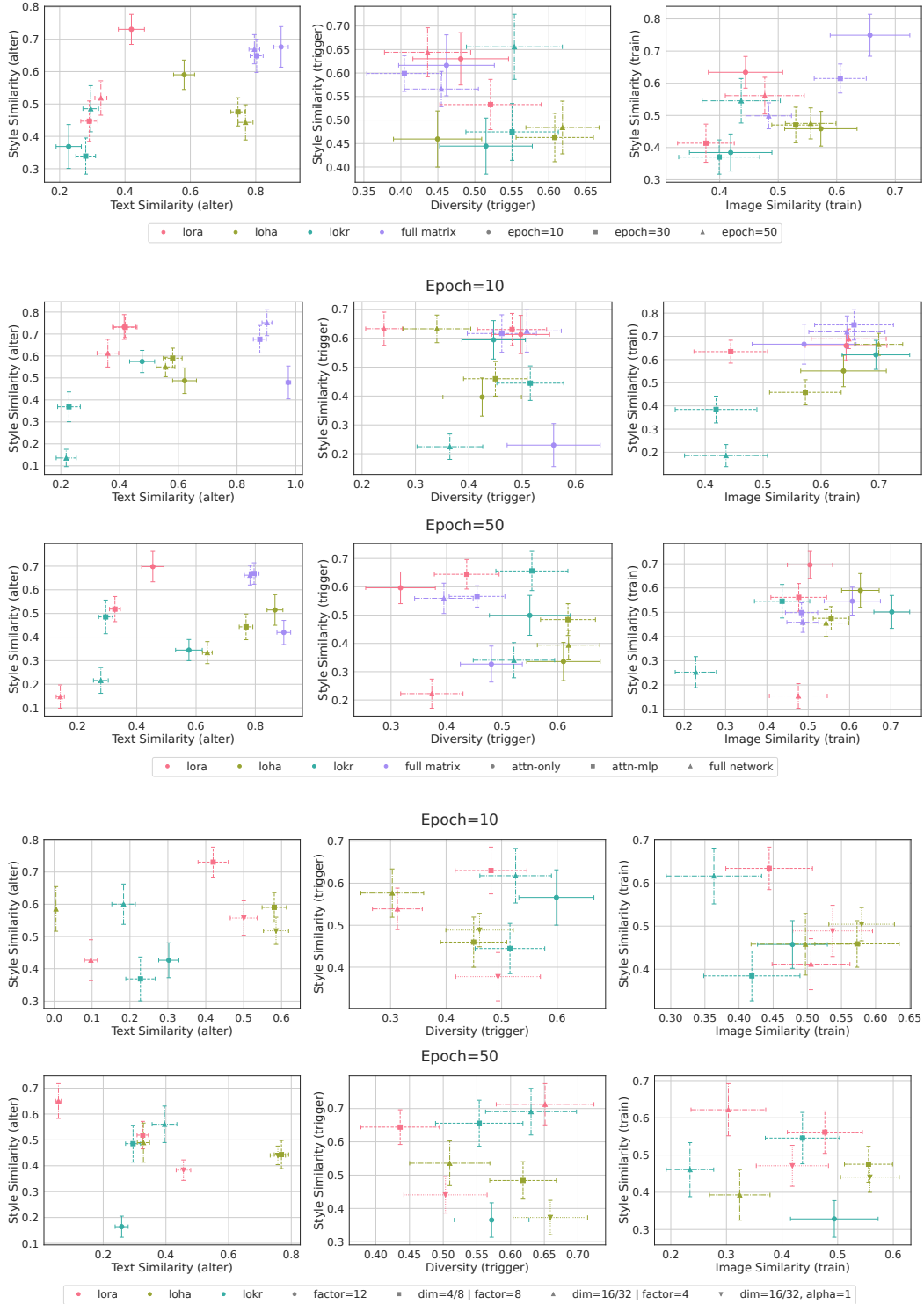


Figure 21: Scatter plots comparing different evaluation metrics for the category “Styles”, with variations across algorithms and either *i*) top: number of training epochs, *ii*) middle: trained layers, or *iii*) bottom: dimensions/factors, and alphas.

G Further Qualitative Results

In this section, we include an extensive set of qualitative results to support the claims that we have made throughout the paper. We highlight especially the challenges in algorithm evaluation, the prevailing trends related to the impact of different algorithmic factors, and some noteworthy deviations from these general principles. As for the prompts that are used to generate these images, please refer to [Appendix D.3](#).

G.1 Discrepancy of Results Across Classes

We have seen in [Section 5.3](#) and [Appendix F](#) that the performance of an algorithm can vary greatly across different concept categories. This variability is due to both differences in the number of training samples as well as intrinsic differences in the complexities of the concepts themselves. In [Figures 22](#) and [23](#), we further demonstrate that such discrepancies can still occur even among classes with the same type of objects and comparable number of images. In [Figure 22](#), the left model learns the “lobster stuffed toy” concept better, while the right model has more success with the “panda stuffed toy” concept. In [Figure 23](#), the left model allows to generalize the “canal” concept to broader contexts while the right model has more flexibility when dealing with the “garden” concept.

G.2 Unreliability of Metrics

While it is expected that the considered metrics may not always give results that align with human perception, it remains the hope that these deviations are simply “noises” that can be averaged out when we perform the evaluation on a large number of images. Unfortunately, this is not necessarily the case. For example, CLIP score for measuring text-image alignment often fails to understand compositional relationships between objects or attributes ([Thrush et al., 2022](#); [Yuksekgonul et al., 2023](#)). Here, we further demonstrate that the image similarity metrics we consider may have some inconsistencies in fully capturing the nuances of likeness across various image types, and this becomes more noticeable for categories that are less commonly seen during the pretraining of the encoders. Concretely, [Figure 17](#) suggests that a model trained with native fine-tuning at a learning rate of $5 \cdot 10^{-6}$ has the lowest image similarity for images generated with training prompts in the “anime characters” category. On closer inspection, we find this is misleading. A specific example is given in [Figure 24](#), where we demonstrate that none of the encoders we consider could accurately assess similarity in anime character appearance.

Such observations caution against an over-reliance on metrics, and emphasize the importance of using task-relevant metrics and encoders. In particular, the metrics we consider in our work may not be nuanced enough for specialized applications.

G.3 Illustrating the Impact of Different Algorithm Components

In this part, we illustrate the general principles that we established in [Section 5.3](#) through qualitative examples of three (sub-)classes: Abukuma [dark color uniform], Bohdi Rock [realistic], and castle. Example images for these three (sub-)classes are provided in [Figure 25](#).

G.3.1 A Case Study on Sub-Class “Abukuma [Dark Color Uniform]”

It is known that Stable Diffusion 1.5 does not perform well in generating anime-style images. Moreover, complex outfits are generally hard to learn. With these in mind, we believe that the uniforms of “Abukuma” would be a good test bed to evaluate the methods’ capacity in learning more difficult concepts. We visualize the images generated with the prompt “[V_{abukuma}] anime girl, [V_{dark uniform}] outfit” in [Figure 26](#) (we consider the epoch 50 checkpoints here for they being the ones that are the most trained). Although none of the models can perfectly reproduce the outfit, we do notice that a number of them can generate quite similar uniforms. This includes LoRA and LoKr trained with default parameters, and native fine-tuning with learning rate $5 \cdot 10^{-6}$. For LoHa, among all the considered configurations, only increasing both dimension and alpha allows us to learn the outfit to some extent. For LoRA and LoKr, with the hyperparameters that we consider, fine-tuning only the attention layers is however not sufficient for learning the appearance of the outfit.

Target Concept	LoKr factor 8	LoKr factor 4
		
		

Figure 22: Example generations for “lobster” and “panda” classes using two 10 epoch checkpoints trained with different algorithm configurations. The first 5 prompts of type <alter> are used to generate these samples.

Target Concept	LoRA dim 32 alpha 1	LoHa dim 16 alpha 1
		
		

Figure 23: Example generations for “canal” and “garden” classes using two 10 epoch checkpoints trained with different algorithm configurations. The first 5 prompts of type <alter> are used to generate these samples.

Reference



LoHA
dim 4
alpha 2
lr=5e-4

Generated Images



Image Similarity

CLIP
0.724

ConvNeXt V2
0.655

DinoV2
0.660

Native
Fine-tuing
lr=5e-6



CLIP
0.704

ConvNeXt V2
0.583

DinoV2
0.625

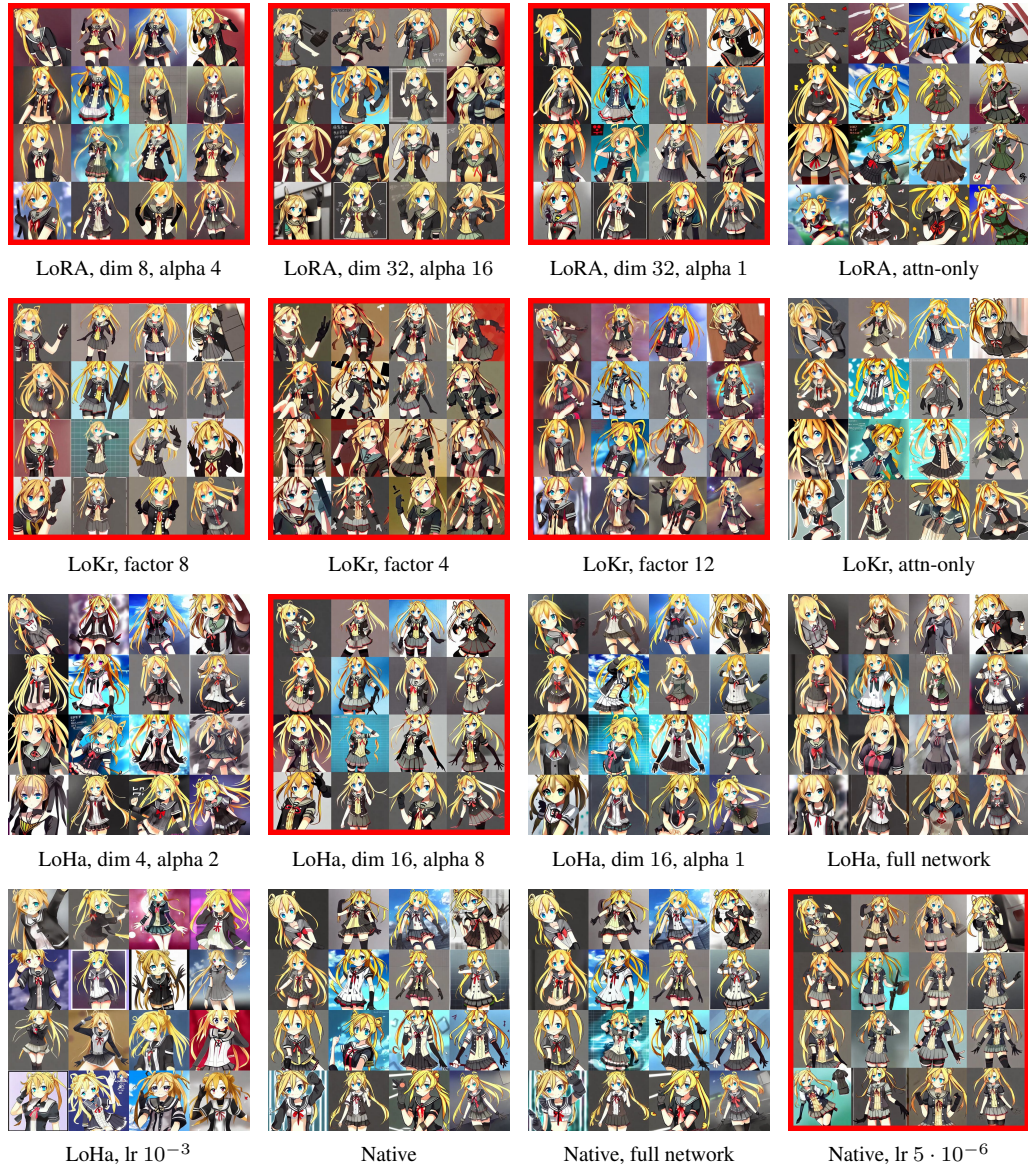
Figure 24: An illustrative example showing that image similarity scores could be misleading. Here, we compute the average cosine similarity between the features of the generated images and of the reference image shown on the left top corner. We consider images generated from two epoch 50 checkpoints. No matter what encoder we use, we get a higher score for the top model. Nonetheless, looking closely at the hairstyle, the outfit, and the armband, one would conclude that the bottom model performs better in generating the same character.



Abukuma [dark color uniform]

Bohdi Rook [realistic]

castle

Figure 25: Example training images for the three (sub-)classes studied [Appendix G.3](#).**Figure 26:** Example generations for “Abukuma [dark color uniform]” from checkpoints trained with different configurations. The images are generated with only the concept descriptor (i.e., trigger and class words) as input. These checkpoints are obtained after 50 training epochs and the default hyperparameters are used unless otherwise specified. Models that learn this concept more successfully are marked with red frames.

G.3.2 A Case Study on Class “Castle”

We next zoom in on the learning of the class “castle”. We first present a number of failure cases in [Figure 27](#). For models with higher capacity, we observe an increased tendency for mode collapse and artifacts that arise from overtraining (the latter, of course, can potentially be avoided by reducing the number of training epochs). On the other hand, when the learning rate is too small, even with native fine-tuning, we may fail to learn the concept correctly, and this cannot be solved with a larger number of training epochs. In particular, we see that after 50 epochs of native fine-tuning at learning rate 10^{-6} , the image quality already gets compromised while the concept is still barely learned.



Figure 27: Illustrations of typical failures that we may encounter during concept customization. This includes mode collapse (leftmost), overtraining artifact (second to the left), and underfitting (right two). These images are generated for class “castle” with prompts of type `<alter>`. The left three models are trained for 10 epochs.

The generated images of several other models are presented in [Figures 29 to 32](#) (we show the results obtained from the epoch 10 checkpoints as 30 epochs systematically cause overtraining for this concept). First, comparing LoRA, LoHa, LoKr trained with default hyperparameters and native fine-tuning with learning rate $5 \cdot 10^{-6}$, we can see that LoKr and LoHa respectively give the most and the least fitted model. This can be adjusted by modifying the hyperparameters. In particular, we show in these figures that a LoRA with higher model capacity (higher dimension and alpha) would be more fitted than a LoKr with lower model capacity (higher factor).

Another observation from these figures is the occurrence of concept leaks from other classes. For instance, elements like waterfalls and sculptures from two other classes (illustrated in [Figure 28](#)) appear in several generated samples in [Figure 31](#). This leakage appears to stem from either the word “forest” or “peacock”, and is more pronounced in models that are more fitted to the concepts. Notably, this phenomenon is less observed in LoHa, LoKr with a factor of 12, and native fine-tuning.

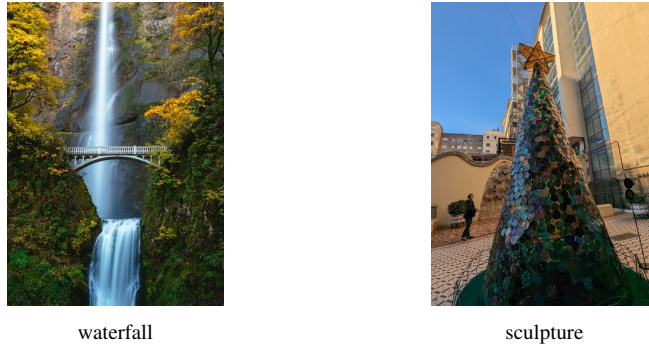


Figure 28: Examples training images for the two classes “waterfall” and “sculpture”.

G.3.3 A Case Study on Sub-Class “Bodhi Rook [Realistic]”

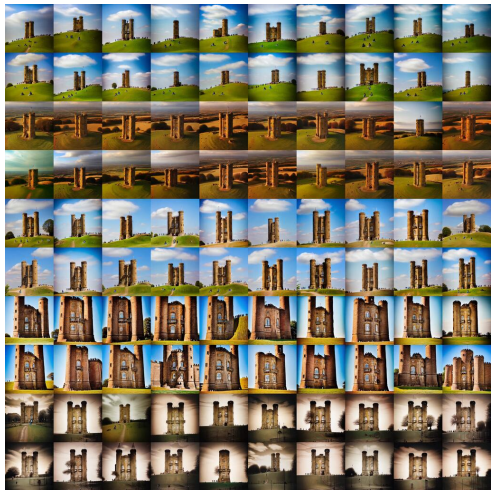
Here, we turn our attention to the generation of photorealistic images of Bodhi Rook, with sample generations shown in [Figures 33 to 36](#). We find most models perform equally well in generating the character (while some details may still be to desired, we leave the judgement to the readers). Nonetheless, the models that are considered to be “more fitted”, such as LoRA and LoKr with default



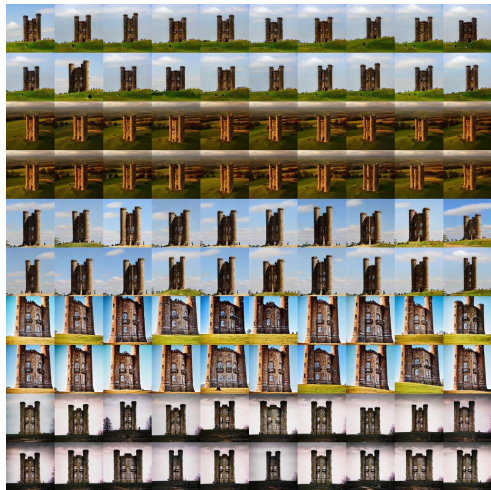
(a) LoRA with dimension 32, alpha 16



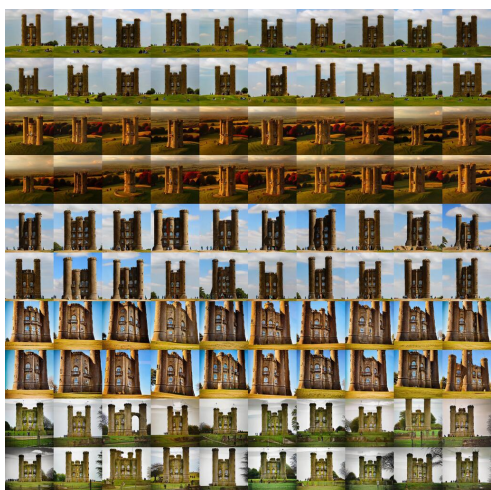
(b) LoKr with factor 12



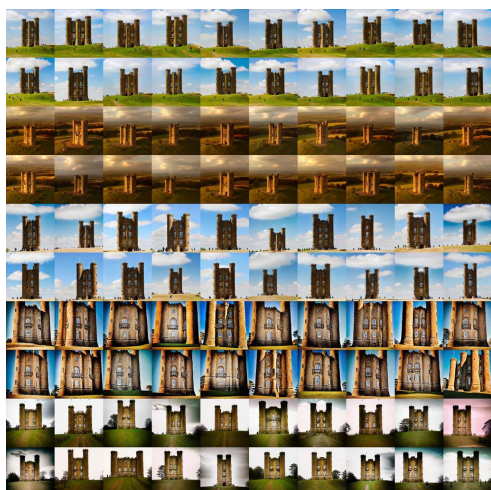
(c) LoRA



(d) LoKr



(e) LoHa



(f) Native fine-tuning with learning rate $5 \cdot 10^{-6}$

Figure 29: Synthetic images of class “castle” that are generated using the prompts of type <train>. The models are trained for 10 epochs and the default hyperparameters are used unless otherwise specified.



(a) LoRA with dimension 32, alpha 16



(b) LoKr with factor 12



(c) LoRA



(d) LoKr



(e) LoHa



(f) Native fine-tuning with learning rate $5 \cdot 10^{-6}$

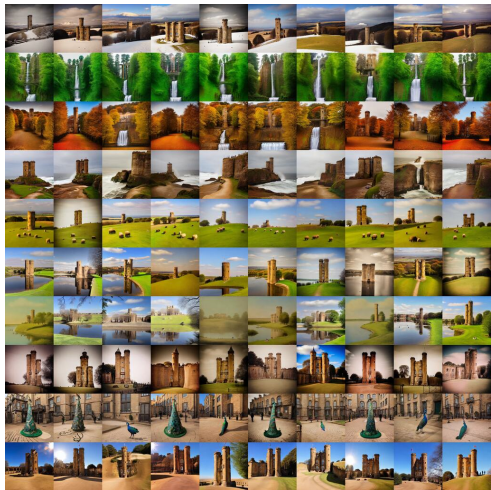
Figure 30: Synthetic images of class “castle” that are generated using the prompts of type <trigger>. The models are trained for 10 epochs and the default hyperparameters are used unless otherwise specified.



(a) LoRA with dimension 32, alpha 16



(b) LoKr with factor 12



(c) LoRA



(d) LoKr



(e) LoHa



(f) Native fine-tuning with learning rate $5 \cdot 10^{-6}$

Figure 31: Synthetic images of class “castle” that are generated using the prompts of type <alter>. The models are trained for 10 epochs and the default hyperparameters are used unless otherwise specified.



(a) LoRA with dimension 32, alpha 16



(b) LoKr with factor 12



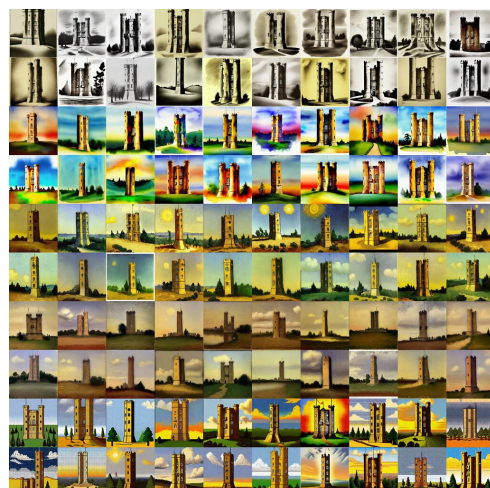
(c) LoRA



(d) LoKr



(e) LoHa



(f) Native fine-tuning with learning rate $5 \cdot 10^{-6}$

Figure 32: Synthetic images of class “castle” that are generated using the prompts of type <style>. The models are trained for 10 epochs and the default hyperparameters are used unless otherwise specified.

hyperparameters, and native fine-tuning with learning rate $5 \cdot 10^{-6}$ would have a higher tendency to generate clothes that look similar to those in the dataset, even when it is asked to generate a different outfit, as seen in the “chef’s outfit” examples in the second row of each image grid in [Figure 35](#). In spite of this, these models are still flexible enough to capture other elements of the prompts, such as backgrounds, like cherry blossoms, poses, like kneeling, or interactions, like playing with dogs.

Yet another way to distinguish between these groups of models is to look at image diversity when we only prompt with the concept descriptor “[V_{bodhi} rook] man, realistic”. Models with lower learning rate (LoKr with learning rate 10^{-4} , native fine-tuning with default learning rate 10^{-6}) and LoHa clearly have more diverse generations as can be seen from [Figure 34](#). It is worth noticing that it may not always be possible to really compare the diversity of two sets of images, as one set may be more diverse in background while the other being more diverse in pose, but this does not seem to be the case here. Finally, we do observe that native fine-tuning seems to yield models with the best base model style preservation for this sub-class, no matter whether we train with learning rate 10^{-6} or $5 \cdot 10^{-6}$, as shown in [Figure 36](#).

G.4 Violations of the General Principles

The goal of this section is to showcase a number of violations to the general principle that we outlined in [Section 5.3](#). Such exceptions indicate that we are still far from having a comprehensive understanding of the myriad factors that influence the fine-tuning process.

G.4.1 LoRA with Better Style Preservation for “Canal” and “Waterfall”

We have seen in [Figure 36](#) that for the sub-class “Bodhi Rook [realistic]”, native fine-tuning seems to perform the best in terms of base model style preservation. Nonetheless, the plots shown in [Appendix F.2](#) suggest that this would not be the case for the “scenes” category. Instead, the metrics suggest that LoRA has the best base model style preservation in this case. Upon visual inspection, we confirmed that this is indeed the case, as evidenced by the examples provided in [Figure 37](#). This observation highlights the benefits of reducing the number of fine-tuned parameters especially when working with a small dataset.

G.4.2 Improved Controllability Over Training

Although more training would generally increase concept fidelity at the expense of controllability, this rule does not hold universally. For example, [Figures 16 to 18](#) in [Appendix F.4](#) suggest that, when considering the “anime characters” category, the models’ text-image alignment for generalization prompts actually improves with more training. While the difference is rather subtle, we do observe this for several configurations as shown in [Figures 38](#) and [39](#). Specifically, note how “Tsushima Yoshiko” is more likely to be depicted riding a horse, as indicated by the prompt in [Figure 38](#) after longer training (8th row of the grids). Similarly, “Yuuki Makoto” dons a more accurate space suit when LoKr undergoes more training, as shown in the 5th row of the grids in [Figure 39](#). This tendency might be linked to the fact that Stable Diffusion 1.5 struggles with generating anime-style images. For these specific concepts, it appears that the models need to *overfit before generalize*.

In a related vein, this phenomenon bears similarities to what is described as grokking ([Power et al., 2022](#)) or double descent ([Nakkiran et al., 2021](#)) in the literature. More compelling evidence for this comes from training LoHa with a dimension of 16 and an alpha value of 8. Here, the overfit-then-generalize effect is not confined to the “anime characters” category but becomes more pronounced across all classes. Initially, after 10 epochs of training, the model barely reacts to the prompts. However, its generalization capabilities show a significant improvement after 50 epochs of training. An illustration of this is given in [Figure 40](#). It is also worth noticing that this behavior is consistent across all three runs trained with identical configurations but different random seeds, suggesting that this is not merely coincidental. Indeed, this trend is also manifested in our plots in [Appendix F](#). In the 10-epoch plots, the point representing this configuration, denoted by a yellow triangle, consistently occupies the upper-left corner when comparing “image similarity <alter>” against “text similarity <alter>”, while in the 50-epoch plots, this point shifts towards the lower-right corner.



(a) LoRA



(b) LoHa



(c) LoKr



(d) Native fine-tuning



(e) LoKr with learning rate 10^{-4}



(f) Native fine-tuning with learning rate $5 \cdot 10^{-6}$

Figure 33: Synthetic images of “Bodhi Rook [realistic]” that are generated using the prompts of type <train>. The models are trained for 30 epochs and the default hyperparameters are used unless otherwise specified. See Appendix G.3.3 for the accompanying discussion.



(a) LoRA



(b) LoHa



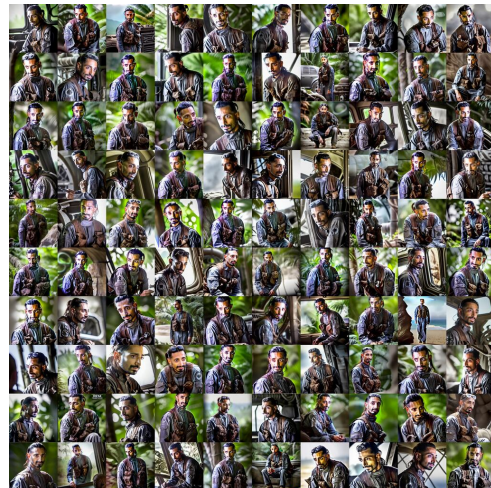
(c) LoKr



(d) Native fine-tuning



(e) LoKr with learning rate 10^{-4}



(f) Native fine-tuning with learning rate $5 \cdot 10^{-6}$

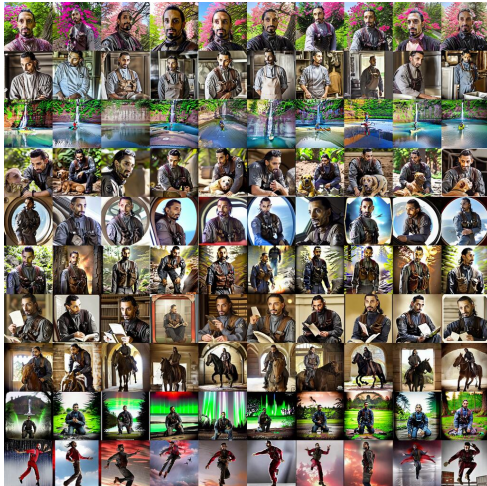
Figure 34: Synthetic images of “Bodhi Rook [realistic]” that are generated using the prompts of type <trigger>. The models are trained for 30 epochs and the default hyperparameters are used unless otherwise specified. See Appendix G.3.3 for the accompanying discussion.



(a) LoRA



(b) LoHa



(c) LoKr



(d) Native fine-tuning



(e) LoKr with learning rate 10^{-4}



(f) Native fine-tuning with learning rate $5 \cdot 10^{-6}$

Figure 35: Synthetic images of “Bodhi Rook [realistic]” that are generated using the prompts of type <alter>. The models are trained for 30 epochs and the default hyperparameters are used unless otherwise specified. See Appendix G.3.3 for the accompanying discussion.



(a) LoRA



(b) LoHa



(c) LoKr



(d) Native fine-tuning



(e) LoKr with learning rate 10^{-4}



(f) Native fine-tuning with learning rate $5 \cdot 10^{-6}$

Figure 36: Synthetic images of “Bodhi Rook [realistic]” that are generated using the prompts of type <style>. The models are trained for 30 epochs and the default hyperparameters are used unless otherwise specified. See Appendix G.3.3 for the accompanying discussion.



Figure 37: Example generations for classes “canal” and “waterfall” using the prompts of type `<style>` (cf. Appendix D.3). The models are trained for 10 epochs and the default hyperparameters are used unless otherwise specified. We note that LoRA seems to have the best style preservation here.



(a) Example image



(b) LoKr, epoch 10



(c) LoKr, epoch 50



(d) Native fine-tuning, lr $5 \cdot 10^{-6}$, epoch 10



(e) Native fine-tuning, lr $5 \cdot 10^{-6}$, epoch 50

Figure 38: Example image and generated samples for “Tsushima Yoshiko”. Prompts of type <alter> are used for the generations (cf. Table 5). We observe improved text-image alignment over training.



(a) Example image



(b) LoKr, epoch 10



(c) LoKr, epoch 50



(d) Native fine-tuning, lr $5 \cdot 10^{-6}$, epoch 10



(e) Native fine-tuning, lr $5 \cdot 10^{-6}$, epoch 50

Figure 39: Example image and generated samples for “Yuuki Makoto”. Prompts of type <alter> are used for the generations (cf. Table 5). We observe improved text-image alignment over training.



(a) Generations with prompts of type <alter>



(b) Generations with prompts of type <style>

Figure 40: Example generations for sub-class “Saw Gerrera [afro, illustration]” using a LoHa with dimension 16 and alpha 8. From left to right we use respectively the epoch 10, 30, and 50 checkpoints. We observe that both text-image alignment and style preservation improve over training.

G.4.3 Richer Stylistic Variations with Increased Model Capacity

While our general guidelines propose that increasing a model’s capacity—while keeping other hyperparameters constant (for alpha, we maintain the alpha/dimension ratio)—tends to diminish the model’s ability to preserve the base model’s style, Figure 13 for the “stuffed toy” category suggests otherwise. To better understand this apparent discrepancy, we delve deeper into this issue in Figure 41. For LoRA, there is no evidence for such improvement in base style preservation when increasing dimension and alpha. However, for LoKr, the improvement may be real. At least, LoKr with smaller factors (and hence larger capacity) seems to generate more stylistically rich images with <style> prompts, though whether these images authentically align with the styles specified in the prompts is subject to discussion. One plausible reason for the emergence of more stylistic images with larger models could be the presence of various styles in our dataset, which the model then incorporates during the fine-tuning process.

G.5 Example Generations for Category “Styles”

For the sake of illustration, we present a number of generated samples for the “styles” category in Figures 43, 45 and 47. We note that different styles need different number of training epochs and model capacity to be learned properly. Moreover, when the dataset only depicts a specific type of object, as in the class “Felix Vallotton”, increasing dimension and alpha of LoRA or LoHa can be harmful for these models’ performance on generalization prompts (cf. Figure 47). Conversely, these changes can be beneficial for the learning of other styles, as shown in Figure 43.

Generally speaking, the trend observed in these figures align with the guiding principles we outlined in Section 5.3. Although Figure 19 suggest that both image and style similarities decrease over training for these classes, we find no evidence of this. One potential explanation for this decrease could then be that the images become “oversaturated” in certain style classes as training progresses, as illustrated in Figure 45.

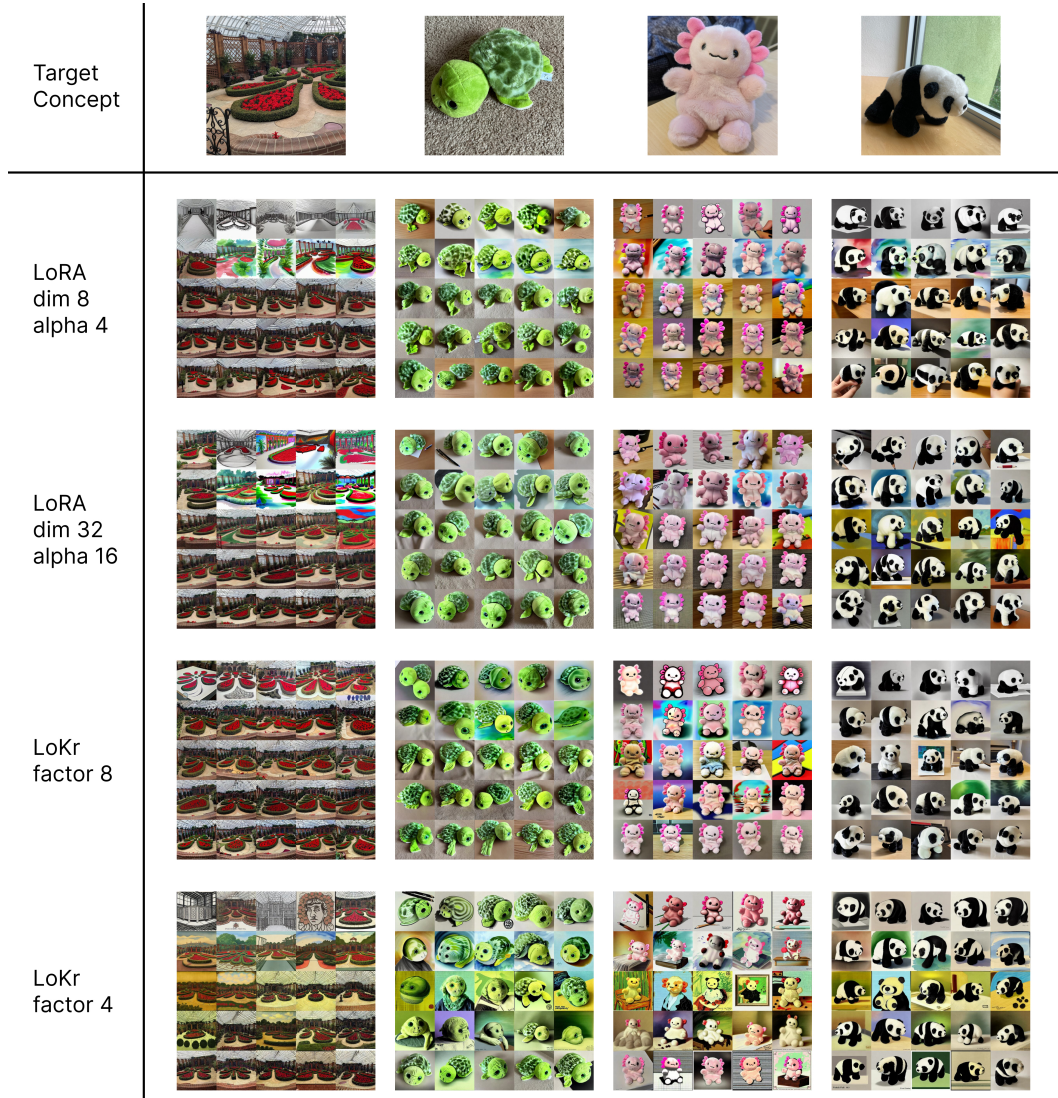


Figure 41: Generated images from four models trained with different configurations. The prompts of type <style> are used here (cf. [Appendix D.3](#)). Note that increasing model capacity enhances LoKr’s ability to generate more stylistically rich images.



Figure 42: Example training images for class “Ghibli 2”.

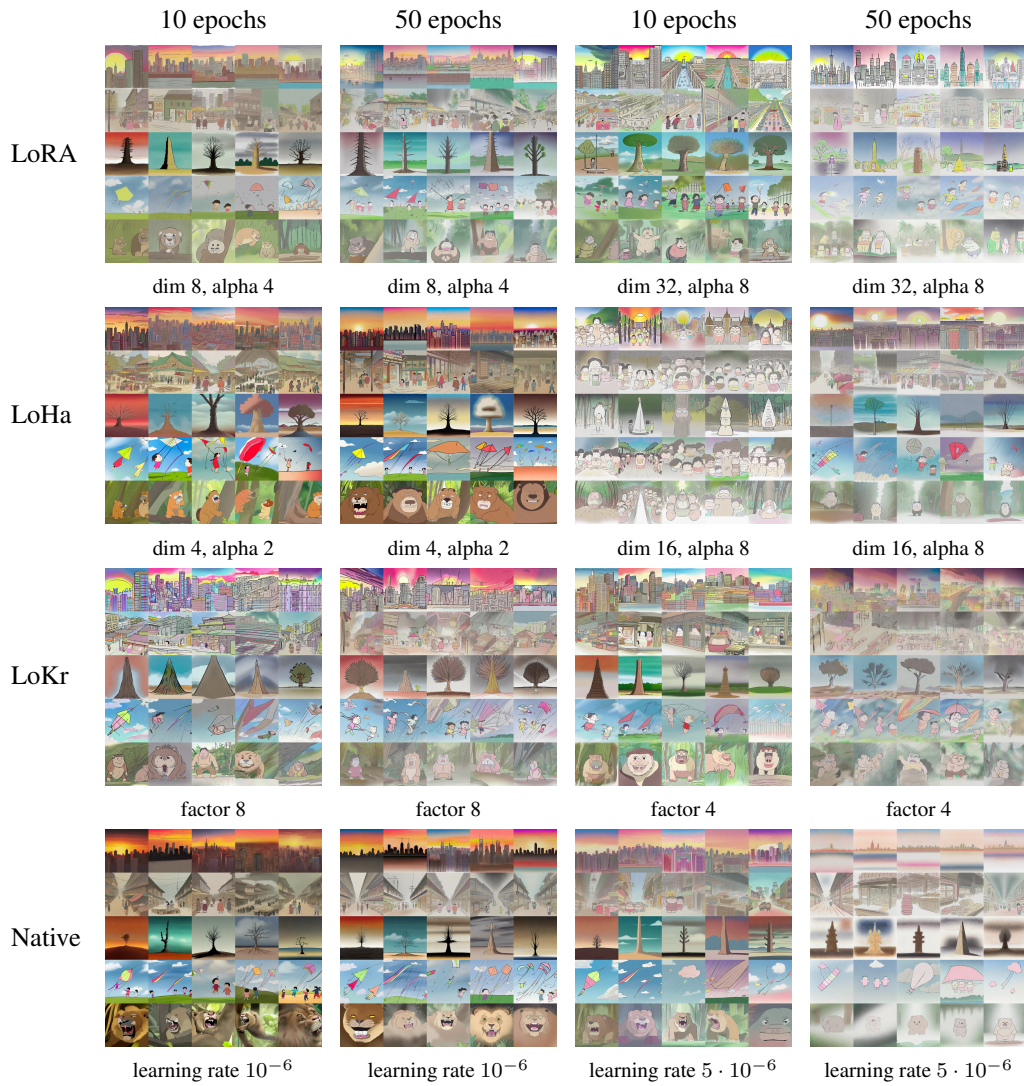


Figure 43: Example generations for “Ghibli 2” from different checkpoints. The first 5 prompts of type <alter> (cf. Table 5) are used to generate these images.



Figure 44: Example training images for class “impressionism”.

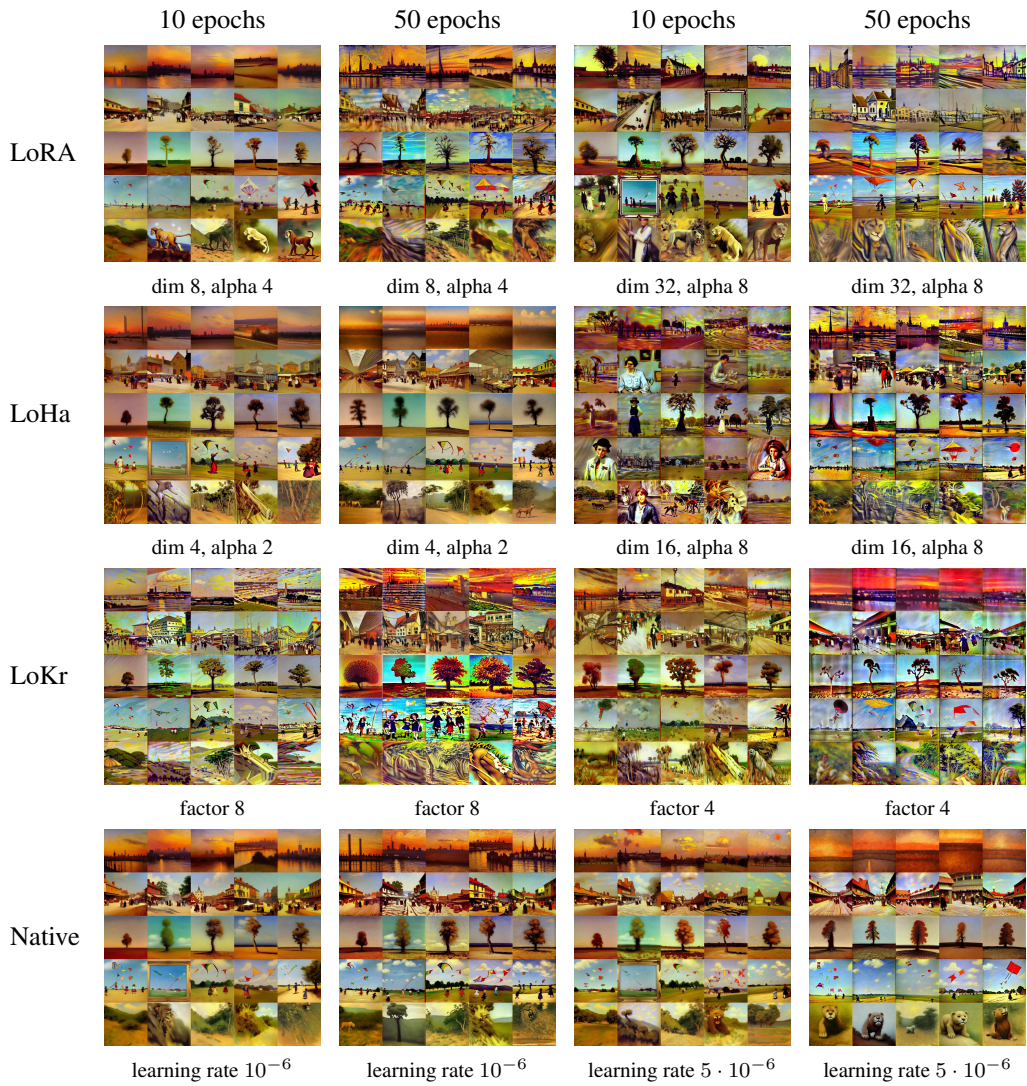


Figure 45: Example generations for “impressionism” from different checkpoints. The first 5 prompts of type <alter> (cf. Table 5) are used to generate these images.



Figure 46: Example training images for class “Felix Vallotton”.

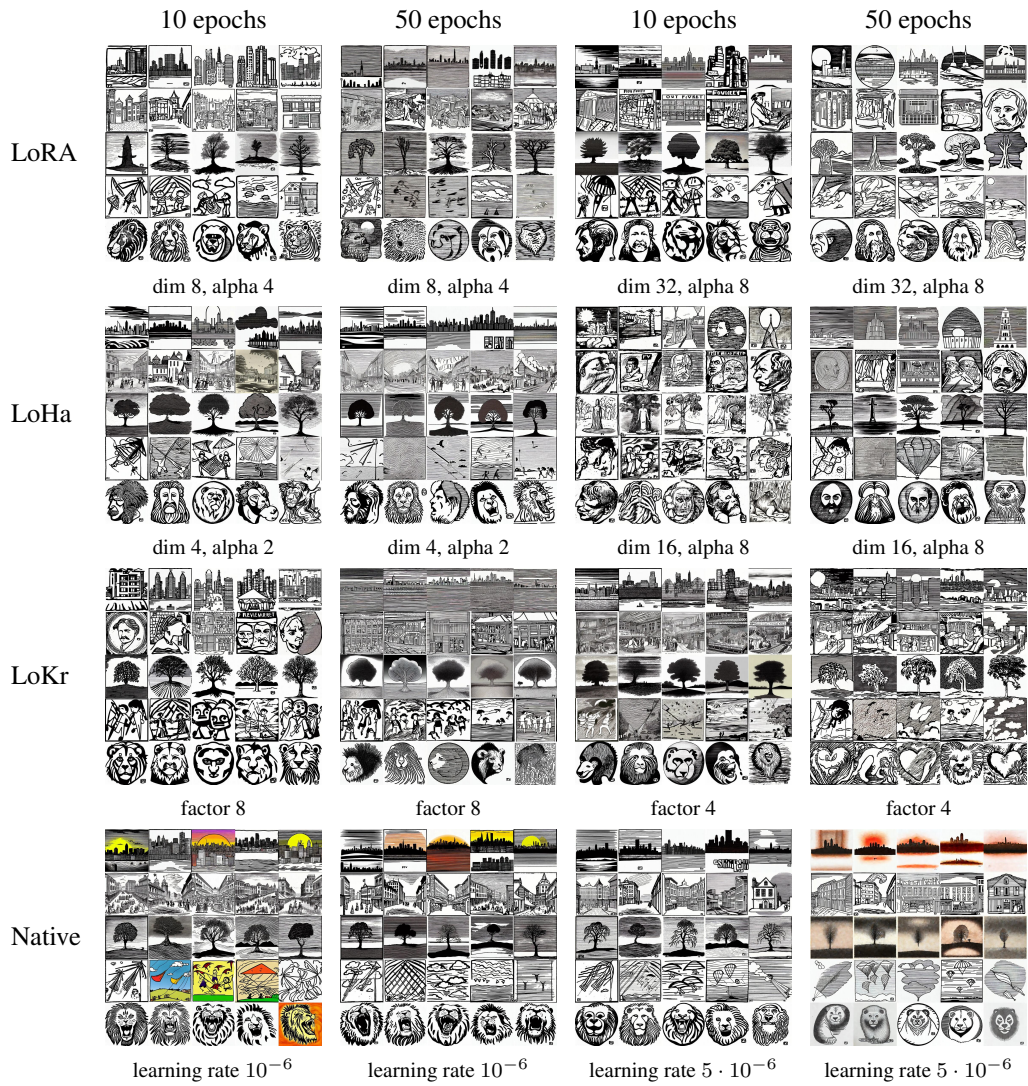


Figure 47: Example generations for “Felix Vallotton” from different checkpoints. The first 5 prompts of type <alter> (cf. Table 5) are used to generate these images.

H Additional Experiments

This appendix presents a number of additional experiments that have been omitted from the main text. These experiments validate some design choices that we have made for our main study, and provide further insights into fine-tuning of text-to-image models.

H.1 Investigating the Relevance of Image Features

The primary objective of this section is to investigate how different image features focus on distinct aspects when measuring similarity between images. This serves as a critical sanity check to shed light on why different encoders are preferable for calculating style loss versus semantic similarity.

Encoders and Resizing Methods. Precisely, we compare a number of ways to extract image features which mainly differ in the choice of encoders and resizing methods.

- **Encoders:** We consider four distinct encoders: DINOv2, CLIP, ConvNeXt V2, and VGG-19, as explained in Appendices D.4 and D.5. For VGG-19, the features are generated by concatenating the flattened normalized Gram matrices that are involved in the computation of the style loss.
- **Resizing Methods:** Four different resizing techniques are considered: scale, letterbox, center crop, and stretch. These are applied to DINOv2, CLIP, and ConvNeXt V2 as discussed in Appendix E. For VGG-19, we only consider the scale method as it can take non-square inputs.

In sum, we explore a total of 10 distinct encoding methods, each representing a unique combination of an encoder and a resizing technique.

Datasets. Our experiments make use of the following three classification datasets.

- **ImageNet100:** A subset of ImageNet (Russakovsky et al., 2015) containing 100 distinct classes, comprising a total of 130,000 images.¹⁵
- **DAF:re-250:** A subset of DAF:re (Rios et al., 2021) with 250 classes, featuring 99,361 images.
- **Style30:** An expanded version of the new WikiArt dataset (Tan et al., 2019), enriched with three additional style classes, summing up to 30 classes and 112,349 images. Notably, the “anime” class in this dataset contains artworks from 279 different artists and includes a total of 29,830 images. Each of these artists’ work can be further considered as a unique style.

By considering datasets with varied image types and classification criteria, we would like to dissect how changes in either the image’s style or content affect the distribution of different image features.

Diversity Ratio. Building upon the above, for each encoding method we compute the *diversity ratio* defined as $\text{diversity}_{\text{class}} / \text{diversity}_{\text{dataset}}$. It compares the intra-class feature diversity against the overall dataset diversity. Then, for example, low diversity ratios in our style dataset would imply that the features in question are particularly sensitive to stylistic changes, while high diversity ratios in other classification tasks might suggest their insensitivity to changes in the subject of the images.

Nonetheless, it still remains the question of how we evaluate feature diversity. For this, we consider three different metrics as listed below.

- **Vendi Score:** This follows the definition given in Appendix D.4.
- **Intra-Dissimilarity:** For a set of features \mathcal{Z} , its intra-dissimilarity is computed as $1 - S_C(\mathcal{Z}, \mathcal{Z})$ where S_C is the average cosine similarity metric defined in (22). This measure is directly related to the use of cosine similarity to assess the similarity of two images.
- **Variance:** We also consider the variance of the feature set. This is directly related to the use of Euclidean distance to assess the similarity of two images, as what we do in computing style loss.

It is worth noticing that the intra-dissimilarity is nothing but the variance of the normalized vectors, as can be seen from (23). Therefore, in reality, the only difference between the second and the third metrics boils down to whether the feature vectors are normalized or not.

¹⁵<https://www.kaggle.com/datasets/ambityga/imagenet100> (Accessed: 2023-08-20)

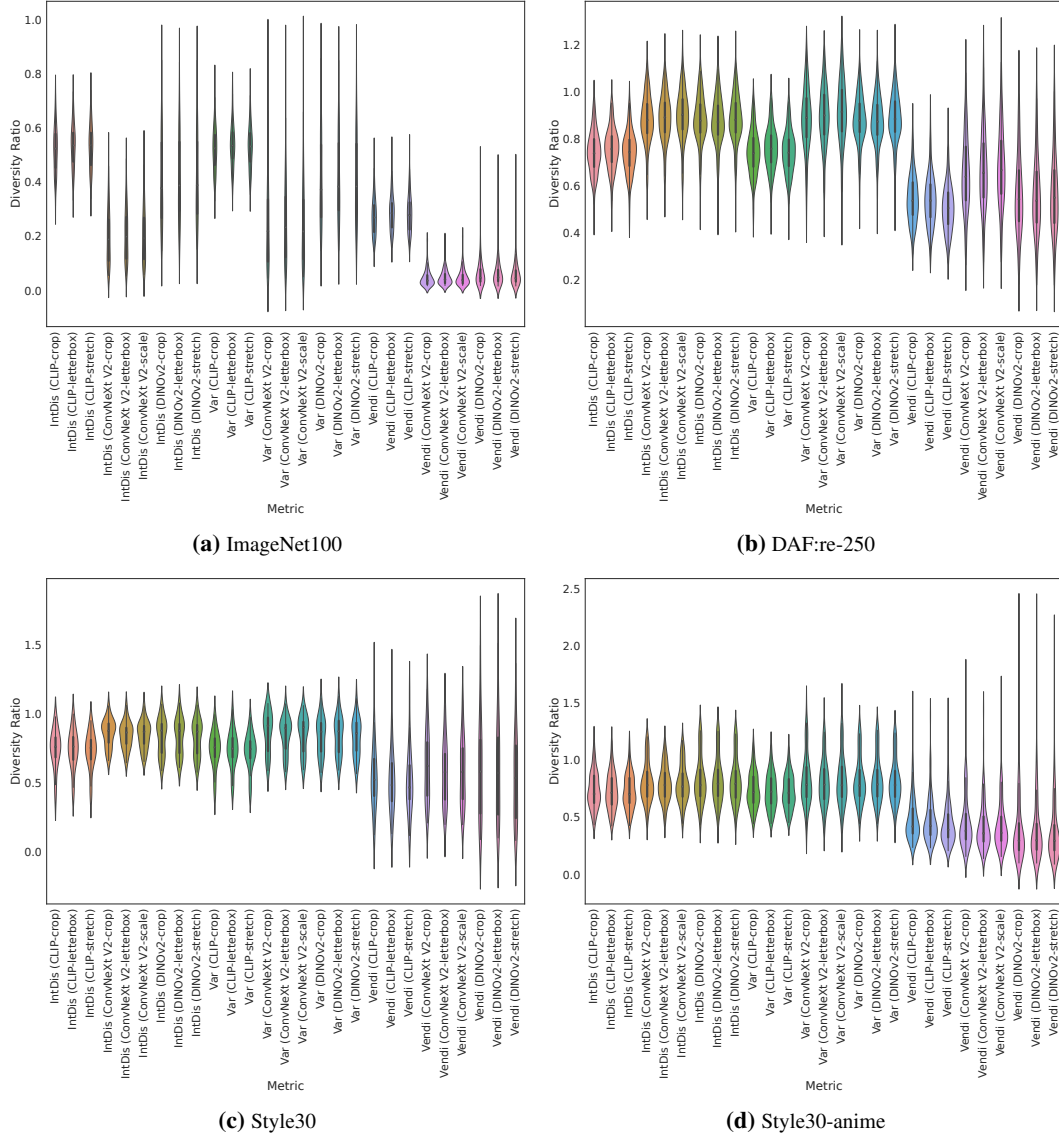


Figure 48: Distribution of diversity ratios across classes for different metrics/encoding methods. IntDis and Var respectively stand for intra-dissimilarity and variance. We observe that the choice of resizing methods has little influence on the results.

Result. We compute the diversity ratios for the three datasets, as well as for the anime class within the style dataset, putting each artist’s work in a separate sub-class. Moreover, we only compute diversity scores for classes with more than 50 images, and whenever we need to compute the diversity score for a set of more than 1,000 images, we sub-sample it to a fixed size of 1,000 before performing the computation. The distributions of the diversity ratios obtained in our experiments are shown in Figures 48 and 49.

In Figure 48, we see that the choice of resizing method has little influence on the results. This is consistent with what we have observed for our main experiments in the correlation analysis of Appendix E. We next zoom in on the influence of encoders and metrics in Figure 49. We first observe that the distributions of diversity ratios for intra-dissimilarity and variance are relatively close. For these two metrics, using the VGG-19 features gives lower diversity ratios for style datasets and higher diversity ratios for ImageNet100 and DAF:re-250, suggesting that VGG-19 features are indeed the most suitable for evaluating style similarity among all the four features that we consider

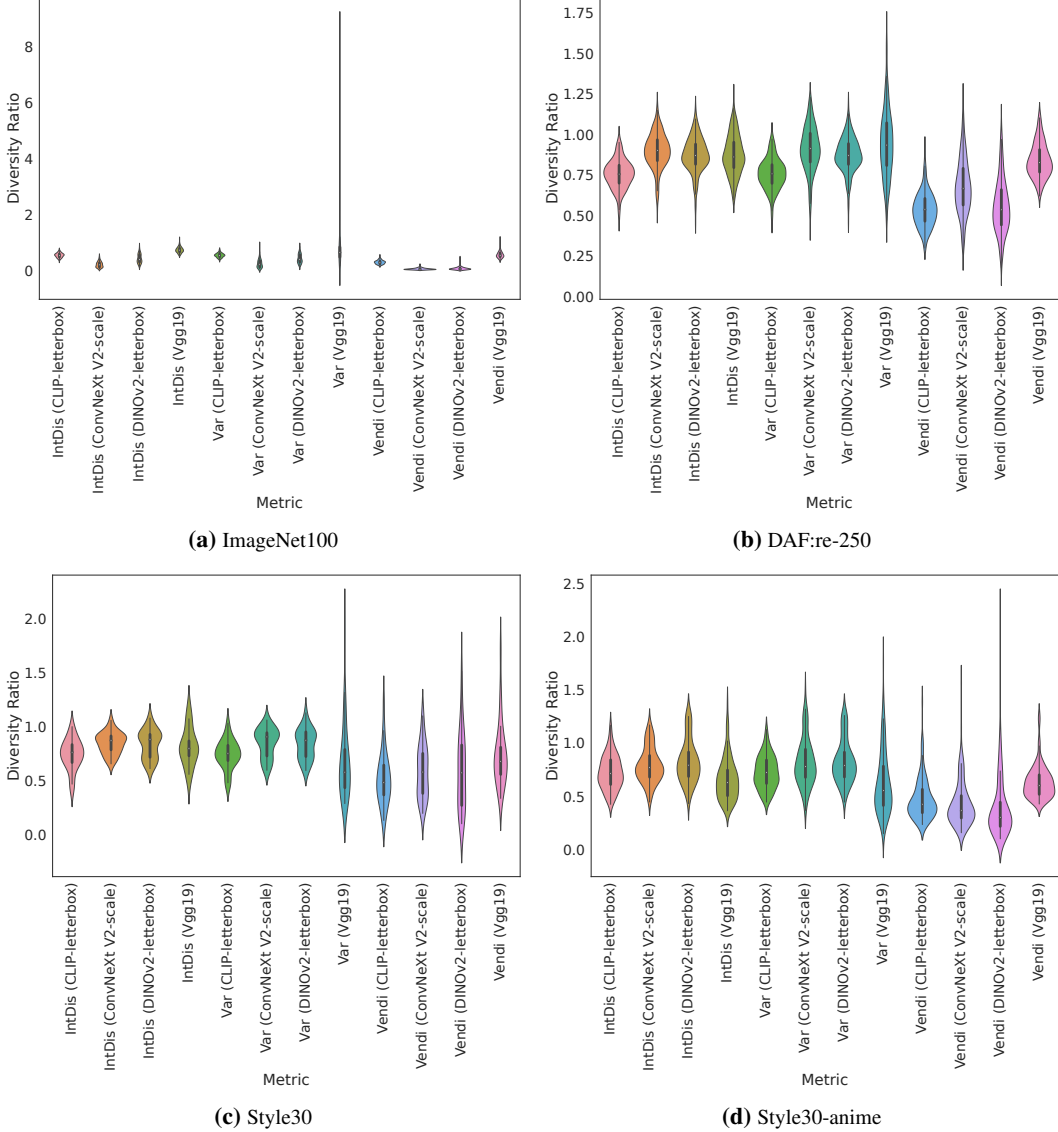


Figure 49: Distribution of diversity ratios across classes for different metrics/encoding methods. IntDis and Var respectively stand for intra-dissimilarity and variance. Only one resizing method is chosen for each encoder here.

here. Intriguingly, this observation does not hold true when we compute the diversity ratio using the Vendi score. The reason behind this discrepancy warrants further investigation. Finally, we generally observe a lower diversity ratio when Vendi score is used to compute diversity. This does suggest that the Vendi score can better discern datasets of various degrees of diversity.

H.2 Image Quality Assessment with Pretrained Models

Evaluating the quality of images generated by deep generative models is itself a challenge. In this appendix, we show that existing state-of-the-art image quality assessment (IQA) models may not be suitable for this task due to distribution shift. Specifically, We examine three leading IQA models: LIQE (Zhang et al., 2023), MANIQA (Yang et al., 2022), and a publicly available artifact scorer trained on the AI Horde ratings dataset (Haidra-Org, 2023; Wang et al., 2022).¹⁶

¹⁶The artifact scorer is available at <https://github.com/kenjiqq/aesthetics-scorer> (Accessed: 2023-08-20).

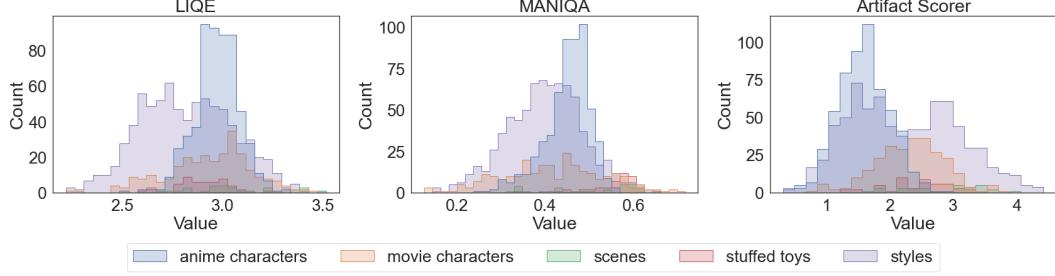


Figure 50: Distributions of the image quality scores on the training dataset. We note an important bias in these scores that favor or disfavor images of certain categories.

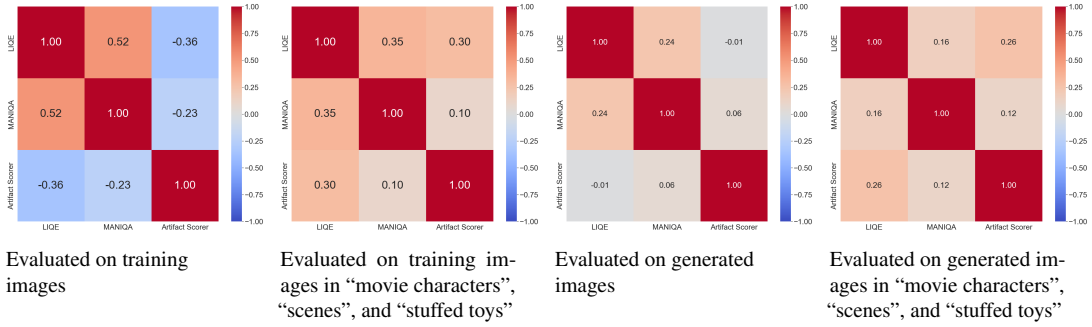


Figure 51: Correlation matrices of the considered image quality scores. We compute the correlation coefficients for scores obtained on different sets of images.

In more detail, we use the MANIQA model pretrained on the KONIQ-10K dataset (Hosu et al., 2020), and the artifact scorer that uses the `openclip_vit_l_14` features. For LIQE and MANIQA, multiple patches of size 224×224 need to be extracted from the images to estimate the scores. For this, we first resize the images so their shortest edges have 512 pixels, and then we extract 10 patches from each image. As for the artifact scorer, we resize the images to resolution 224×224 , with black padding added to the images if necessary (i.e., letterbox resizing).

Importantly, among the three models, only the artifact scorer is specifically made to evaluate AI-generated images, which is why we have included it in our study. Also, it is worth mentioning that while LIQE and MANIQA assign higher scores to better-quality images, the artifact scorer does the opposite. It gives a score between 0 and 5, where a higher score signifies more artifacts in the image. To make our results easier to compare, we thus convert this to “5 minus the original score” below.

Results. With these three IQA models, we evaluate the quality of both the images from our training set and those generated using training prompts and a 10th-epoch LoRA checkpoint trained with default hyperparameters. Our observations are as follows:

- **Style-Related Bias:** As shown in Figure 50, we find the image quality scores predicted by the models vary based on the style of the images. In particular, LIQE and MANIQA tend to give higher scores to anime-style images whereas the artifact scorer tends to give lower scores to them. For LIQE and MANIQA, we believe this is because they are trained exclusively on natural images, thereby limiting their predictive accuracy for artworks. In the case of the artifact scorer, the observed bias likely stems from inherent biases in the AI Horde ratings dataset. Such biases undermine the credibility of these IQA models, as image quality should ideally be style-agnostic.
- **Disagreement Among Models:** The correlation coefficients of the scores computed by different models are illustrated in Figure 51. Given the biases previously mentioned, we analyze the correlations in two distinct contexts: first across all training or considered generated images, and then excluding images from the “anime characters” and “styles” categories. In all the scenarios,

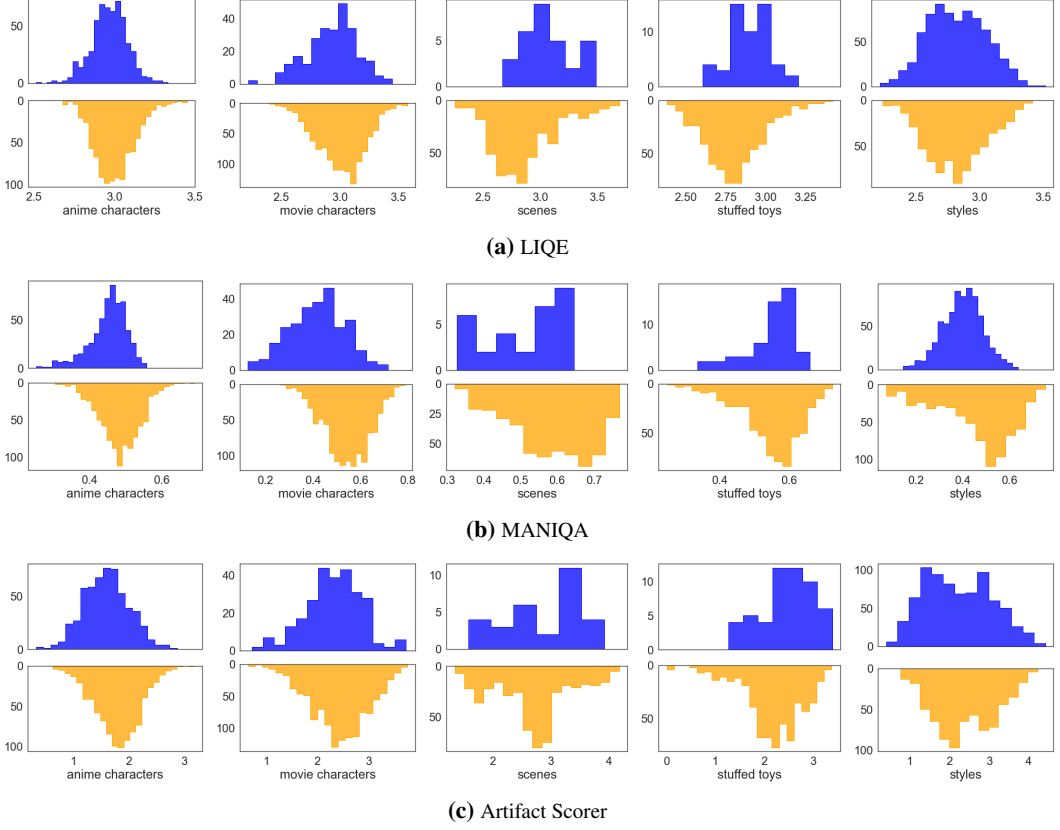


Figure 52: Distributions of the image quality scores on training (top, blue) and generated (bottom, yellow) images. We observe that these scores often fail to attribute higher scores to real images.

we observe that the models exhibit only a weak correlation in their predicted scores, indicating a lack of agreement among the predictions made by these models.

- **Inability to Distinguish Real from Generated Images:** In Figure 52, we contrast the quality scores assigned to dataset images with those given to generated images. The plots reveal that none of the three models consistently award higher scores to real images. More surprisingly, MANIQA often assigns higher scores to generated images, even when these contain noticeable artifacts.

In summary, the above observations cast doubt on the reliability of the three IQA models under consideration in evaluating the quality of AI-generated images. As a consequence, we have opted not to include them in our primary experiments.

H.3 Impact of Captioning Strategies on Model Performance

In this section, we explore the influence of captioning strategies on the performance of fine-tuned models. Specifically, we focus on three captioning strategies:

- **No Tags:** This approach follows the common practice in existing literature, using brief captions like “a photo of [V]” or “an illustration of [V]”.
- **All Tags:** In this setup, we append all tags predicted by the employed tagger to the concept descriptor, thereby creating richer captions.
- **Adjusted Tags:** This strategy is the one employed in our main experiment, wherein the tags are manually adjusted after the initial tagging phase. See Appendix D.1 for more details.

For the sake of simplicity, in the following, we just consider LoRA, LoHa, and LoKr trained with default hyperparameters, and native fine-tuning with learning rate 5×10^{-6} as our main experiment suggests that this consistently leads to better results than using the default 10^{-6} learning rate.

The image generation, metric computation, and metric processing procedures follow those employed in our main experiment. It is however important to note that when it comes to rank-based normalization of the metrics, we only compare with the checkpoints studied in this section. We report quantitative and qualitative results across these captioning strategies respectively in Figures 53 and 54.

Impact on Concept Fidelity, Controllability, and Base Style Preservation. A closer look at Figure 53 reveals the following trade-offs between different captioning strategies.

- **With no tags:** Although the use of simple caption seems to enhance concept fidelity, it comes at the expense of both controllability and base style preservation.¹⁷
- **With all tags:** Conversely, including all tags improves controllability and base style preservation but sacrifices concept fidelity. This compromise occurs because each component of the target concept is automatically mapped to the tag that most closely describes it. Without manual adjustments to these tags, the concept becomes fragmented across its various components. As a result, the concept descriptor captures only a partial and limited aspect of the target concept.

These contrasting effects are demonstrated in Figure 54. The leftmost figures of the first and third rows show that models trained on captions devoid of tags struggle to appropriately respond to prompts. On the other hand, in the rightmost figure of the first row, it is shown that a model trained with all the tags produced by the tagger fails to accurately capture the hairstyle and the uniform of the character. Even worse, in the rightmost figure of the second row, the sculpture, which should be the focus of the concept, is completely absent. Instead, the concept descriptor is associated with the background. This misdirection is likely due to the consistent presence of the tag “Christmas tree” in the training captions for this specific class, causing the model to associate the sculpture with “Christmas tree” rather than with the intended concept descriptor.

The above findings also validate our choice of using adjusted tags in our main experiment. This approach strikes a delicate balance between the extremes observed in the “no tags” and “all tags” strategies, ensuring degrees of controllability without sacrificing concept integrity.

Impact on Diversity. Interestingly, Figure 53 also reveals that both alternative captioning strategies improve image diversity compared to the default “adjusted tags” approach. However, we believe this occurs for two distinct reasons. For the “no tags” strategy, this is mostly because the concept descriptor unintentionally captures additional elements from the training set, leading to a broader, albeit less accurate, interpretation of the target concept. In contrast, for the “all tags” strategy, the diversity seems to stem from the fact that the concept descriptor only captures a limited part of the target concept, allowing the model greater freedom in generating more diverse images.

In the meantime, we observe that in the “stuffed toys” category, the “all tags” strategy not only improves diversity but also enhances image similarity for images generated using solely the concept descriptor. This likely happens because our manually adjusted tags better encapsulate the image backgrounds compared to the predicted tags, resulting in models generating images with more “neutral” backgrounds when only the concept descriptor is involved in the prompts. On the other hand, when using the tags produced by the tagger, details from the training set’s background leak into the learned concepts, contributing to both higher similarity and diversity. This phenomenon is further illustrated in the last row of Figure 54.

¹⁷An exception to this general trend is observed in the case of LoHa, where base style preservation actually improves with simple captions, potentially due to the specific phrasing “A . . . of [V]” used in this case.

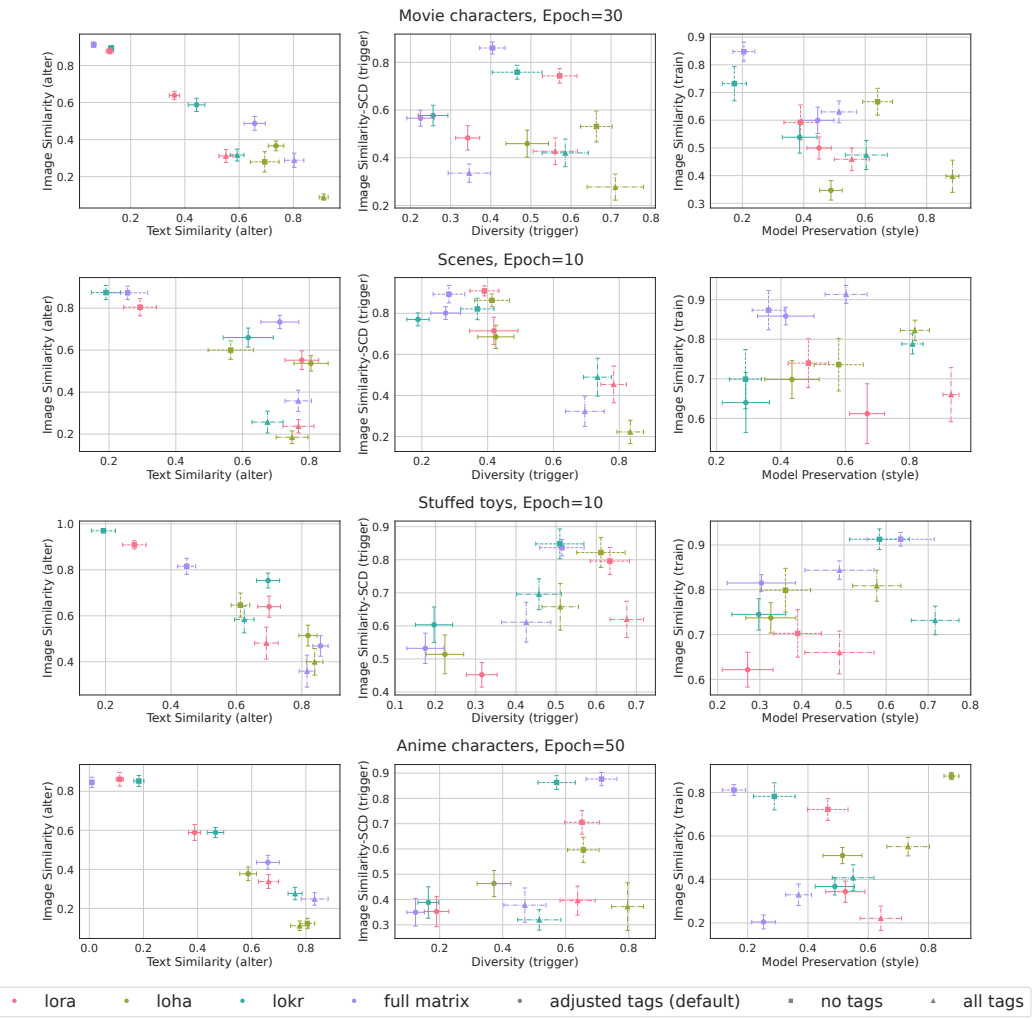


Figure 53: Scatter plots comparing different evaluation metrics with variations across algorithms and captioning strategies.

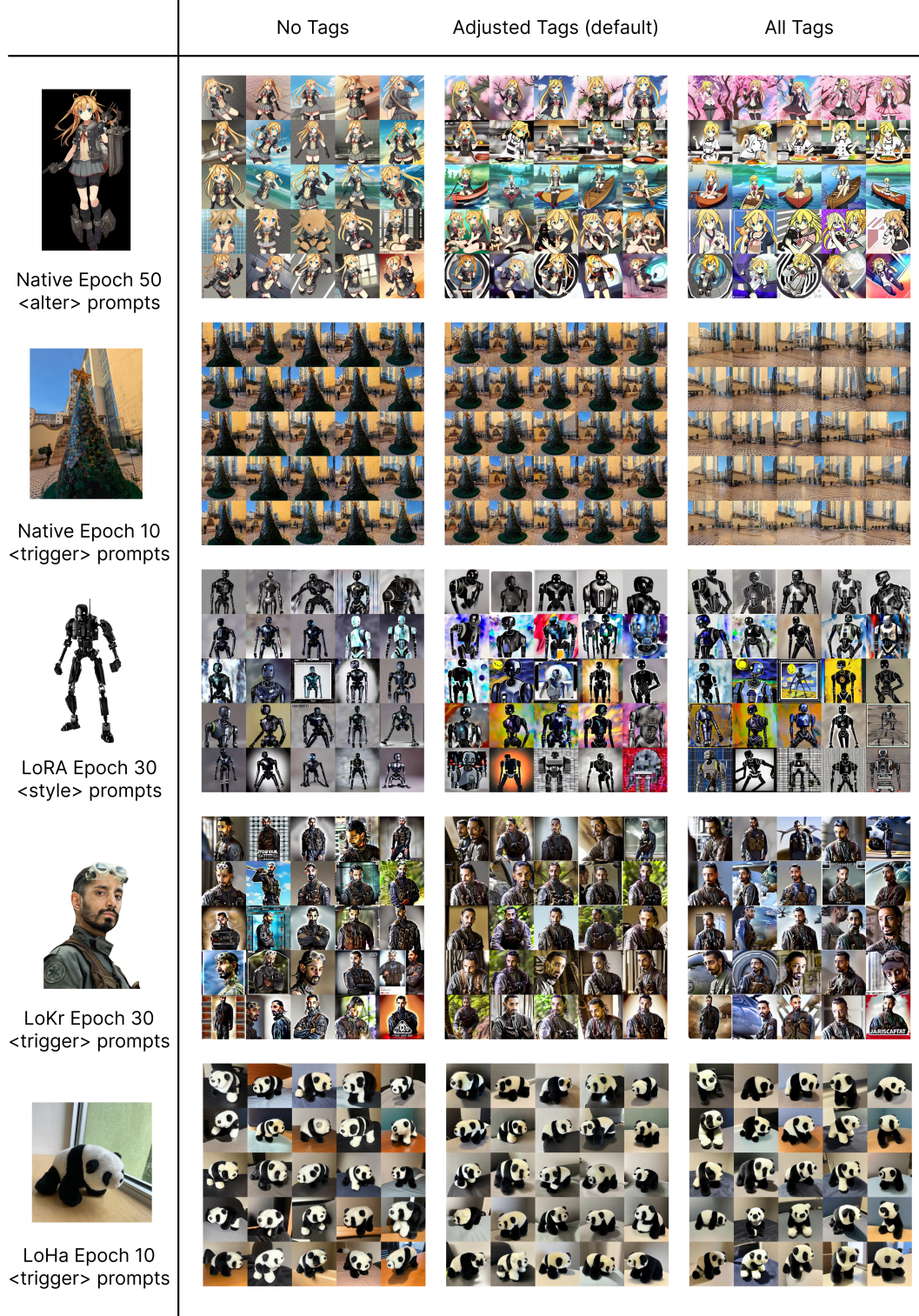


Figure 54: Generated images from models trained with different sets of captions. We observe that models trained with short captions without any further description of the images lack flexibility while training with unpruned tags could cause the target concept to be associated with the tags instead of the concept descriptor. Readers are referred to [Appendix D.3](#) for details on the evaluation prompts.

I Author Contributions

The contributions of each author are summarized in [Table 6](#).

	S.-Y. Yeh	Y.-G. Hsieh	Z. Gao	B. B W Yang	G. Oh	Y. Gong
Algorithm Conception	X		X		X	
Library Development	X				X	
Evaluation and Experiments		X	X			
Writing	X	XX	X	X		X

Table 6: Author contributions.